OPTIMIZATION OF MOLYBDENUM(V) CHLORIDE INTERCALATION PROCESS TO GRAPHENE FOR CONDUCTOR APPLICATIONS

EKKAPHOP KETSOMBUN

Student ID: NB 18501

Major: Functional Control Systems

Supervisor

Prof. Dr. Kazuyoshi Ueno

A thesis submitted in fulfilment of

the requirements for the award of the degree of

Doctor of Philosophy

Shibaura Institute of Technology

CANDIDATE'S DECLARATION

It is hereby declared that this thesis or any part of it has not been submitted elsewhere for the award of any degree or diploma.

Signed: ______________________

(Ekkaphop Ketsombun)

Student No.: NB18501

Certified by: ______________________

(Prof. Dr. Kazuyoshi Ueno)

Dedicated
To
My family and my supervisor

Acknowledgments

First of all, I would like to express the deepest appreciation to my supervisor, **Prof. Dr. Kazuyoshi Ueno**, Department of Electronic Engineering (SIT), Japan, for all the support and encouragement to accomplish this thesis. This dissertation would never have been possible without his guidance and constant feedback.

Also, I would like to express my deepest gratitude to **Dr. Zsolt Tokei** (imac, Belgium)**,** **Dr. Dennis Lin** (imac, Belgium), **Dr. Cedric Huyghebaert** (imac, Belgium), **Dr. Inge Asselberghs** (imac, Belgium), **Dr. Xiangyu Wu** (imac, Belgium), and **Miss Swati Achra** (imac, Belgium) for their collaborations and fruitful discussions on some topics related to my research.

I am grateful to **Prof. Hiroyasu Ishikawa** (SIT), **Prof. Tadashi Maeda** (SIT), **Prof. Shinichi Tanaka** (SIT), and **Prof. Eiichi Kondoh** (University of Yamanashi) for their kind review of my dissertation.

I gratefully acknowledge the funding I received toward my doctoral course at SIT from **the Hybridge Twinning program** (SIT) and **SIT Research Center for Green Innovation.**

Also, I would like to thank the **Department of Physics**, **Faculty of Science**, **King Mongkut's University of Technology Thonburi** for the three years of study leave during my study at SIT.

I am thankful to **Mrs. Mikiko Nikami**, **Dr. Ploybussara Gomasang**, **Mr. Tomoki Akimoto**, and **all members of the Nanoelectronic Laboratory** (SIT) for the continuous encouragement provided to me.

Abstract

Conductor materials such as copper (Cu) have been used for electron devices. Recently, Internet of Things (IoT), artificial intelligence (AI), and 5G are leading the development of electronic device technologies including conductors. For electronic device applications, conductors are used as the materials for inductors, interconnects, and transparent conductive films. Doped graphene has attracted people's interest as the new conductor material due to its potential of low-resistance, high reliability, and high inductance density. Few layer graphene (FLG) is expected to be used in applications that include LSI interconnects and transparent electrodes of solar cells. Doped multilayer graphene (MLG) is the one candidate for inductors to achieve both continuous sizes scaling while fulfilling the inductance and performance requirements due to the increasing of kinetic inductance after doping. This study reported the optimization of process guidelines for the $MoCl_5$ intercalation process which is known as a stable doping method. $MoCl_5$ intercalation for FLG, exfoliated highly oriented graphite (e-HOPG) to mimic the high crystallinity of MLG, and chemical vapor deposition-MLG (CVD-MLG) as a practical deposition method. This study also proposes a practical fabrication process for doped CVD-MLG patterns as a potential method for inductor applications.

The optimization of the FLG was expected to be used as a scaling down of the interconnects and transparent electrodes. Moreover, the results of the FLG was used for the process guidelines of thicker graphene layers. This work proposes a $MoCl_5$ intercalation process for doping FLG at a low temperature of 150 ºC using a high concentration of $MoCl_5$ chemicals. Bilayer graphene (BLG) was successfully doped at 150 ºC without serious damages within a short time process of 30-60 min. The uniformity of doping was improved by increasing the reaction time. However, the damage on the narrow width was found. To avoid the damage, the work proposed to reduce the chemical concentration of the $MoCl_5$ intercalation process.

For the reduced chemical concentration, this work found that optimum intercalation temperature and time depend on the layer number of FLG. The bilayer graphene (BLG) was intercalated at 175ºC without serious damage, besides that higher temperature of 200ºC was

required to intercalate tri-layer graphene (TLG) with a fixed reaction time for 60 min. Although we can reduce the intercalation temperature for TLG, a longer reaction time is required and higher damage is found. After considering both viewpoints of the effective doping and low damage, the high reaction temperature with short reaction time conditions may be suitable for the TLG intercalation process. The stacked upper layer is considered to protect the underlying layer from chemical damage during the intercalation process and it leads to the higher activation energy for intercalation at the same time. Therefore, higher reaction temperature or longer reaction time are required for intercalating FLG with more layer numbers.

Thick MLG, of the order of micrometers, is required for MLG applications in high-frequency devices, such as inductors. e-HOPG films were used to mimic a high crystallinity MLG films. Damage-less doping process with $MoCl_5$ intercalation for e-HOPG has been developed by optimizing the chemical concentration and temperature. This work found that the thick e-HOPG films are more susceptible to the intercalation damage than the FLG. The damage was found to be reduced by lowering the chemical concentration. This work found that there is a trade-off relationship between the doping efficiency and damage. An efficient doping with 77% reduction of sheet resistance without serious damage was obtained with the further optimization of temperature and time. The strain and hole density induced during the intercalation process were analyzed using G and 2D peak correlation plots. The changes in strain and carrier density agreed well with the observed damage and sheet resistance. Moreover, the intercalation process obtains high stability after storage in the N_2 box for 40 weeks. It is suggested that the optimization of intercalation conditions is essential for low-resistance and high-inductance applications of doped e-HOPG.

CVD-MLG is expected to be a more practical method for device manufacture than e-HOPG. The optimization of CVD temperature provides a guideline for the $MoCl_5$ intercalation process with patterned CVD-MLG. High-crystallinity CVD-MLG with a G/D ratio of 88 was obtained with a high CVD temperature of 900 ℃. A higher crystallinity of the G/D ratio more than 20 was required for $MoCl_5$ intercalation. The morphology did not change after the intercalation process. Cross-sectional SEM images showed the stacked layers of CVD-MLG and Ni. Part of the Ni layer was removed after intercalation at a temperature of

300 ℃. It is suggested that the doped of CVD-MLG can be used as a more practical method for the doped-MLG inductor fabrication.

For the practical fabrication process of the doped MLG pattern such as inductor, this work proposed the selective CVD-MLG on Ni catalyst and stable $MoCl_5$ intercalation process with the G/D ratio above 20. Finally, stage 2 intercalation and above was achieved by increasing the intercalation temperature and using high-crystallinity CVD-MLG. The sheet resistance was reduced after intercalation.

In this study, we investigated the optimization of $MoCl_5$ intercalation, which is known as stable intercalation, to MLGs of various film thickness. There is a trade-off relationship between the doping density and the damage induced by the $MoCl_5$ intercalation process, therefore the optimization will be inevitable depending on the MLG thickness. The optimized condition will lead to obtain a low-resistance and stable MLG for various conductor applications in electron devices to support the advancement of the IoT, AI, and 5G technologies and beyond.

Contents

	Page
Acknowledgment	**I**
Abstract	**II**
Contents	**V**
List of Figures	**IX**
List of Tables	**XV**
List of Abbreviations	**XVI**
List of Publications	**XIX**
1 Introduction	**1-24**
1.1 Overview	1
1.2 Doped graphene applications: background and issues	3
1.2.1 Theory and discovery of graphene	3
1.2.2 Doping methods of graphene	4
1.2.2.1 Surface transfer doping of graphene	6
1.2.2.2 Substitutional doping of graphene	6
1.2.2.3 Intercalation doping of graphene	7
1.2.3 Intercalation doping of graphene for electronic device applications	7
1.2.3.1 Doped graphene interconnects	8
1.2.3.2 Doped graphene inductors	10

1.3 Literature review related to the objective of this research 14
1.3.1 Literature review related to intercalation doping of graphene 14
1.3.2 Literature review related to $MoCl_5$ intercalation doping 17
1.4 Aim and approach to reach the goal of this study 18
1.5 Structure of the thesis 19
References 22

2 Graphene fabrication, intercalation process, and methodology 25-46
2.1 Overview 25
2.2 Graphene fabrication 25
2.2.1 Few layer graphene fabrication 26
2.2.1.1 Few layer graphene growth 26
2.2.1.2 Few layer graphene transfer process 26
2.2.2 Multilayer graphene fabrication 27
2.2.2.1 Substrate cleaning 27
2.2.2.2 Ni catalyst deposition 28
2.2.2.3 Multilayer graphene growth 29
2.2.3 Exfoliated highly oriented pyrolytic graphite preparation 30
2.3 $MoCl_5$ intercalation 31
2.4 Metal electrode fabrication 33
2.5 Methodology 34
2.5.1 Raman spectroscopy 35
2.5.2 Scanning electron microscopy 38
2.5.3 Energy dispersive X-ray analysis (EDX) 38
2.5.4 Atomic force microscopy 39
2.5.5 Laser scanning microscopy 40
2.5.6 Optical microscopy 41
2.5.7 Four-probe method 42
References 45

3 **Intercalation to few layer graphene** **47-71**
3.1 Introduction 47
3.2 Experimental methods 47
3.3 Results and discussion 48
3.3.1 High chemical concentration intercalant process 49
3.3.2 Reduced chemical concentration intercalation 55
3.3.2.1 Doping efficiency characterization by Raman spectroscopy 55
3.3.2.1.1 Reaction temperature dependence of doping efficiency 55
3.3.2.1.2 Reaction time dependence of doping efficiency 59
3.3.2.2 Damage in FLG from the intercalation process 61
3.3.2.2.1 Reaction temperature dependence of FLG damage 61
3.3.2.2.2 Reaction time dependence of FLG damage 65
3.4 Summary and conclusion 69
References 70

4 **Intercalation to exfoliated highly oriented pyrolytic graphite (e-HOPG)** **72-93**
4.1 Introduction 72
4.2 Experimental methods 72
4.3 Results and discussion 73
4.3.1 Chemical amount dependence of doping efficiency and damage 74
4.3.2 Reaction temperature dependence of doping efficiency and damage 77
4.3.3 Reaction time dependence of doping efficiency and damage 82
4.3.4 Strain and charge density of HOPG after $MoCl_5$ intercalation process 87
4.3.5 Stability of doping efficiency and sheet resistance 91
4.4 Summary and conclusions 92

References 93

5 Intercalation of CVD-MLG 94-109

5.1 Introduction 94

5.2 Experimental methods 94

5.3 Results and discussion 95

5.3.1 Optimization of CVD temperature for highly crystalline MLG 95

5.3.2 Optimization of $MoCl_5$ intercalation temperature for CVD-MLG 101

5.4 Summary and conclusion 108

References 109

6 Intercalation of patterned CVD-MLG 110-126

6.1 Introduction 110

6.2 Experimental methods 110

6.3 Results and discussion 111

6.3.1 Fabrication of CVD-MLG patterns 111

6.3.2 Doping efficiency of CVD-MLG patterns 114

6.3.3 TLM measurement of CVD-MLG patterns 119

6.4 Summary and conclusion 125

References 126

7 Conclusions and future prospects 127-130

7.1 Overall conclusions 127

7.2 Conclusions for each chapter 127

7.2.1. Chapter 3 127

7.2.2. Chapter 4 128

7.2.3. Chapter 5 128

7.2.4. Chapter 6 129

7.3. Future prospects 129

List of Figures

1.1	Schematic of a smart city concept using 5G technology.	2
1.2	(a) Honeycomb lattice of monolayer graphene and (b) electronic dispersion in the honeycomb lattice band structure calculated using the tight-binding method.	3
1.3	Schematic showing the relationship between positions of the HOMO-LUMO levels of dopants with respect to the Fermi level of graphene for n- and p-type graphene doping.	5
1.4	Metals that are better than Cu in that they have a higher melting temperature and a lower resistivity.	9
1.5	Illustration (top) and scanning electron microscopy image (bottom) of intercalation-doped multilayer-graphene-nanoribbons for next-generation interconnects.	10
1.6	Comparison of scaling trends: required area of a typical on-chip inductor versus the area of a single logic transistor and width of the M1 interconnect.	11
1.7	Schematic of a spiral inductor and its simplified equivalent circuit (two-port network).	12
1.8	Simulation of total inductance and Q-factor (at 5 GHz) of a two-turn inductor with area (=outer diameter^2) scaling down.	13
1.9	Variation of kinetic inductance as a function of sample dimension (width) for various stages of intercalation-doped MLG (2D), compared with non-doped MLG (2D) and copper (3D).	14
1.10	Flowchart of this dissertation.	21

2.1	Flow of MLG fabrication on Ni catalyst from the CVD process.	27
2.2	Schematic diagram of the DC magnetron sputtering system.	29
2.3	Schematic diagram of the MLG growth process by CVD.	30
2.4	Schematic diagram of e-HOPG placement onto a SiO_2/Si substrate.	31
2.5	Schematic diagram of the experimental setup for the $MoCl_5$ intercalation process.	32
2.6	Schematic diagram of the evaporator system for metal electrode deposition.	34
2.7	Schematic diagram of Raman scattering phenomena.	35
2.8	Raman spectra of graphene.	37
2.9	Signals emitted from different regions of the interaction volume.	38
2.10	Illustration of the principle of characteristic X-rays used for EDX analysis.	39
2.11	Schematic illustration of atomic force microscopy (AFM).	40
2.12	Schematic of a confocal laser scanning microscope.	41
2.13	Basic construction of an optical microscope.	42
2.14	Schematic diagram of a linear four- probe.	43
2.15	Schematic diagram of a four-probe measurement for patterned MLG.	44
2.16	Schematic diagram of the electrode pattern for TLM measurements.	44
3.1	Optical microscopy morphology (left) and Raman spectra (right) of FLG.	49
3.2	Raman spectra of BLG and SLG after intercalation with a high concentration of $MoCl_5$ for 60 min at different temperatures.	50
3.3	Optical image and Raman mapping of the G peak position in SLG and BLG areas. High concentration at 150°C (a) for 60 min and (b) 30 min and (c) reduced concentration for 30 min.	51
3.4	Optical microscope images of surface morphology after reaction with high concentration $MoCl_5$ for 60 min at different reaction temperatures: (a) 250°C, (b) 150°C, and (c) 130°C. (d) Pristine graphene on SiO_2.	52
3.5	AFM results of BLG after reaction with high concentration $MoCl_5$ at 150°C.	53

3.6	G-band of BLG after intercalation using high chemical concentration at 150°C and 175°C and with reduced chemical concentration at 175°C.	54
3.7	Optical images after intercalation for 60 min.	55
3.8	G-band spectra of BLG and TLG after intercalation for 60 min.	56
3.9	Relationship between the average G peak position and reaction temperature after intercalation for 60 min.	57
3.10	Raman mapping of the G peak position of FLG after intercalation for 60 min.	58
3.11	G-band spectra of TLG after intercalation at 175°C.	60
3.12	Relationship between average G peak position of TLG and reaction time after intercalation at 175°C.	61
3.13	Optical images after 60 min of the intercalation process at different reaction temperatures.	62
3.14	AFM morphology of BLG after the intercalation process for 60 min at different temperatures.	62
3.15	AFM RMS roughness for different reaction temperatures of 150, 175, and 200°C.	63
3.16	Relationship between G/D ratios and reaction temperature after the intercalation process for 60 min.	64
3.17	Optical images after the intercalation process at 175°C for various reaction times.	65
3.18	Morphology from AFM after the intercalation process at 175°C for different reaction times.	66
3.19	RMS roughness for different reaction times of 60, 90, and 120 min.	66
3.20	Relationship between G/D ratios and reaction time at 175°C.	67
3.21	Schematic model explaining the graphene layer number dependence of $MoCl_5$ intercalation into FLG.	69
4.1	Cross-sectional photo from SEM, surface morphology from OM and Raman spectra of e-HOPG and FLG.	74
4.2	G-band spectra of e-HOPG after intercalation using 200ºC for 30 min.	75

4.3 Surface SEM images of e-HOPG after intercalation at 200℃ for 30 min. 76
4.4 G-band spectra after intercalation using the STD/5 and STD/6 chemicals for 30 min. 78
4.5 Relationship between the reduction ratio of sheet resistance between before and after intercalation for 30 min and the reaction temperature. 79
4.6 Surface morphology after intercalation process of STD/5 and STD/6 chemical for 30 min from SEM. 80
4.7 Surface morphology after intercalation process of STD/5 and STD/6 chemical for 30 min from AFM. 81
4.8 G-band spectra after intercalation using the STD/5 chemicals with 225°C. 83
4.9 Relationship between the reduction ratio of sheet resistance between before and after intercalation using the STD/5 chemical with 225°C and the reaction time. 84
4.10 Surface SEM images of e-HOPG after intercalation process using STD/5 chemical with 225°C. 85
4.11 Surface morphology images of e-HOPG after intercalation process using STD/5 chemical with 225°C from AFM. 86
4.12 Correlation between the G-peak position and 2D-peak position after intercalation of temperature dependence of STD/5 and STD/6 chemicals for 30 min. 88
4.13 Correlation between the G-peak position and 2D-peak position after intercalation of time dependence using STD/5 chemical at 225°C. 89
4.14 Schematic model to explain the mechanism for damage with $MoCl_5$ intercalation process. 90
4.15 G-band spectra after intercalation using the STD/5 with 225°C and 250°C for 30 min after storage for 40 weeks. 91
4.16 Reduction ratio of sheet resistance between before and after intercalation using the STD/5 chemical for 30 min after storage for 40 weeks. 92
5.1 Optical images of CVD-MLG at different CVD temperatures. 95

5.2	Raman spectra of CVD-MLG on Ni catalyst at different CVD temperatures.	96
5.3	Raman spectra of CVD-MLG on Ni catalyst grown at different CVD temperatures.	97
5.4	AFM surface morphology and RMS roughness of CVD-MLG grown at different CVD temperatures.	98
5.5	Cross-sectional SEM images of CVD-MLG at different CVD temperatures.	99
5.6	EDX mapping of cross-sectional CVD-MLG after CVD growth at 900 ℃.	99
5.7	Sheet resistance of CVD-MLG after the CVD process at different CVD temperatures.	100
5.8	G-band spectra of CVD-MLG after intercalation for 30 min.	101
5.9	Relationship between the G-peak position of CVD-MLG after intercalation at different intercalation temperatures and the G/D ratio before intercalation.	102
5.10	Optical images of CVD-MLG before and after the intercalation process.	103
5.11	SEM surface morphology before and after intercalation at different temperatures.	104
5.12	Cross-sectional SEM images of CVD-MLG before and after intercalation at 300 ℃.	105
5.13	EDX mapping of cross-sectional SEM before and after intercalation at 300 ℃.	106
5.14	Sheet resistance reduction after intercalation at 300 ℃.	107
6.1	Fabrication procedure of doped MLG patterns	111
6.2	Fabricated MLG/Ni patterns (left) and a schematic of the four-terminal Pd electrodes (right) to measure sheet resistance.	112
6.3	Raman spectra of CVD-MLG on Ni catalyst for each width.	113
6.4	G/D ratio of CVD-MLG on Ni patterns of different widths.	113
6.5	Thickness of MLG/Ni at the center and edge of the pattern for each width.	114
6.6	G-band spectra at the center and edge of the pattern for each width.	115

6.7	Optical images of the surface of patterned CVD-MLG on Ni catalyst for each width.	116
6.8	SEM surface morphology of patterned CVD-MLG on Ni catalyst for each width.	117
6.9	Sheet resistance before and after intercalation for different widths.	118
6.10	Cross-sectional SEM images of 2.5-mm width patterns before and after intercalation at 300 ºC for 30 min.	119
6.11	Fabricated MLG/Ni patterns for the TLM measurement (left) and a schematic of the TLM measurement (right) to measure sheet resistance and contact resistance.	120
6.12	Optical images of the surface of patterned CVD-MLG on Ni catalyst for TLM-measurement structure.	121
6.13	G-band spectra of CVD-MLG for the TLM-measurement structure.	122
6.14	Sheet resistance before and after intercalation from the TLM-measurement.	123
6.15	Contact resistance before and after intercalation from the TLM-measurement.	124

List of Tables

1.1	Summary of graphene doping methods.	6
2.1	Summary of graphene fabrication methods.	25
2.2	Summary of $MoCl_5$ intercalation doping conditions.	33
2.3	Relevant Raman spectra modes of graphene and their significance.	37
3.1	G/D ratio of host FLG before intercalation process.	64
4.1	RMS roughness of e-HOPG after intercalation from confocal laser microscope.	77
4.2	RMS roughness of e-HOPG after intercalation from AFM.	82
4.3	RMS roughness of e-HOPG after intercalation using STD/5 chemical with 225℃ by AFM.	86

List of Abbreviations

2D = Two dimensional
3D = Three dimensional
5G = Fifth generation
A = Ampere
a-C = Amorphous carbon
AFM = Atomic force microscopy
Ar = Argon
Ar+ = Ar ions
at% = Atomic percent
B = Boron
B_2H_6 = Diborane
BH_3 = Trihydridoboron
BLG = Bilayer graphene
Br = Bromine
°C = Degree Celsius
$CC1_4$ = Carbon tetrachloride
CCl_4 = Tetrachloromethane
Cl = Chlorine
cm = Centimeter
Co = Cobalt
Cu = Copper
$CuCl_2$ = Copper(II) chloride
CVD = Chemical vapor deposition
DC = Direct current
DFT = Density functional theory
EDX = Energy dispersive X-ray analysis
EF = Fermi level
e-HOPG = Exfoliated highly oriented pyrolytic graphite
EM = Electromigration
eV = Electronvolt
$FeCl_3$ = Iron(III) chloride

FEOL	=	Front-end-of-line
FLG	=	Few-layer graphene
g	=	Gram
G/D	=	Ratio of intensities of the G and D peak
G_0	=	Pristine graphite
G_1	=	Stage 2 intercalation
G_2	=	Stage 1 intercalation
GHz	=	Gigahertz
GICs	=	Graphite intercalation compounds
GNR	=	Graphene nanoribbon
H_2	=	Hydrogen
H_2O_2	=	Hydrogen peroxide
H_2SO_4	=	Sulfuric acid
He	=	Helium
HOMO	=	Highest occupied molecular orbital
I	=	Applied current
IoT	=	Internet of things
I_D	=	Intensities of the D peak
I_G	=	Intensities of the G peak
ICs	=	Integrated circuits
Ir	=	Iridium
KCl	=	Potassium chloride
L	=	Length
L_a	=	Crystallite size of graphene
L_K	=	Kinetic inductance
L_M	=	Magnetic inductance
L_{total}	=	Total inductance
Li_3N	=	Lithium nitride
LUMO	=	Lowest unoccupied molecular orbital
M	=	Molar mass
MA	=	Megaamperes
min	=	Minute
MLG	=	Multilayer graphene
$MoCl_5$	=	Molybdenum(V) chloride
MoO_x	=	Molybdenum oxide compounds
N	=	Nitrogen
n	=	Hole density
$N_3C_3Cl_3$	=	Cyanuric chloride
NaOH	=	Sodium hydroxide
NH_3BF_3	=	Trifluoroborane--ammonia
Ni	=	Nickel

nm	=	Nanometer
NTSG	=	N-doped tetragonal-shaped single crystal graphene
Pa	=	Pascal
Pd	=	Palladium
PGS	=	Pyrolytic Graphite Sheet
PMMA	=	Polymethyl methacrylate
Pt	=	Platinum
R_C	=	Contact resistance
R_s	=	Sheet resistance
R_T	=	Total resistance
RF	=	Radio frequency
RMS	=	Root mean square
rpm	=	Revolutions per minute
Ru	=	Ruthenium
s	=	Seconds
$SbCl_5$	=	Antimony(V) chloride
sccm	=	Standard cubic centimeters per minute
SEM	=	Scanning electron microscopy
Si	=	Silicon
SiO_2	=	Silicon dioxide
SLG	=	Single-layer graphene
STD	=	Standard
TEM	=	Transmission electron microscopy
THz	=	Terahertz
TLG	=	Tri-layer graphene
TLM	=	Transmission line measurement
UPW	=	Ultrapure water
V	=	Volt
W	=	Width
ε	=	Mechanical strain
λ_l	=	Wavelength of the excitation laser
μΩ	=	Microohm
Ω/sq	=	Ohms per square

List of Publications

[Journal papers]

1. **E. Ketsombun**, X.Wu, I. Asselberghs, S. Achra, C. Huyghebaert, D. Lin, Z.Tokei, and K. Ueno, “Reaction Temperature and Time Dependence of $MoCl_5$ Intercalation to Few-Layer Graphene”, Japanese Journal of Applied Physics, **59**, SLLE01, 2020.
2. **E. Ketsombun**, and K. Ueno, “Optimization of $MoCl_5$ Intercalation for Low-resistance and Low-damage Exfoliated Highly-Oriented Pyrolytic Graphite”, Microelectronic Engineering, submitted.

[International conference papers]

1. **E. Ketsombun**, K. Yokosawa, X.Wu, I. Asselberghs, S. Achra, C. Huyghebaert, Z.Tokei, and K. Ueno,et.al, “$MoCl_5$ Intercalation for CVD Graphene at Low Temperature using High Chemical Concentration”, IEEE International Interconnect Technology Conf. (IITC 2019) and the Materials for Advanced Metallization Conf. (MAM 2019), 2019.
2. X, Wu, I. Asselberghs, **E. Ketsombun**, K. Yokosawa, S. Achra, S. Brems, C. Huyghebaert, M. Heyns, B. Sorée, K. Ueno and Z. Tokei, “Electrical Characterization of $MoCl_5$ Intercalated Graphene Interconnects”, IEEE International Interconnect Technology Conf. (IITC 2019) and the Materials for Advanced Metallization Conf. (MAM 2019), 2019.
3. **E. Ketsombun**, X.Wu, I. Asselberghs, S. Achra, C. Huyghebaert, D. Lin, Z.Tokei, and K. Ueno, “Layer Number Dependence of $MoCl_5$ Intercalation to Few-Layer Graphene”, Advanced Metallization Conference 2019 (ADMETA2019), 2019.
4. **E. Ketsombun**, and K. Ueno, “Efficient $MoCl_5$ Intercalation Doping of Multilayer Graphene for Low-Resistance and Low-Damage”, International Conf. on Solid State Devices and Materials (SSDM2020), 2020.
5. **E. Ketsombun**, T. Akimoto and K. Ueno, “Fabrication of Highly Doped MLG Patterns Using Selective CVD and $MoCl_5$ Intercalation”, IEEE International Interconnect Technology Conf. (IITC 2021), 2021.

[Domestic conference papers]

1. **E. Ketsombun**, X.Wu, I. Asselberghs, S. Achra, C. Huyghebaert, D. Lin, Z.Tokei, and K. Ueno, “Chemical Concentration Dependence of $MoCl_5$ Intercalation to Bilayer Graphene”, The 80th Japan Society of Applied Physics (JSAP) Autumn Meeting, 2019
2. **E. Ketsombun**, X.Wu, I. Asselberghs, S. Achra, C. Huyghebaert, D. Lin, Z.Tokei, and K. Ueno, “Temperature Dependence of $MoCl_5$ Intercalation to Few Layer Graphene”, 7th Green Innovation Symposium, 2020
3. **E. Ketsombun**, and K. Ueno, “Efficient $MoCl_5$ Intercalation Doping of Exfoliated Highly Oriented Pyrolytic Graphite for Low Resistance and Low Damage”, 8th Green Innovation Symposium, 2021

CHAPTER 1
INTRODUCTION

1.1. Overview

The internet of things (IoT) has promised the development of solutions using different devices with computational capacity and connection to the internet. These solutions can be applied in the domains of healthcare, agriculture, smart cities, industry, and logistics, among many others [1-2]. Fifth generation wireless systems (5G) are required for communication between devices and computational analysis systems. Figure 1.1 shows an example model for a smart city concept using 5G technology. The technologies, which include the cloud, wireless, information technology, and social media, converge and become smarter everyday objects with real-time connections that lead to an automated world.

Wireless connections are driven by radio frequency (RF) integrated circuits (RF-ICs) that demand scalability, flexibility, high performance, and ease of integration. Decimeter, centimeter, and millimeter wave wideband internet access is expected to be used for 5G technology communications. For the miniaturize of on-chip inductors that can be operated with 5G technology, doped multilayer graphene (MLG) is one candidate to achieve continuous size scaling while fulfilling both inductance and performance requirements due to its kinetic inductance property [3-5].

Small size or the scaling down of electronic devices is also required for 5G technology to develop smarter devices. One challenge for scaling down is nano-interconnects for large-scale integrated interconnects. Doped graphene is considered an alternative replacement to copper interconnects due to its high current capacity and robustness against electromigration (EM) of doped graphene [6-7].

Conductor materials have been developed to support the advancement of the IoT and 5G technology. For electronic device applications, inductors, interconnects, and transparent conductive films have been developed using doped graphene while following 5G technology requirements.

Figure 1.1. Schematic of a smart city concept using 5G technology [3].

However, serious damage to graphene from the $MoCl_5$ intercalation doping process has been observed and there is a trade-off between doping efficiency and this damage. The $MoCl_5$ intercalation process used to obtain both low damage and high doping efficiency (low resistance) has become a challenge for the graphene doping process.

The purpose of this study is the optimization of the $MoCl_5$ intercalation process for transferred few-layer graphene (FLG), exfoliated highly oriented pyrolytic graphite (e-HOPG), and chemical vapor deposition (CVD) grown multilayer graphene (MLG) on Ni catalyst. Process design guidelines for $MoCl_5$ intercalation based on scientific discussions are included in this study. The experimental work also proposes a fabrication process for the patterning of doped CVD-MLG, using a Ni catalyst, for graphene inductor fabrication.

This chapter includes a discussion of the background, the physical theory for doped graphene and its applications, and the critical issues facing the intercalation doping process.

Moreover, the essential properties of doped MLG are discussed to reach the goals of low damage and low resistance.

1.2. Doped graphene applications: background and issues

1.2.1 Theory and discovery of graphene

Graphene is a two-dimensional monolayer of sp^2-hybridized carbon atoms arranged on a honeycomb lattice. The electronic band structure of graphene was revealed more than 60 years ago [8]. Figure 1.2 shows the honeycomb lattice of a monolayer of graphene and the band structure of graphene calculated using the tight-binding method [9]. In 2004, the observation of the electric field effect in FLG was reported. This report was acknowledged in 2010 with a Nobel Prize in Physics for the discovery of graphene and its characterization [10]. FLG was prepared by repeatedly peeling highly oriented pyrolytic graphite (HOPG), also known as the scotch tape method. Graphene exhibits remarkable optical properties, ultra-high intrinsic strength, superior thermal conductivity, and extremely high charge carrier mobility [9-11]. Due to their remarkable properties, graphene-based materials are expected to be used in a variety of applications, such as ultra-capacitors, graphene water filters, highly flexible organic light emitting diodes, transistors, and solar cell applications.

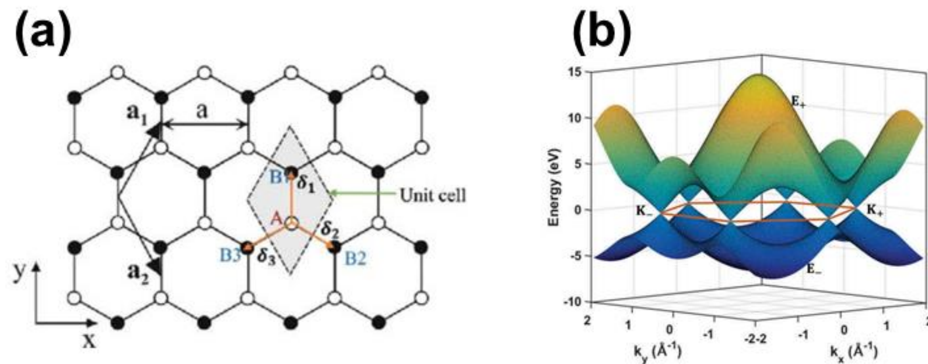

Figure 1.2. (a) Honeycomb lattice of monolayer graphene and (b) electronic dispersion in the honeycomb lattice band structure calculated using the tight-binding method [10].

Since the discovery of graphene from the scotch tape method, fabrication of large-area graphene film with high-electrical quality has been studied and reported using many fabrication methods. CVD was successfully used to fabricate large-area graphene [12]. Transition metal substrates, such as Ni, Pd, Ru, Ir, Co, and Cu, have been reported as catalysts for graphene growth from CVD using a hydrocarbon gas source [13]. In this study, FLG and MLG were fabricated using CVD. More details of the fabrication process are included in Chapter 2. However, high temperature growth and a transfer process for graphene material, from the transition metal to a real substrate after CVD, are still required. For device applications, low temperature growth and a transfer-free process are still attractive topics in graphene research.

Solid phase reaction is a transfer-free graphene deposition process. Amorphous carbon (a-C) is allowed to react with a catalyst layer by high temperature annealing using a fast heating rate. During the cooling process, MLG growth by precipitation takes place on both sides of the catalyst layer. The thickness of the MLG is related to the thickness of the a-C layer. However, the uniformity and crystallinity of the MLG are still lower than MLG fabricated by CVD. Therefore, the CVD method was selected for optimization of the $MoCl_5$ intercalation process and the investigation of device applications in this study.

1.2.2 Doping methods of graphene

The tight-binding model calculation can simulate the electronic dispersion in a honeycomb lattice, as shown in Figure 1.2. At the Brillouin zone corners, the Fermi level of graphene is located near the Dirac point. Moreover, the dispersion relation near the Dirac point is linear and, consequently, leads to pristine graphene being a zero band-gap semiconductor or a semimetal. Therefore, graphene shows a remarkably high electron mobility of 2.0×10^5 cm^2 V^{-1} s^{-1} at room temperature. For device applications, shifting of the Dirac point of pristine graphene relative to the Fermi level and precise control over charge carrier type are required [14]. Figure 1.3 shows a schematic of the relationship between positions of the highest occupied molecular orbital-lowest unoccupied molecular orbital (HOMO-LUMO) levels of dopants with respect to the Fermi level of graphene for n- and p-

type doping. The relative position of the density of states of the HOMO and LUMO of the dopant are used to consider the doping type compared to the Fermi level. Charge is transferred from the dopant to the graphene layer if the HOMO of the dopant is above the Fermi level of graphene, resulting in n-type doping. On the other hand, for dopants with a LUMO below the Fermi level, charge transfer occurs from the graphene layer to the dopant, resulting in p-type doping [14,15].

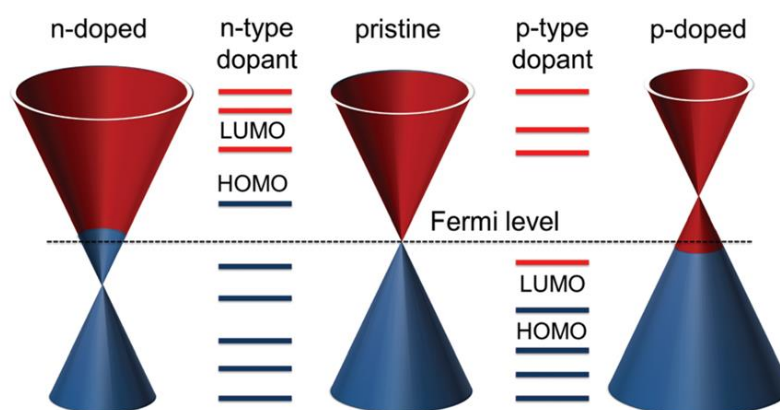

Figure 1.3. Schematic showing the relationship between positions of the HOMO-LUMO levels of dopants with respect to the Fermi level of graphene for n- and p-type graphene doping [15].

Methods for doping graphene have been reported by several research groups and have been based on doped graphene applications. Graphene doping methods can be separated into surface transfer, substitutional, and intercalation doping methods, as shown in Table 1.1. Details and demonstrations of these methods are described in the following sections.

Table 1.1. Summary of graphene doping methods.

Graphene doping method	Definition of doping method
Surface transfer doping	Transfer of electrons between surface molecules and the graphene layer.
Substitutional doping	Carbon atoms of graphene are substituted by dopant atoms.
Intercalation doping	Dopant molecules are intercalated between the interlayers of graphene.

1.2.2.1 Surface transfer doping of graphene

Surface transfer doping is a graphene doping method wherein electrons are transferred between dopant molecules on the top of the graphene and the graphene layer. In the case where molecules with electron receiving groups are adsorbed on the surface of the graphene, there is p-type doping of graphene. Molecules with electron donating groups adsorbed on the surface of graphene induce n-type doped graphene. Gases, organic molecules, and metal atoms are easily adsorbed on the surface of graphene due to its high surface area [14].

The p-type doping of graphene by the surface transfer doping method was reported by the adsorption of water vapor, NO_2 molecules, Br_2, and I_2. In the case of n-type doping, n-type semiconducting graphene was obtained after the adsorption of strong donating groups, such as ethanol, NH_3, and CO [16]. Surface transfer doping is suitable for chemical reaction sensing and bio-sensing applications. However, for electronic device applications, the surface transfer doping needs to resolve many issues such as the chemical stability after doping.

1.2.2.2 Substitutional doping of graphene

Substitutional doping of graphene can be separated into two different methods: direct synthesis and post treatment. Nitrogen, sulfur, phosphorus, boron, or transition metals have

been introduced into graphene to change the electron density. Direct synthesis approaches, such as CVD, solvothermal synthesis, and arc discharge, are widely used to produce homogeneous doping effects. However, post treatments, like thermal annealing or plasma treatment, succeed mainly in surface doping.

In the case of substitutional doping by the CVD process, n-type doping was successful in N-doped tetragonal-shaped single crystal graphene (NTSG) [17]. Additionally, B-doped graphene, from the incorporation of B atoms into graphene sheets with the use of boron powder as the precursor, showed p-type semiconductor features. The doping efficiency of graphene using the CVD process is related to parameters that include the catalyst, precursor, flow rate, temperature, pressure, and reaction time. However, challenges facing uniformity of the doping area need to resolved. In the case of the solvothermal approach, compounds such as BH_3, CCl_4, Li_3N, $N_3C_3Cl_3$, and NH_3BF_3 have been successfully used in doping [14,18-19]. For the arc discharge method, B- and N-doped graphene have been created by creating arc discharge with graphite electrodes in the presence of hydrogen (H_2), helium (He), diborane (B_2H_6) or H_2, He, and pyridine vapor. However, dopant content via the arc discharge method has only reached very low levels (0.5–1.5 at%) [14]. For lower dopant concentration and uniform doping area of graphene by substitutional doping, this method is still limited for large-scale electronic device applications.

1.2.2.3 Intercalation doping of graphene

Intercalation doping of graphene was developed from graphite intercalation compounds (GICs). GICs were used as a high-electrical conductivity material in electrical wiring and in Li ion secondary batteries [20]. The doping efficiency of the intercalation doping method is related to the intercalation stage [21]. The intercalation doping method is more suitable for electronic device applications, such as low-resistance interconnects and high-inductance applications in inductors or antennae, compared to other doping methods because of the stability of chemical intercalants, such as $MoCl_5$. Therefore, this study focuses on intercalation doping, with more details provided in the next section.

1.2.3 Intercalation doping of graphene for electronic device applications

In this study, graphene doped by the intercalation doping method was investigated to achieve low resistance and high inductance. Low-resistance doped graphene is expected to be used in interconnect applications. Doped graphene from the intercalation process is a candidate for next generation interconnects to replace copper. High-inductance doped graphene is expected to be the next generation of inductors because of the high kinetic inductance of doped graphene. Intercalation doping of graphene is also considered capable of solving scaling issues faced by on-chip inductors for 5G technology.

1.2.3.1 Doped graphene interconnects

Copper (Cu) thin films are widely used as the low-resistance interconnect material for lines and vias in both logic and memory chips. Downscaling of device dimensions below the 5 nm technology node is challenging for Cu interconnects and the chip front-end-of-line (FEOL) due to electrostatic and variability limitations. The increase of Cu interconnects resistivity and the degradation of EM reliability are serious issues after scaling-down pattern widths to below 40 nm [22,23]. A barrier/liner is required to avoid Cu migration into the surrounding oxide. However, the scaling of the liner and the current flow at the barrier are also becoming a problem. Figure 1.4 shows metals that are better than Cu in that they have a higher melting temperature and a lower resistivity. The most attractive metals are Co and Ru. For barrierless Ru and Co at the same trench cross-section with Cu, they outperform Cu at 16 nm and 12 nm, respectively. However, a big challenge with Co and Ru interconnects is chemical-mechanical polishing due to galvanic corrosion in narrow trenches.

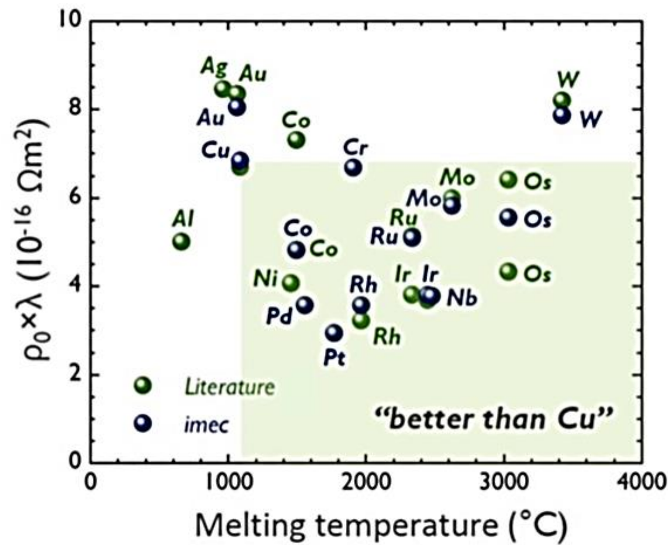

Figure 1.4. Metals that are better than Cu in that they have a higher melting temperature and a lower resistivity. [23].

The high current capacity and robustness against EM of graphene have been expected to benefit nano-interconnect applications [6,7]. Theoretically, graphene has been reported to potentially have good electrical properties after scaling down, such as high carrier mobility [24]. FLG interconnects retain a high carrier mobility of ~1000 cm ^{2}/Vs after scaling down to 20 nm [24,25]. However, lower electrical properties (lower carrier density) than those theoretically predicted for graphene have been obtained in experiments [26,27]. Graphene with intercalation doping has been expected to lower the electrical resistivity of graphene interconnects due to increased carrier density [28]. Several intercalates, such as $FeCl_3$, $MoCl_5$, and Br, have been proposed to intercalate with FLG and MLG for lowering resistivity. Figure 1.5 shows $FeCl_3$ intercalation to a graphene nanoribbon (GNR) interconnect. $FeCl_3$ intercalation-doped ML-GNR interconnects, with a width down to ~20 nm, were demonstrated with a resistivity of 21.45 μΩ cm, which is comparable to Cu of the same thickness. Moreover, extremely high current carrying capacity (no degradation after 7 h under 200 MA/cm^2 and a 475 K stress condition) was provided by $FeCl_3$ intercalation-doped ML-GNR interconnects, with which Cu cannot compete [26]. In addition, $MoCl_5$ intercalation shows higher chemical stability than other metal chlorides [29,30]. Therefore,

$MoCl_5$ intercalation with graphene was selected as the low-resistance material to investigate in this study.

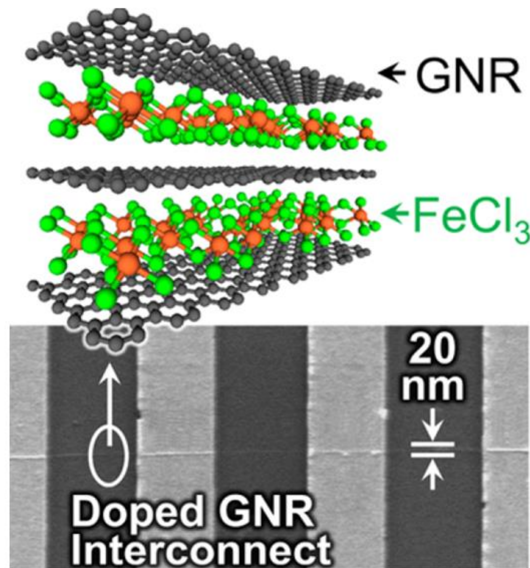

Figure 1.5. Illustration (top) and scanning electron microscopy image (bottom) of intercalation-doped multilayer-graphene-nanoribbons for next-generation interconnects [26].

1.2.3.2 Doped graphene inductors

The scaling down of RF integrated circuits (RF-ICs) is required for achieving 5G technology. Figure 1.6 provides a comparison of the following scaling trends: required area of a typical on-chip inductor versus area of a single logic transistor and width of the M1 interconnect. The rapid scaling down of transistors and interconnects in IC technology has been achieved with increase in performance. However, the scaling down of on-chip inductors is slower due to the fact that large inductor areas are dictated by fundamental electromagnetics.

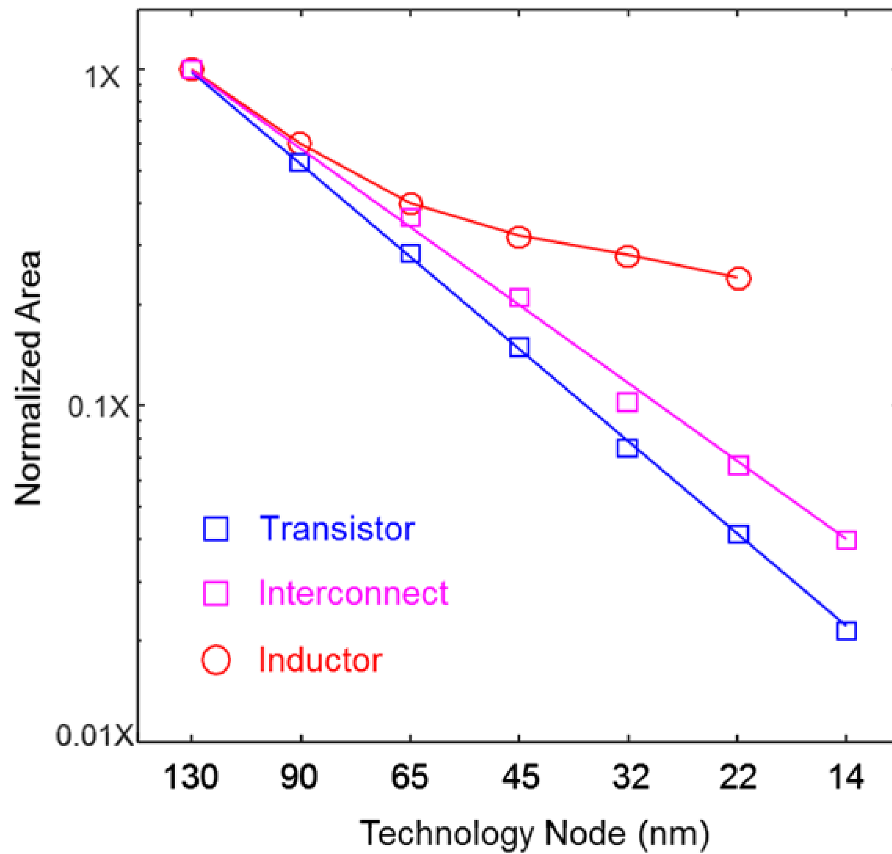

Figure 1.6. Comparison of scaling trends: required area of a typical on-chip inductor versus the area of a single logic transistor and width of the M1 interconnect [31].

The size of the inductor is related to the inductance, which requires large surface area to achieve desired values of inductance density. Therefore, scaling down of the on-chip inductor is limited by Faraday's law of electromagnetic induction. To achieve continuous size scaling while fulfilling inductance and performance requirements, improved inductance density is required. The inductance density can be defined by the total inductance (L_{total}) per unit area of the inductor. The total inductance is the sum of the magnetic inductance (L_M) and the kinetic inductance (L_K). Figure 1.7 shows a schematic of a spiral inductor and its simplified equivalent circuit (two-port network). The red dotted curves in the figure represent the time-varying magnetic field, which results in magnetic inductance. The blue dots in the figure represent charge carriers with inertia, which result in kinetic inductance.

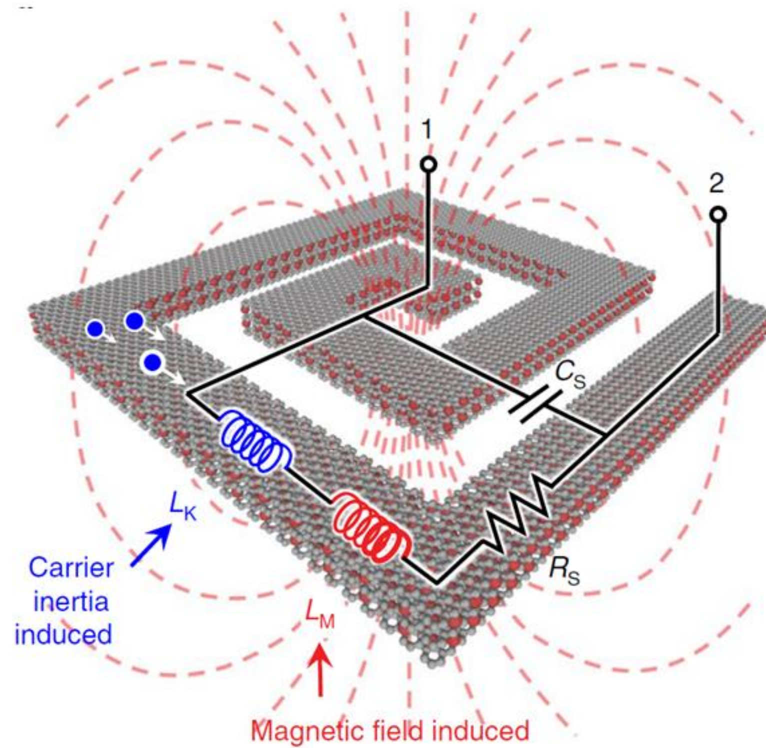

Figure 1.7. Schematic of a spiral inductor and its simplified equivalent circuit (two-port network) [31].

Figure 1.8 shows the simulation of total inductance and Q-factor (at 5 GHz) of a two-turn inductor with area (=outer diameter squared) scaling down. At the same inductor area, conventional Cu inductors without kinetic inductance (L_K) show lower inductance and Q-factor compared with an artificial inductor that included kinetic inductance at the same the inductor area. To continue the scaling down of an on-chip inductor for RF-ICs, the improvement of kinetic inductance in the next generation of spiral inductors should be considered.

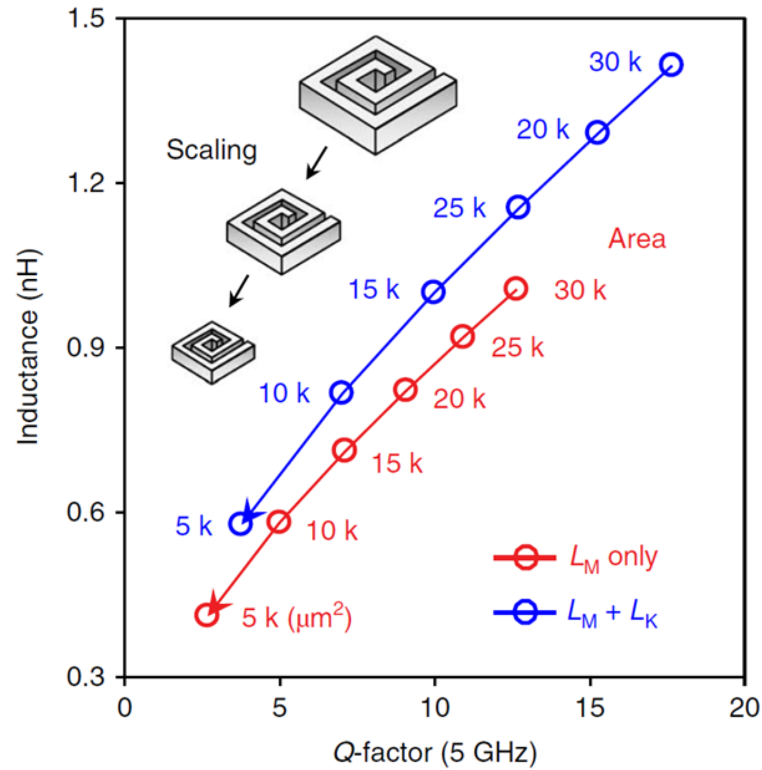

Figure 1.8. Simulation of total inductance and Q-factor (at 5 GHz) of a two-turn inductor with area (=outer diameter^2) scaling down [31].

The intercalation doping of MLG has been expected to be used for next-generation inductors due to its increased carrier density from the doping effect and due to interlayer decoupling after intercalation doping for larger kinetic inductance. Figure 1.9 shows the variation of kinetic inductance as a function of sample dimension (width), which was studied for various stages of intercalation-doped MLG (2D) and compared with non-doped MLG (2D) and conventional copper (3D). The kinetic inductance can be improved by $FeCl_3$ intercalated to MLG and the kinetic inductance depends on the stage of intercalation doping. However, many aspects of the intercalation process need to be investigated, such as the intercalant, the fabrication process, and the scientific mechanism explaining phenomena. $MoCl_5$ intercalation to MLG is investigated in this study for its potential as a next-generation inductor. A literature review related to $MoCl_5$ intercalation doping and the aims and approaches of this study will be described in the following sections.

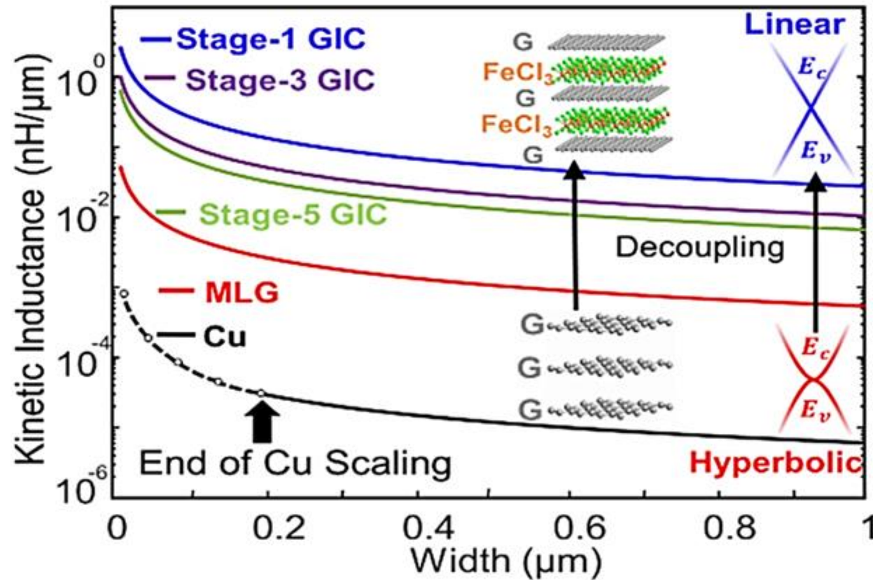

Figure 1.9. Variation of kinetic inductance as a function of sample dimension (width) for various stages of intercalation-doped MLG (2D), compared with non-doped MLG (2D) and copper (3D) [32].

1.3. Literature review related to the objective of this research

The literature review on the intercalation doping process, in terms of electrical properties improvement after intercalating by the intercalant, the type of intercalant, and the intercalant selection based on stability, are related to the objective of this study. A summary of each as described in the literature follows.

1.3.1 Literature review related to intercalation doping of graphene

The intercalation doping of graphene has been developed from the GICs method. In 1841, the first discovery of potassium GICs was reported and led to hundreds of GIC chemical products. Alkali metal and metal chloride, fluoride, acid, and halogen compounds were reported after the discovery of GICs [18]. This literature review is based on intercalation doping related to electronic device applications.

J. Nathaniel et al. [33], reported first-principles density functional theory (DFT), including interlayer van der Waals interactions, of $FeCl_3$ intercalated bilayer graphene. The calculation results demonstrated that hole-doped graphene layers associated with the high electronegativity of $FeCl_3$ transform into electron-doped layers with a tuned applied bias.

K. Tasaki [34] reported DFT calculations with the van der Waals correction for GICs using the dispersion correction method within the framework of the generalized gradient approximation. The results showed that there is a strong correlation between intercalation energy and electron transfer between the intercalate and graphite.

W. Zhao et al. [35] reported intercalation of FLG flakes with $FeCl_3$ and the determination of the Fermi level (E_F), layer-by-layer decoupling, and stability using Raman spectra. The G-peak of heavily doped graphene shifts upward, to $\sim$1627 cm^{-1}, and a Lorentzian line shape exists for the 2D band, indicating that each layer behaves as a decoupled heavily doped monolayer. An estimated $E_F \approx 0.9$ eV and stability of up to one month after air exposure of doped graphene were reported.

Q. Chen et al. [36] reported $FeCl_3$ intercalation to continuous CVD graphene (CVD-G). The G-band position and two-dimensional band shape in the Raman spectra confirmed intercalation of $FeCl_3$ between the graphene layers. The $FeCl_3$ intercalation increased the electrical conductivity of the CVD-G with a well-maintained transmittance. Moreover, change in interlayer distance was detected by atomic force microscopy (AFM).

K. Ueno et al. [37] reported Br intercalation to MLG from e-HOPG. Based on the experiment, the Fermi level was shifted downward by 0.63 eV and the sheet resistance was reduced to less than 10% of that of pristine HOPG by increasing Br concentration.

R. Matsumoto et al. [38] reported the electrical conductivity and air stability of $FeCl_3$, $CuCl_2$, $MoCl_5$, and $SbCl_5$ GICs in flexible graphite sheets (PGS and GRAFOIL). The $CuCl_2$-GICs and $MoCl_5$-GICs did not decompose in air as a function of time. Degradation was observed for $FeCl_3$-GICs, while the $SbCl_5$-GICs transformed to a higher-stage intercalation. Moreover, the $MoCl_5$-GICs were the highest potential air stability and conductivity compounds.

From the summary of literature provided above, the improvement of electrical conductivity of doped graphene from the intercalation doping method is considered useful for creating low resistance and high-inductance material for nano-scaling of electronic devices. A summary of intercalation doping for the nano-scaling of electronic devices follows.

C. Xu et al. [28] reported the modeling, analysis, and design of GNR interconnects. Based on their simulations, which used a simple tight-binding model and the linear response Landauer formula, intercalation-doped multilayer zigzag GNRs can have better performance than that of Cu and W. This implies possible application of GNRs as local interconnects in some cases.

J. Jiang et al. [26] reported intercalation-doped ML-GNRs from CVD using $FeCl_3$ for next-generation interconnects. The sub-20-nm widths established that highly intercalated ML-GNRs can carry over 2×10^8 A/cm^2 of current density and are better than Cu interconnects. The key criterion of current carrying capacity is necessary for an alternative interconnect material.

M. Katagiri et al. [19] reported intercalation doping of narrow MLG interconnects from MLG flakes with sub-100-nm widths. The intercalation of $MoCl_5$ into narrow graphene interconnects under suitable conditions was confirmed by Raman scattering spectroscopy. These results indicated that intercalation using $MoCl_5$ is promising for the fabrication of narrow graphene interconnects.

D. Kondo et al. [39], reported sub-10-nm wide intercalated MLG interconnects using $FeCl_3$. After narrowing the width to 8 nm by electron beam lithography, the 8-nm-wide intercalated MLG exhibited a resistivity of 3.2 μΩ cm, which is predicted to be lower than that of Cu interconnects with the same dimensions.

K. Agashiwala et al. [32] reported DFT simulations in $FeCl_3$ intercalated MLG in terms of kinetic inductance in low-dimensional materials to enable a new generation of RF-electronics. The variation of kinetic inductance as a function of the sample dimension (width) of the inductor and stages of intercalation-doped MLG were presented. Among the various

materials analyzed, intercalated MLG was identified as the best inductor material to provide the maximum benefit of kinetic inductance for 5G/6G and THz technology requirements.

J. Kang et al. [31] reported on-chip intercalated-graphene inductors with Br_2 molecules for next-generation RF electronics. The two-turn spiral inductors based on bromine-intercalated MLG exhibited a 1.5-fold higher inductance density compared to conventional inductors and provided Q-factors of up to 12.

1.3.2 Literature review related to $MoCl_5$ intercalation doping

Based on the above literature review of intercalation doping, $MoCl_5$ intercalation is more attractive than other intercalants. The highest air stability was exhibited in $MoCl_5$ intercalation to graphene. Therefore, $MoCl_5$ intercalation was selected in this study to create low resistance and high-inductance material for electronic device applications. A literature review related to $MoCl_5$ intercalation follows.

J. Mittal et al. [30] reported the synthesis of Stage 1 $MoC1_5$-GIC in single phase by heating a mixture of $MoC1_5$ and $MoOC1_3$ with natural graphite (size of 85 μm). The stage structure of the $MoCI_5$-GICs depends on the presence of $MoOCI_3$. Stage 1 intercalation was observed after exposure to air with 50% humidity at 23°C for 10 min or after mixing with 0.25 mol.% $MoOC1_3$.

M. Inagaki et al. [29] reported that the stability of graphite flake intercalation compounds of $MoCI_5$ ($MoC1_5$-GICs) with Stage 2 and Stage 4 structure soaked in various solutions. The X-ray diffraction patterns of these GICs did not change after soaking in water at room temperature, boiling water, acetone, KCl-saturated aqueous solution, and $CC1_4$.

K. Kawamoto et al. [40] reported novel in-situ MoO_x passivation of $MoCl_5$ doped MLG flakes without air-exposure. Improved air stability of dopants was confirmed by Raman spectroscopy via direct MoO_x passivation at room temperature.

H. Miyazaki et al. [41] reported $MoCl_5$ intercalation doping and oxygen passivation of sub-micrometer-sized MLG. MLG flakes intercalated with Br_2, $FeCl_3$, and $MoCl_5$ were compared in terms of doping ability, robustness against environmental effects, and

miniaturization method. They found that $MoCl_5$ was advantageous for miniaturization and the doping effect was improved by oxidation of the intercalated material ($MoCl_5$).

H. Kinoshita et al. [42] reported highly conductive and transparent large-area bilayer graphene (BLG) realized by $MoCl_5$ intercalation. The twist-rich and AB-stacked BLG was prepared by a CVD process. Low sheet resistance (83 Ω/sq) was realized while maintaining high optical transmittance (≈95%) from the twist-rich BLG films after $MoCl_5$ intercalation. The low sheet resistance state was relatively stable in air for more than three months.

1.4. Aim and approach to reach the goal of this study

From the literature review provided in the previous section, the doping of graphene by the $MoCl_5$ intercalation process is expected to solve the scaling-down issues regarding the size of interconnects and inductors for conductors in electronic device applications.

However, serious damage of the graphene from the $MoCl_5$ intercalation doping process has been observed and there is a trade-off between doping efficiency and damage. An $MoCl_5$ intercalation process to obtain both low damage and high doping efficiency (low resistance) is a challenge for the doping process of graphene.

Based on the discussion in the previous sections, the optimization of $MoCl_5$ intercalation to FLG is the candidate low-resistance material for narrow interconnects to replace Cu. In a previous study of our laboratory, higher vapor pressure of intercalant was found to be more efficient for obtaining higher doping concentration in MLG flakes exfoliated from HOPG at 300 ℃ [39, 40]. Our approach for the optimization of $MoCl_5$ intercalation of FLG uses high chemical concentration to reduce intercalation temperature and time and investigates the doping efficiency and damage of graphene by the intercalation process. The analysis of results based on the scientific discussion of $MoCl_5$ intercalation to FLG leads to a process design guideline for $MoCl_5$ intercalation of thicker graphene layers.

For device applications with graphene inductors or antennae, graphene thicker than FLG is required to study $MoCl_5$ intercalation doping. From the viewpoint of graphene fabrication, a degradation in crystallinity comes with higher thickness of graphene. The e-HOPG becomes our approach to mimic the high crystallinity of MLG for $MoCl_5$ intercalation doping as using the process guideline from the optimization of FLG. Doping efficiency, reduction

of sheet resistance, and damage were analyzed and summarized based on the scientific discussion. This helped create guidelines for the $MoCl_5$ intercalation process of lower crystallinity MLG.

For graphene inductor device fabrication, MLG from the CVD process was implemented, along with the $MoCl_5$ intercalation process. MLG on Ni catalyst is used to study the $MoCl_5$ intercalation process and to propose patterned MLG for graphene inductor fabrication. To reach the goal of inductor applications, the reduction of sheet resistance of MLG doped from the $MoCl_5$ intercalation process are also analyzed and discussed to provide guidelines for the $MoCl_5$ intercalation process.

1.5. Structure of the thesis

This dissertation is divided into seven chapters, as shown in Fig. 1.10, which can be briefly described as follows.

Chapter 1 consists of the background and objectives of this thesis. Explanation regarding the expected applications of doped graphene, in terms of low resistance and high-inductance, the intercalation doping process, and an important review of previous work related to this thesis are also provided. The previous reviews were discussed to design the process guideline based on this scientific discussion. Finally, the aim and approach to reach the goal of the thesis are also discussed in this chapter.

Chapter 2 consists of the material and methods used in experiments discussed in this thesis. An explanation of FLG and MLG fabrication by the CVD process, e-HOPG preparation to mimic the high crystallinity of MLG, and the $MoCl_5$ intercalation process are included. Characterization techniques used for doped graphene, such as Raman spectroscopy, scanning electron microscopy, atomic force microscopy (AFM), optical microscopy, laser microscopy, and the four-point probe method for measuring sheet resistance are also described in this chapter.

Chapter 3 consists of experiments, results, and discussion of $MoCl_5$ intercalation in CVD FLG transferred on a SiO_2/Si substrate. The reaction temperature dependence, reaction time dependence, and chemical concentration dependence of $MoCl_5$ intercalation of FLG are

optimized from the viewpoint of effective doping and low damage. The uniformity of the intercalation area, the effect of $MoCl_5$ intercalation on the crystallinity of FLG, and the mechanism of $MoCl_5$ intercalation in FLG are also discussed in this chapter.

Chapter 4 consists of experiments, results, and discussion of $MoCl_5$ intercalation in e-HOPG. The e-HOPG was used to mimic doping in thick MLG films with high crystallinity. The reaction temperature dependence, reaction time dependence, and chemical concentration dependence of $MoCl_5$ intercalation in e-HOPG are investigated in terms of doping efficiency and damage. Correlation plots of G and 2D peak positions in Raman spectra were analyzed to determine the strain and carrier density of doped e-HOPG. The stability of doping efficiency, sheet resistance characterization, and the mechanism of damage in e-HOPG during $MoCl_5$ intercalation are also described in this chapter.

Chapter 5 consists of experiments, results, and discussion of $MoCl_5$ intercalation in CVD-MLG on Ni catalyst. G/D ratios of CVD-MLG varied with variation in CVD growth temperature. The optimization of $MoCl_5$ intercalation to CVD-MLG in terms of the G/D ratio dependence, and the reaction temperature dependence using the STD/5 chemical concentration in this chapter. The simultaneous doping/etching process of CVD-multilayer graphene on Ni and sheet resistance is also discussed in this chapter.

Chapter 6 consists of the fabrication and characterization of patterned CVD-MLG. Experiments, results, and discussion of $MoCl_5$ intercalation in the pattern of CVD-MLG are reported in this chapter. The uniformity of the doping area and the characterization of electrical properties in terms of the four terminals and the transmission line measurement pattering methods are also discussed in this chapter.

Chapter 7 summarizes all results of this thesis. The conclusion of our present work is also given. The prospects of future work are also given in this chapter.

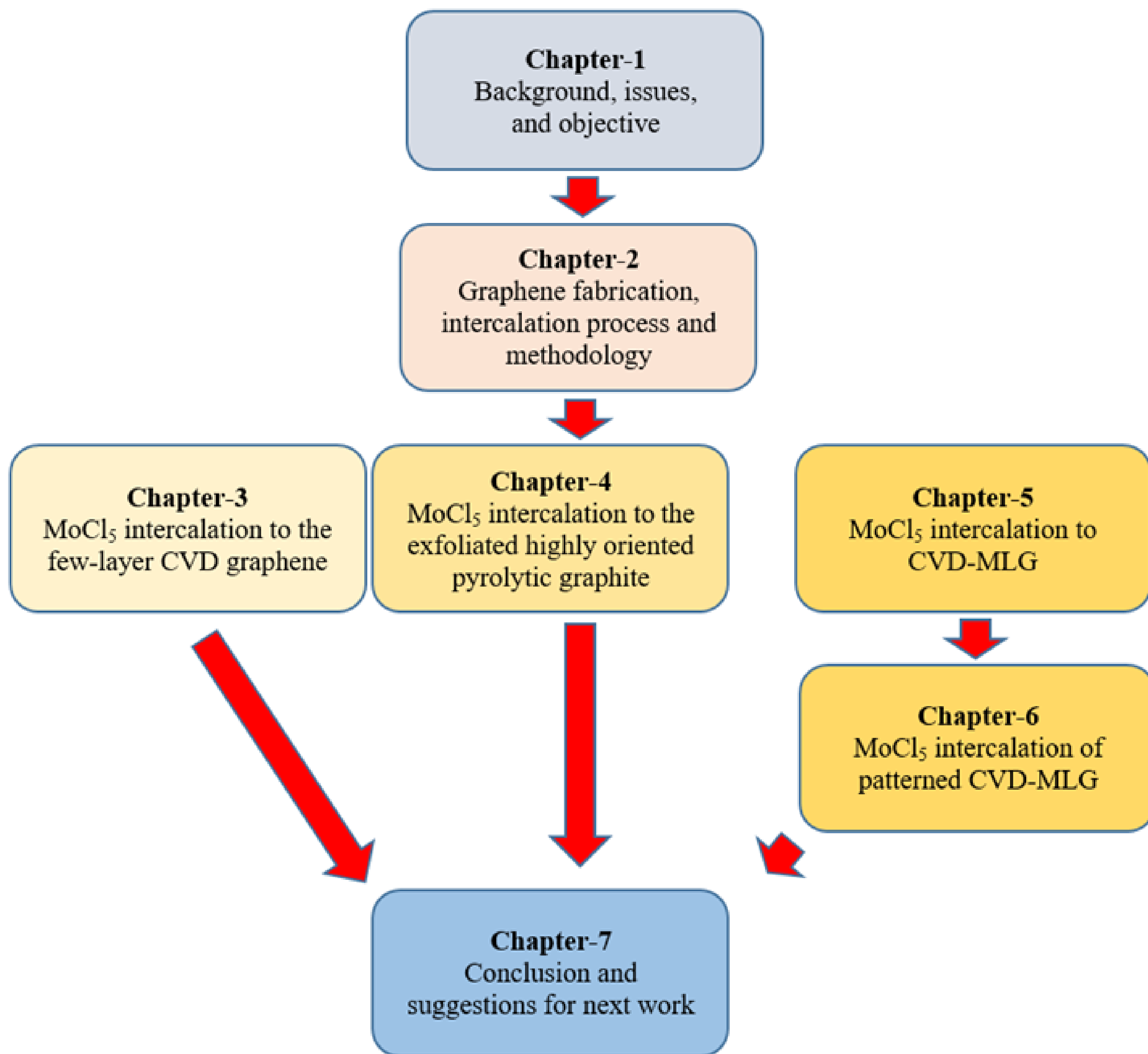

Figure 1.10. Flowchart of this dissertation.

References

[1] W. Ejaz, A. Anpalagan, M.A. Imran, M. Jo, M. Naeem, S.B. Qaisar and W. Wang: IEEE Access. **4**, 10310 (2016).

[2] A. Tikhomirov, E. Omelyanchuk and A. Semenova: 2018 Systems of Signals Generating and Processing in the Field of on Board Communications, p. 1 (2018).

[3] A. Phan and S. T. Qureshi, "5G impact on smart cities", www.researchgate.net/publication/315804922, 06 April 2017.

[4] C. Colman-Meixner, P. Diogo, M.S. Siddiqui, A. Albanese, H. Khalili, A. Mavromatis, L. Luca, A. Ulisses, J. Colom and R. Nejabati: 2018 IEEE International Symposium on Broadband Multimedia Systems and Broadcasting (BMSB), p. 1 (2018).

[5] J.A. Manrique, J.S. Rueda-Rueda and J.M. Portocarrero: 2016 IEEE international conference on Internet of Things (iThings) and IEEE green computing and communications (GreenCom) and IEEE cyber, physical and social computing (CPSCom) and IEEE smart data (SmartData), p. 252 (2016).

[6] J. Jiang, J. Kang, J.H. Chu and K. Banerjee, Proc. IEEE Int. Electron Devices Meeting, 2017, p. 14.3.1.

[7] S. Dutta, S. Kundu, A. Gupta, G. Jamieson, J.F.G. Granados, J. Bömmels, C.J. Wilson, Z. Tőkei and C. Adelmann, IEEE Electron Device Lett. **38**, 949 (2017).

[8] P.R. Wallace: Physical review. **71**, 622 (1947).

[9] G. Yang, L. Li, W.B. Lee and M.C. Ng: Science and technology of advanced materials. **19** [1], 613 (2018).

[10] K.S. Novoselov, A.K. Geim, S.V. Morozov, D. Jiang, Y. Zhang, S.V. Dubonos, I.V. Grigorieva and A.A. Firsov: science. **306**, 666 (2004).

[11] A.C. Neto, F. Guinea, N.M. Peres, K.S. Novoselov and A.K. Geim: Reviews of modern physics. **81**, 109 (2009).

[12] X. Chen, L. Zhang and S. Chen: Synthetic Metals. **210,** 95 (2015).

[13] C. Mattevi, H. Kim and M. Chhowalla: Journal of Materials Chemistry. **21,** 3324 (2011).

[14] W. Zhang, L. Wu, Z. Li and Y. Liu: RSC Advances. **5**, 49521 (2015).

[15] K.S. Mali, J. Greenwood, J. Adisoejoso, R. Phillipson and S. De Feyter: Nanoscale. **7**, 1566 (2015).

[16] F. Schedin, A. K. Geim, S. V. Morozov, E. W. Hill, P. Blake and M. I. Katsnelson, Nat. Mater., **6**, 652 (2007).

[17] H. Xu, L. Ma and Z. Jin: Journal of energy chemistry. **27**, 146 (2018).

[18] J. Han, L. L. Zhang, S. Lee, J. Oh, K.-S. Lee, J. R. Potts, J. Ji, X. Zhao, R. S. Ruoff and S. Park, ACS Nano, **7**, 19 (2013).

[19] D. Deng, X. Pan, L. Yu, Y. Cui, Y. Jiang, J. Qi, W.-X. Li, Q. Fu, X. Ma, Q. Xue, G. Sun and X. Bao, Chem. Mater., **23**, 1188 (2011).

[20] T. Enoki, M. Suzuki, and M. Endo, Graphite intercalation compounds and applications. Oxford University Press, 2003.

[21] M. Katagiri, H. Miyazaki, R. Matsumoto, A. Kajita and T. Sakai: Japanese Journal of Applied Physics. **56**, 07KD01 (2017).

[22] Z. Tokei, Scaling the BEOL – a toolbox filled with new processes, boosters and conductors, imec magazine September 2019

[23] P. McLellan, “IEDM: Novel Interconnect Techniques Beyond 3nm”, https://community.cadence.com/cadence_blogs_8/b/breakfast-bytes/posts/iedm5, 28 Jan 2020.

[24] X. Wu, I. Asselberghs, C. Huyghebaert, A. Contino, B. Soree, M. Heyns and Z. Tokei, Proc. IEEE Int. Interconnect Technology Conf., 2018, p. 25.

[25] X. Wu, Y. Chuang, A. Contino, B. Sorée, S. Brems, Z. Tokei, M. Heyns, C. Huyghebaert and I. Asselberghs, Adv. Mater. Interfaces. **5**, 1800454 (2018).

[26] J. Jiang, J. Kang, W. Cao, X. Xie, H. Zhang, J.H. Chu, W. Liu and K. Banerjee, Nano Lett. **17**, 1482 (2017).

[27] M. Politou, W. Xiangyu, A. Contino, B. Soree, C. Huyghebaert, D. Lin, I. Radu, Z. Tokei and I. Asselberghs, Proc. IEEE Int. Interconnect Technology Conf. / Advanced Metallization Conf., 2016, p. 200.

[28] C. Xu, H. Li and K. Banerjee: IEEE transactions on electron devices. **56**, 1567 (2009).

[29] M. Inagaki and G. Watanabe: Synthetic metals. 94 235 (1998).

[30] J. Mittal and M. Inagaki: Synthetic metals. 92 87 (1998).

[31] J. Kang, Y. Matsumoto, X. Li, J. Jiang, X. Xie, K. Kawamoto, M. Kenmoku, J.H. Chu, W. Liu and J. Mao: Nature Electronics. **1**, 46 (2018).

[32] K. Agashiwala, A. Pal, W. Cao, J. Jiang and K. Banerjee: 2018 IEEE International Electron Devices Meeting (IEDM), p. 24.4. 1 (2018).

[33] J. Nathaniel and X. Wanga: Applied physics letters. **100**. 213112 (2012).

[34] K. Tasaki: The Journal of Physical Chemistry C. **118**. 1443−1450 (2014).

[35] W. Zhao, P.H. Tan, J. Liu and A.C. Ferrari: Journal of the American Chemical Society. **133**, 5941 (2011).

[36] Q. Chen, L. Zhang and H. Zhu: Nano Research. **11**, 440 (2018).

[37] K. Ueno, R. Kosugi, K. Imazeki, A. Aozasa, Y. Matsumoto, H. Miyazaki, N. Sakuma, A. Kajita and T. Sakai: Japanese Journal of Applied Physics. **53**, 05GC02 (2014).

[38] R. Matsumoto and Y. Okabe: Synthetic Metals. **212**, 62 (2016).

[39] D. Kondo, H. Nakano, B. Zhou, I. Akiko, K. Hayashi, M. Takahashi, S. Sato and N. Yokoyama: IEEE International Interconnect Technology Conference, p. 189 (2014).

[40] K. Kawamoto, Y. Saito, M. Kenmoku and K. Ueno: 2017 IEEE Electron Devices Technology and Manufacturing Conference (EDTM), p. 252 (2017).

[41] H. Miyazaki, R. Matsumoto, M. Katagiri, T. Yoshida, K. Ueno, T. Sakai and A. Kajita: Japanese Journal of Applied Physics. **56**, 04CP02 (2017).

[42] H. Kinoshita, I. Jeon, M. Maruyama, K. Kawahara, Y. Terao, D. Ding, R. Matsumoto, Y. Matsuo, S. Okada and H. Ago: Advanced Materials. **29**, 1702141 (2017).

CHAPTER 2
GRAPHENE FABRICATION, INTERCALATION PROCESS, AND METHODOLOGY

2.1 Overview

The objective of this study is to investigate the $MoCl_5$ intercalation process of different types of graphene layers, such as transferred few-layer graphene (FLG) and MLG on Ni catalyst from CVD processes and thick MLG with high crystallinity from e-highly oriented pyrolytic graphite (e-HOPG). The type of graphene and its thickness depends on the requirement of device applications. However, there is a trade-off between doping efficacy and damage. Therefore, optimization needs to made and the mechanics need to be described, as introduced in the previous chapter. The details of graphene fabrication are shown in Table 2.1. The $MoCl_5$ intercalation doping process and the characterization of doped graphene is described in this chapter.

Table 2.1 Summary of graphene fabrication methods.

Type of graphene	Fabrication method
Few-layer graphene (FLG)	CVD process using Pt foil catalyst
Thick multilayer graphene (MLG)	The exfoliated film from highly oriented pyrolytic graphite (HOPG)
Multilayer graphene (MLG)	CVD process using Ni catalyst

2.2 Graphene fabrication

Graphene fabrication or growth techniques effect the quality of graphene. For device applications, such as interconnects and inductors, differences in thickness and graphene quality is considered as appropriate for each device application. The graphene used in this study consists of transferred FLG from the CVD process, MLG on Ni catalyst from the CVD

process, and thick MLG with high crystallinity from e-HOPG. Fabrication of each type of graphene is described in detail as follows.

2.2.1 Few-layer graphene fabrication

The FLG used in this experiment was grown and transferred by Interuniversity Microelectronics Center (imec), Belgium. The FLG was fabricated under the same conditions to control the quality of graphene. After transferring to a SiO_2 substrate, the FLG was shipped to the Nanoelectronic laboratory, Shibaura Institute of Technology. After arriving, the FLG was kept in a N_2 box until the intercalation experiment. The process to fabricate the FLG from imec follows.

2.2.1.1 Few-layer graphene growth

The FLG was grown on 50-μm thick Pt foils (99.99% trace metal basis, Alfa Aesar) in a vertical cold-wall AIXTRON Black Magic Pro 6″ CVD system. The reactor was heated from room temperature to 980°C with a hydrogen flow rate at 800 sccm. The pressure of the reactor was controlled at 750 mbar for the entire growth process. After reaching 980°C, methane with a flow rate of 5 sccm was introduced to the chamber for 20 min. After the FLG growth process, the reactor was cooled down to room temperature at a cooling rate of 15°C/min under a flow rate ratio of methane and hydrogen of 4:800 sccm [1-4].

2.2.1.2 Few-layer graphene transfer process

After the growth process, FLG on the Pt foil substrate was submerged in ultrapure water (UPW) at 80°C for 16 h to achieve water intercalation. The support polymer, polymethyl methacrylate (PMMA), was spin-coated on the FLG on Pt foil and baked at 135°C for 10 min. After the baking process, the PMMA on the FLG was delaminated from the Pt foil by electrolysis in NaOH (0.2 M) at −3 V. The sample was connected as the working electrode and a Pt wire as the auxiliary electrode. Both electrodes were submerged in the NaOH electrolyte. After the electrolysis process, the PMMA on FLG was rinsed in UPW and subsequently transferred to a SiO_2/Si target substrate. After transferring, the PMMA/FLG on

SiO_2/Si substrate was annealed in vacuum at 50°C overnight. To remove the PMMA support layer, the sample was dissolved in hot acetone at 50°C overnight. After drying, the FLG on SiO_2/Si substrate was packed in a vacuum package and shipped to the Nanoelectronic laboratory, Shibaura Institute of Technology [1-4].

2.2.2 Multilayer graphene fabrication

MLG is expected to be used, after fabrication with the conventional method, for device applications. Here, MLG fabrication on a Ni catalyst using CVD process will be described. MLG fabrication can be separated into three steps:

1. substrate cleaning,
2. Ni catalyst deposition,
3. MLG growth.

Figure 2.1 shows the flow of MLG fabrication on a Ni catalyst by the CVD process. The details of each step of the MLG fabrication process follows.

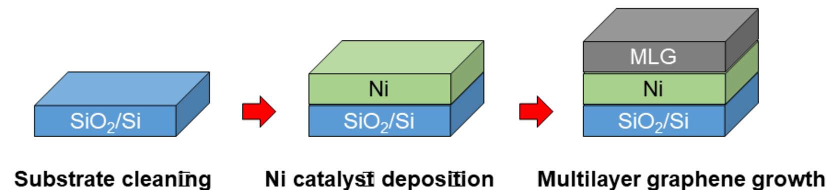

Figure 2.1. Flow of MLG fabrication on Ni catalyst from the CVD process.

2.2.2.1 Substrate cleaning

The 100-nm SiO_2 layer on a 725-μm-thick Si substrate was selected for MLG fabrication on a Ni catalyst by CVD process. The cleaning procedure used for the SiO_2/Si substrate before Ni catalyst deposition is described below.

1. The SiO_2/Si substrate was submerged into a Teflon container containing sulfuric acid (H_2SO_4) and hydrogen peroxide (H_2O_2) with a 4:1 H_2SO_4:H_2O_2 volume ratio. While submerged, the SiO_2/Si substrate was shaken for 10 min to flush the substrate surface.
2. The SiO_2/Si substrate was rinsed of excess chemical in UPW twice.

3. The SiO_2/Si substrate was soaked in a glass beaker with UPW and then ultra-sonicated for 5 min.
4. The SiO_2/Si substrate was blown by N_2 gas to remove the water on the surface.
5. Finally, the SiO_2/Si substrate was baked at 115°C for 10 min.

2.2.2.2 Ni catalyst deposition

Direct current (DC) magnetron sputtering (Shibaura, CFS-4EP-LL i-miller) was used to deposit a Ni thin film as the metal catalyst for MLG fabrication due to the conductivity of the Ni target. Figure 2.2 shows a schematic diagram of the DC magnetron sputtering system. The 3-inch-diameter Ni target was installed at the sputtering gun on the top of magnets. The SiO_2/Si substrate was loaded into the substrate holder, after the final baking from the cleaning process. The DC magnetron sputtering system was connected to a vacuum pump. Before the deposition process, the vacuum chamber was pumped down to a base pressure below 7×10^{-4} Pa. After reaching the base pressure, Ar gas was flowed into the vacuum chamber at a flow rate of 20 sccm. After reaching the working pressure, a DC power of 100 W was supplied to the system. Under low pressure and with the electrical field, the Ar gas is ionized to the plasma stage. During the Ar ionization process, the Ni target is bombarded by Ar ions (Ar^+). The collision between Ar^+ and Ni atoms on the surface of the Ni target ejects sputtered Ni atoms. The sputtered atoms can be moved to the substrate by kinetic energy and subsequently start to form the Ni thin film on the surface of the substrate. The substrate was rotated with a rotation rate of 20 rpm for uniformity improvement during deposition. The deposition rate was fixed at 0.11 nm/sec at room temperature. The thickness of the Ni film can be controlled by the deposition time. After obtaining the appropriate Ni thickness, the DC power supply was stopped and the substrate was removed. The Ni thin film was kept in a N_2 box until the next step of the experiment.

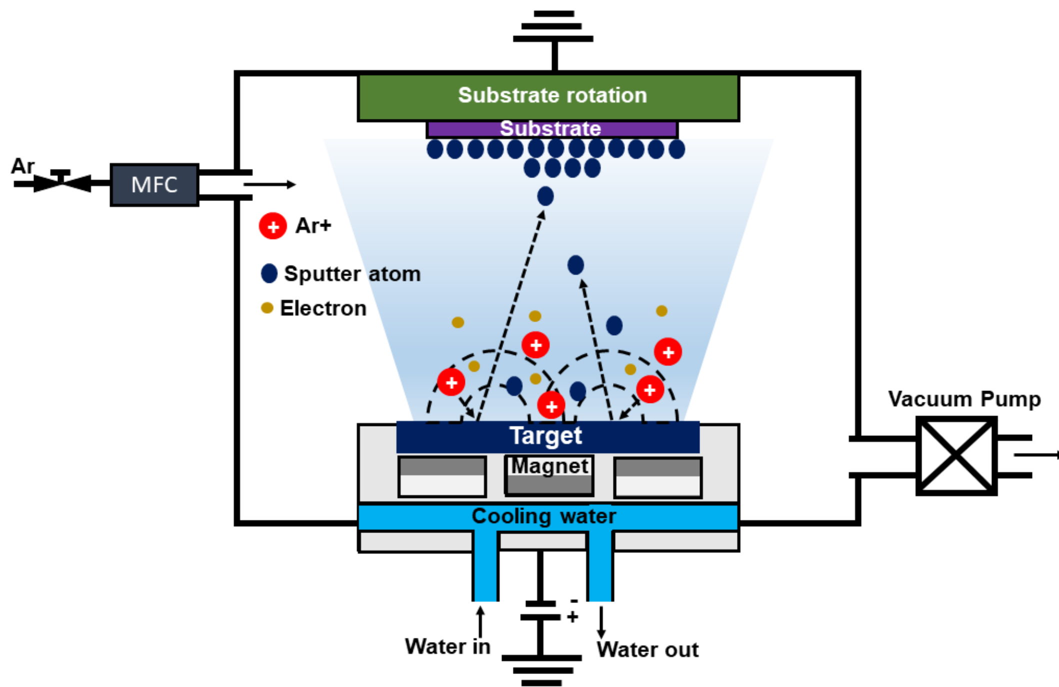

Figure 2.2. Schematic diagram of the DC magnetron sputtering system.

2.2.2.3 Multilayer graphene growth

MLG was grown by the CVD process. Figure 2.3 shows a schematic diagram of MLG growth by CVD. The Ni thin film was selected as the transition metal catalyst for MLG growth [5-8]. The Ni thin film on the SiO_2/Si substrate was placed in a quartz boat, which was then inserted into a quartz tube at the center of an electric furnace. After end closing the quartz tube, Ar was flowed through the tube at a flow rate at 500 sccm for 45 min by opening the V_1 and V_2 valves. After 45 min, the proportional-integral-derivative controller of the electric furnace was set with the heating parameters and turned the heater on. After obtaining the target temperature, the Ar was set to the growth flow rate by opening the V_3 and V_4 valves. MLG began growing after the V_2 valve was closed. The vapor of ethanol was carried by Ar gas to the quartz tube. The electric furnace was turned off at the same time V_2 opened and subsequently by V_3 and V_4 closing. The ethanol vapor is a hydrocarbon derivative and can be decomposed on the Ni catalyst surface at high temperature. The carbon can be dissolved to the Ni after decomposition. The fraction of carbon atoms in Ni at high

temperature is precipitated to form a MLG film upon cooling [3-4]. After the temperature was below 70°C, the sample was removed from the CVD setup and kept in a N_2 box until the next experimental step.

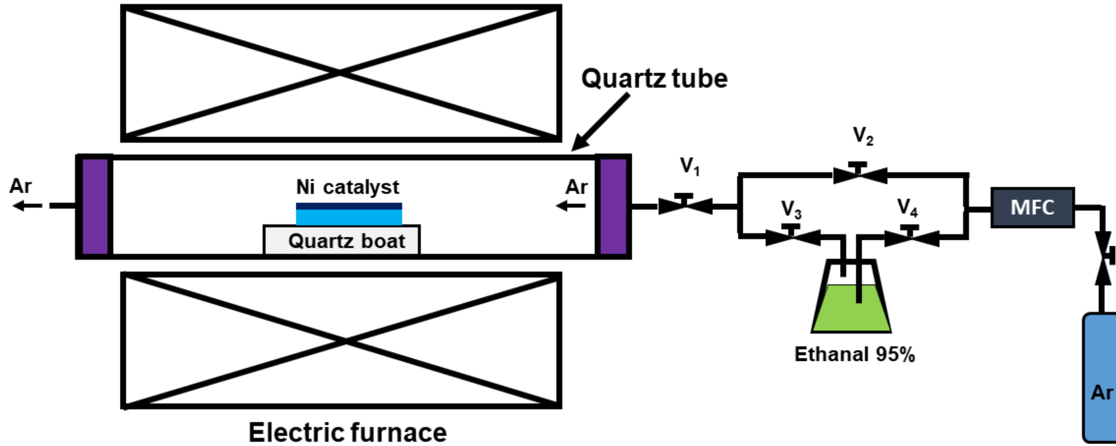

Figure 2.3. Schematic diagram of the MLG growth process by CVD.

2.2.3 Exfoliated highly oriented pyrolytic graphite preparation

An e-HOPG film was used to mimic the high crystallinity of thick MLG. Figure 2.4 shows a schematic diagram of e-HOPG on a SiO_2/Si substrate. The exfoliating and transferring starts from pasting thermal detachment tape on the surface of highly oriented pyrolytic graphite (SPI-Grade-1, ZYA). After peeling the thermal detachment tape from the surface of HOPG, the exfoliated film with a thickness of about 10 μm was taped with thermal detachment tape and the e-HOPG/scotch tape was pasted on the surface of a SiO_2/Si substrate heated to 110°C on a hot plate. The glue of the thermal detachment tape deteriorated after heating and subsequently led to the transfer of the e-HOPG film onto the SiO_2/Si substrate. After cooling, the e-HOPG film on the SiO_2/Si substrate was kept in a N_2 box until the next step of the experiment.

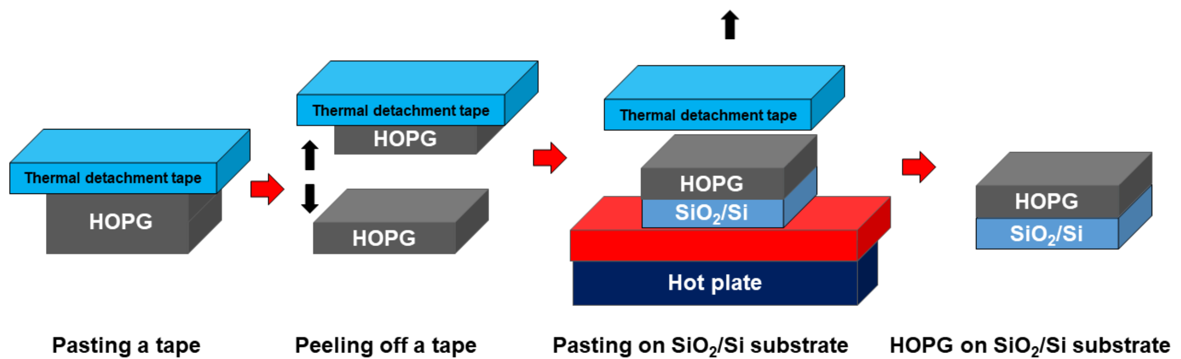

Figure 2.4. Schematic diagram of e-HOPG placement onto a SiO_2/Si substrate.

2.3 $MoCl_5$ intercalation

GIC doping was used to study $MoCl_5$ doping in FLG, e-HOPG as a thick multilayer film, and CVD-MLG on Ni catalyst. Figure 2.5 shows a schematic diagram of the experimental setup for the $MoCl_5$ intercalation process. The sample was inserted into a glass capsule with molybdenum (V) chloride (99.6%, Alfa Aesar) and molybdenum (VI) oxide (99.5%, Kanto Kagaku. Ltd) at a constant molar ratio of 1:0.37 and pyrolytic graphite sheet (PGS). After enclosing the glass capsule, it was inserted into a glass tube. Ar gas was flowed through the glass tube for 10 min. Before the reaction, the glass tube was pre-annealed at 110 ºC for 120 min in an Ar-atmosphere to dry out water. After pre-annealing for 120 min, the electric furnace was set to the reaction temperature with a heating rate of 10 ºC/min. The pre-annealing and reaction temperatures were maintained at a stable temperature during the experiment. After the reaction temperature was stable, the electric furnace was turned off after obtaining the target reaction time. The table 2.2 shows the summary of $MoCl_5$ intercalation doping conditions. MoO_3 was used to accelerate the intercalation reaction and to reduce the time and temperature for the formation of low stage $MoCl_5$-GICs, i.e. higher doping. The molar ratio between $MoCl_5$ and MoO_3 was kept at 1:0.37 which was optimized J. Mittal et. al. for all of the chemical amount conditions [9]. The sample was removed after natural cooling in atmosphere. The doped graphene sample was kept in a N_2 box until undergoing characterization processes.

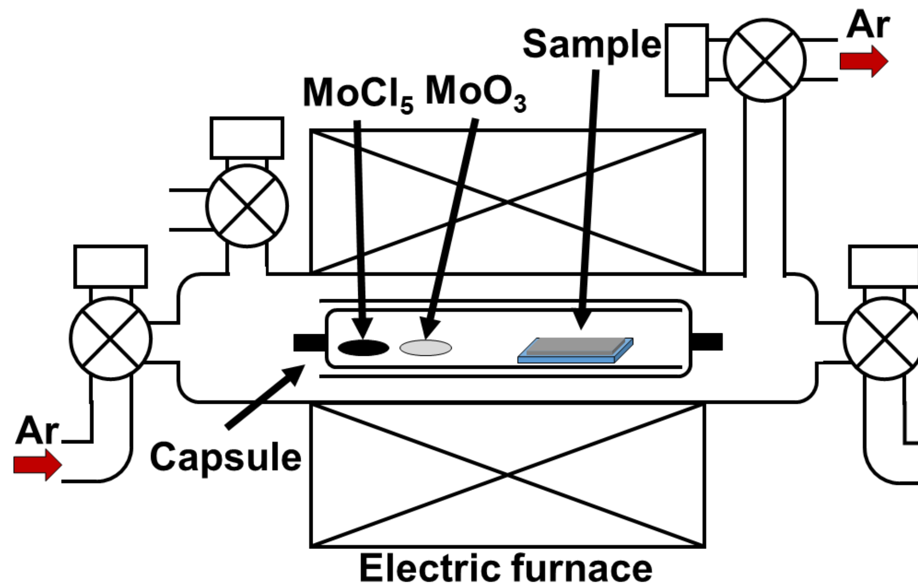

Figure 2.5. Schematic diagram of the experimental setup for the $MoCl_5$ intercalation process.

Table 2.2 Summary of $MoCl_5$ intercalation doping conditions.

Chapter	Chemical amount			Temperature (°C)	Time (min)
		$MoCl_5$ (g)	MoO_3 (g)		
Chapter 3	High	0.3412	0.0665	130, 150, 250	30, 60
	Reduce	0.1706	0.0332	150, 175, 200	60, 90, 120
Chapter 4	STD	0.1706	0.0332	200, 225, 250	5, 10, 15, 30
	STD/2	0.0853	0.0166		
	STD/4	0.0427	0.0083		
	STD/5	0.0374	0.0073		
	STD/6	0.0284	0.0055		
Chapter 5	STD/5	0.0374	0.0073	225, 250, 300	30
Chapter 6	STD/5	0.0374	0.0073	300	30

2.4 Metal electrode fabrication

The resistance reduction of doped graphene after the $MoCl_5$ intercalation process was investigated as the intercalation parameters were changed. An evaporation deposition system (Shikuu, VE-2020) was used to create metal electrodes for electrical properties characterization. Figure 2.6 shows a schematic diagram of the evaporator system for metal electrode deposition. The sample was installed onto the substrate holder by pasting stainless steel on the top of the sample. The tungsten filament (Nilaco, LF305W) was bound by metal wire at the V-shape of the filament. The thickness of the metal film was controlled by the volume of metal wire. Then, the filament was installed to the filament slot and the distance between the filament and sample was adjusted. The system was then pumped down to the base pressure as below 1.0×10^{-2} Pa. After reaching the base pressure, the shutter was opened and the power supply current was increased. After increasing the current, the atoms of the

metal wire were evaporated and moved to the sample to form a thin metal film. After venting the vacuum system, the sample was removed and kept in a N_2 box until characterized.

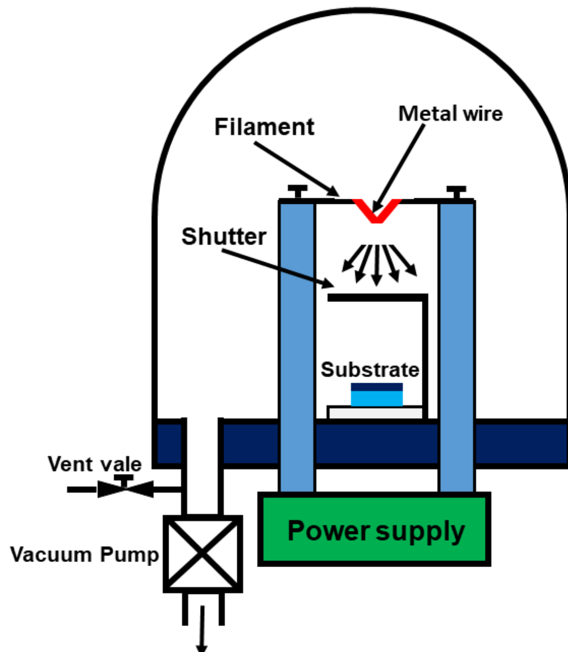

Figure 2.6. Schematic diagram of the evaporator system for metal electrode deposition.

2.5 Methodology

To investigate and optimize the $MoCl_5$ intercalation process, doping efficiency and damage of graphene were characterized. To evaluate the doping efficiency of graphene, Raman spectroscopy was used to indicate the doping stages, the crystallinity of graphene, and the uniformity of the doping area. Scanning electron microscopy (SEM) and the optical microscopy were used to observe the morphology of the graphene. Atomic force microscopy (AFM) and laser microscopy were used to analyze the surface morphology and compare RMS roughness before and after the $MoCl_5$ intercalation process. Finally, the electrical properties before and after the $MoCl_5$ intercalation process were evaluated by the four-point probe method. The details of each characterization method follow.

2.5.1 Raman spectroscopy

Raman spectroscopy is a favored technique for analysis of chemical and structural information of various compounds that measures vibrational states of a molecule or compound. A Raman spectroscope (HORIBA, HR-Evolution) was used to characterize graphene before and after the $MoCl_5$ intercalation process. A 532-nm laser was used to excite the sample. The phenomena between the excitation laser and the sample molecule can be described as an electronic excited state, as shown schematically in Figure 2.7. When the molecule is excited by the energy of the incident laser, the energy is mostly scattered with the same frequency as the incident laser, which is called Rayleigh scattering. A few incident photons interact and exchange energy with the molecular bond vibration, which leads to inelastic scattered light that is called Raman scattering. The scattered photon that is lower in energy than the incident photon energy is called the red-shifted Stokes photon. However, the scattered photons with energy higher than the incident energy are called blue-shifted anti-Stokes photons. The difference in frequency between incident and scattered photons is typically called the Raman shift and corresponds to the vibrational energy level of a molecule [10-15].

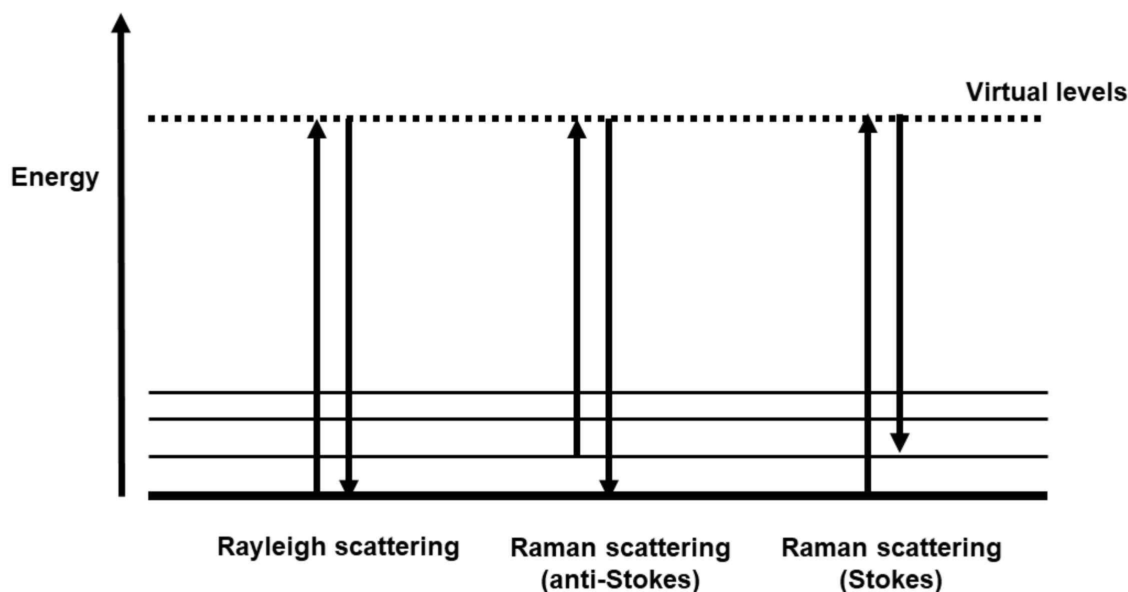

Figure 2.7. Schematic diagram of Raman scattering phenomena.

For Raman spectroscopy characterization of graphene, the G-, D-, and 2D-bands were used to investigate the properties of graphene before and after intercalation by $MoCl_5$. Figure 2.8 shows Raman spectra of graphene that consists of the G-, D-, and 2D-bands. The G-band corresponds to the in-plane motion of carbon atoms and is located at ~1580 cm^{-1}. The G-band is sensitive to strain effects and is used to indicate the number of graphene layers. The G-band also corresponds to doping and both the position and line width of this band can be used to monitor the doping level. The D-band corresponds to lattice motion away from the center of the Brillouin zone and is located between 1270 and 1450 cm^{-1}, depending on the excitation wavelength. The D-band represents phonons easily absorbed by defects, which explains why the D-band is normally used to determine the quality of graphene sheets. The 2D-band or second-order D band is due to a double resonance process at approximately 2700 cm^{-1}. When the number of graphene layers increases, the number of double resonance processes also increases. Therefore, the intensity of the 2D-band can be used to determine the number of graphene layers in comparison with the G band. The Raman scattered modes significant to graphene are shown in Table 2.1.

The ratio of intensity between the G-band and D-band corresponds to the crystallite size of graphene. The crystallite size of graphene can also be determined from the G/D ratio using the following equation [16],

$$L_a(nm) = (2.4 \times 10^{-10})\lambda_l^4 \left(\frac{I_D}{I_G}\right)^{-1} \quad (2.1)$$

Where L_a is the crystallite size of graphene, λ_l is the wavelength of the excitation laser used in Raman spectroscopy, and I_D and I_G are the intensities of the D and G peaks, respectively.

Raman mapping was also used in this study to indicate the uniformity of the intercalation doping area.

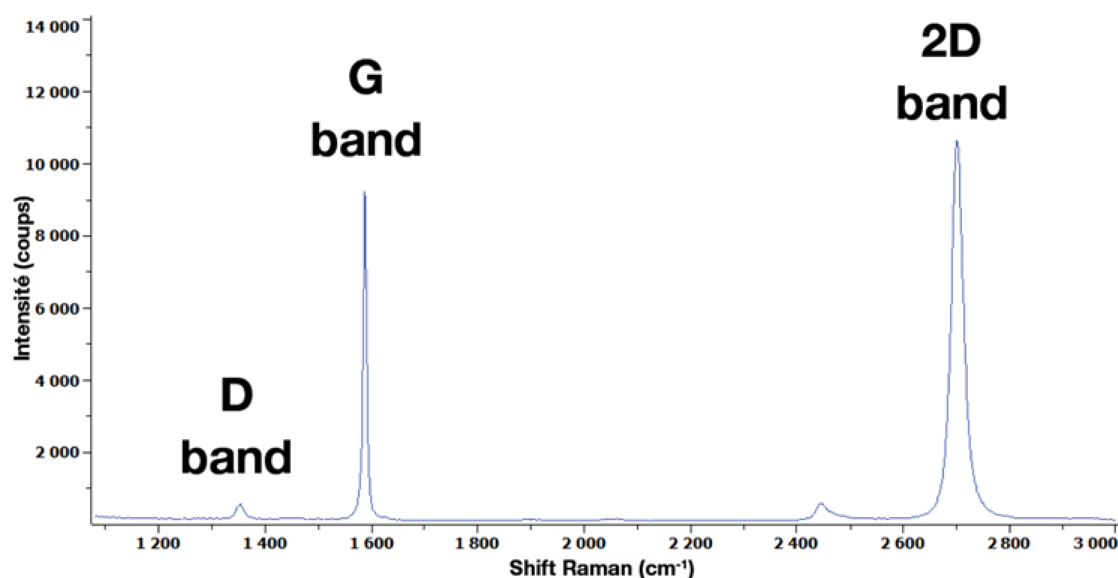

Figure 2.8. Raman spectra of graphene [15].

Table 2.3. Relevant Raman spectra modes of graphene and their significance [16].

Mode	Position (cm^{-1})	Significance
G	~1580	Originates from graphitic structure and the intensity of the peak increases with increasing number of graphene layers
D	~1350	Originates from defect structures, such as edges and grain boundaries
2D	~2700	Second order effect of the D band used to determine the number of graphene layers

2.5.2 Scanning electron microscopy

SEM is high magnification microscopy that is generally used for micrometer or nanometer scale observation. A field emission SEM (JEOL, JSM-7610F) was used to observe the morphology of graphene. The emission electrons were produced from a Schottky emitter electron source by a high electric field. The emission electrons are accelerated and controlled using condenser and objective lenses. A scanning coil is used to scan the surface of the sample. Figure 2.9 shows the emitted signals from the interaction between emission electrons and the sample surface. These signals are collected by one or more detectors to form images. The secondary electron is the main signal used to observe sample morphology.

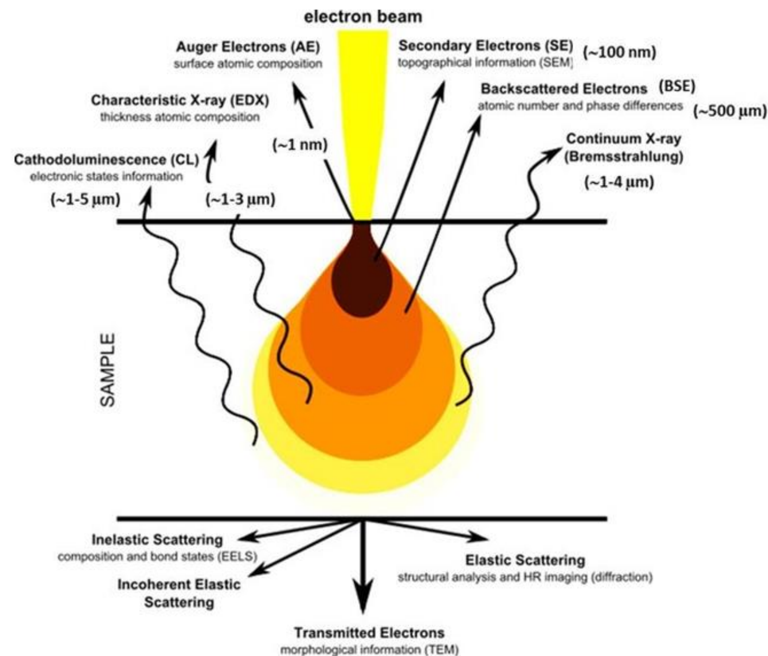

Figure 2.9. Signals emitted from different regions of the interaction volume [18].

2.5.3 Energy dispersive X-ray analysis (EDX)

EDX analysis is a chemical characterization or elemental analysis technique that is included in SEM system. From signals emitted from the electron beam and samples, the characteristic X-ray is used to analyze elemental and chemical composition. Figure 2.10 shows the principle of characteristic X-rays used for EDX analysis. After the primary

electron from the electron beam hits the electron in the shell of an atom, the electron is knocked from the shell. This vacancy is filled by an electron from an outer shell (higher energy level to lower energy level). The difference of energy leads to the release of an X-ray. The energy of this X-ray is unique to the specific element and transition and is called a characteristic X-ray. EDX analysis in this study, with the field emission SEM (JEOL, JSM-7610F) and SEM (Shimazu, SSX-550M), were used to analyze the composition of graphene.

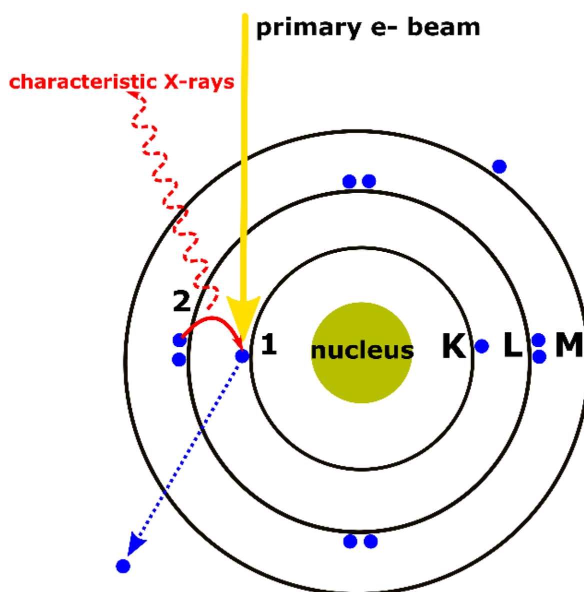

Figure 2.10. Illustration of the principle of characteristic X-rays used for EDX analysis [19].

2.5.4 Atomic force microscopy

AFM a surface morphology characterization technique. An AFM (HITACHI, AFM5000II) in dynamic force microscope mode was used to characterize the surface morphology and RMS roughness of graphene before and after intercalation. Figure 2.11 shows a schematic illustration of AFM. The tip of a scanning probe is scanned across a sample surface at very small distances. The AFM consists of three basic modes: contact, non-contact, and tapping. Tapping mode provides high resolution imaging and avoids dragging

of the tip across the surface as this mode uses an oscillating cantilever to contact the surface for image topography.

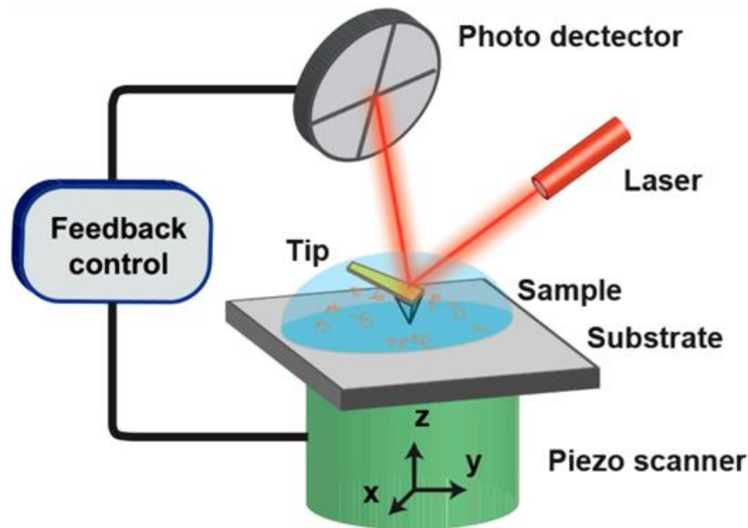

Figure 2.11. Schematic illustration of atomic force microscopy (AFM) [20].

2.5.5 Laser scanning microscopy

Laser scanning microscopy is a 3D morphology observation technique. A laser scanning microscope (Olympus, OLS4000) was used to characterize the surface morphology and RMS roughness in a larger area than that of AFM for e-HOPG and multilayer graphene before and after intercalation. Figure 2.12 shows the composition of a confocal laser scanning microscope. The pinhole of the confocal optical system was installed to detect light only at the focused position. Topography mapping, depth of focus, and 3D visualization were produced from the emitted light from the point light source on the sample.

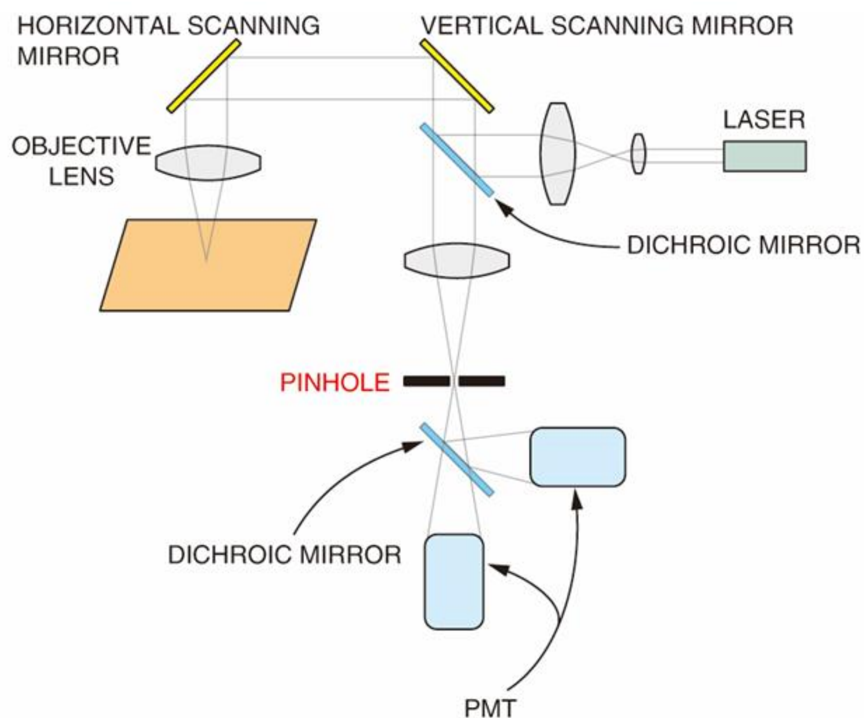

Figure 2.12. Schematic of a confocal laser scanning microscope [21].

2.5.6 Optical microscopy

Optical microscopy was used to observe the morphology of graphene before and after $MoCl_5$ intercalation and used to distinguish the number of FLG layers. Figure 2.13 shows the basic construction of an optical microscopes. After turning on the lamp, the path of light is controlled by the filter cube and tube lens. The magnification of an optical microscope can be adjusted by the objective lens. A charged cooling device camera is used to save the morphology photo to a digital file.

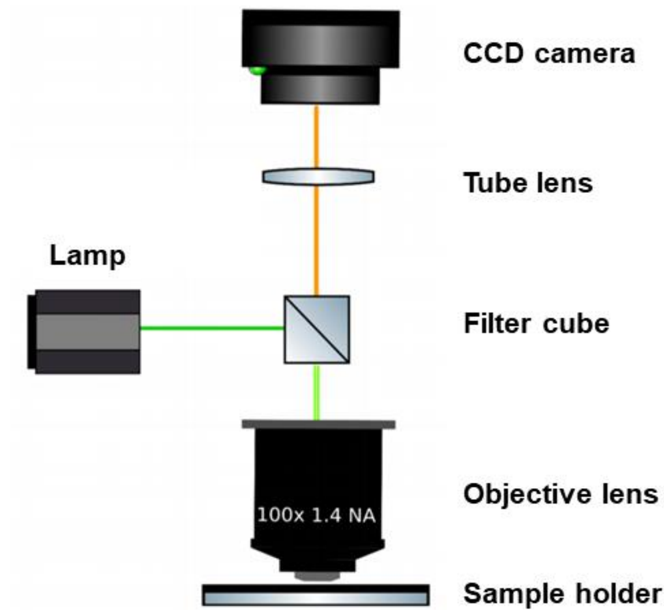

Figure 2.13. Basic construction of an optical microscope [22].

2.5.7 Four-probe method

Electrical properties before and after the $MoCl_5$ intercalation process were evaluated using a four-probe method. A resistance meter (HIOKI, RM3544) was used as a source and meter for the four-probe measurement. In the case of large area MLG and e-HOPG films, the linear four-probe method was used to characterized the sheet resistance change before and after the $MoCl_5$ intercalation process. Figure 2.14 shows a schematic diagram of a linear four-probe. The linear four-probe system consists of four conductive pins located the same distance apart. A DC current is applied from the outer pins and a different voltage is sensed from the inner pins. The sheet resistance can be calculated using the following equation [23],

$$R_s = \frac{\pi}{lnln\,(2)}\frac{V}{I}, \quad (2.2)$$

where R_s is the sheet resistance, I is the applied current, and V is the feedback voltage.

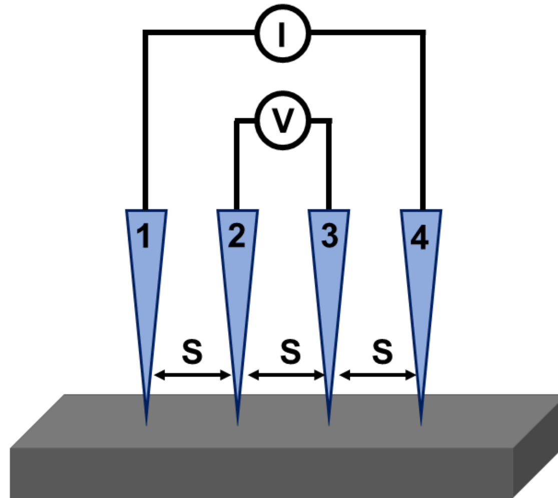

Figure 2.14. Schematic diagram of a linear four- probe.

For patterned MLG, the sheet resistance can be evaluated after deposition of metal electrodes on the top of the patterned graphene. Figure 2.15 shows a schematic diagram of a four-probe measurement for patterned MLG. A DC current is applied from outer electrodes and a different voltage is sensed by the inner electrodes. The sheet resistance can be calculated using the following equation [4],

$$R_s = \frac{V}{I}\frac{W}{L}, \tag{2.3}$$

where R_s is the sheet resistance, I is the applied current, V is the feedback voltage, W is the width of patterned MLG, and L is the length of the patterned MLG.

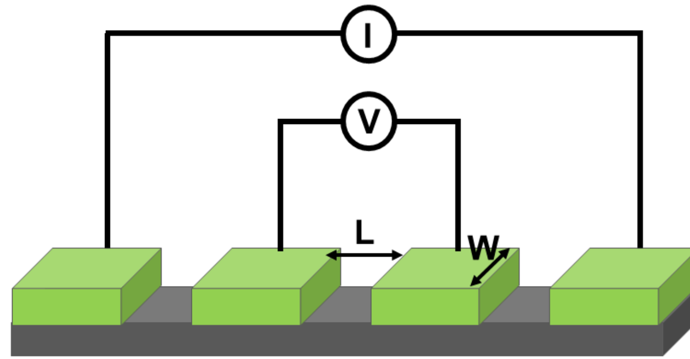

Figure 2.15. Schematic diagram of a four-probe measurement for patterned MLG.

A transmission line measurement or the transfer length measurement (TLM) is used to analyze the contact resistance between a metal electrode and doped MLG. Figure 2.16 shows a schematic diagram of a metal electrode for TLM measurement. The contact resistance and sheet resistance can be extracted by fitting the plot of the relationship between length and total resistance (R_T), as given by the equation [4]

$$R_T = R_S \frac{L}{W} + 2R_C, \tag{2.4}$$

where R_s is the sheet resistance, R_C is the contact resistance, W is the width of the patterned MLG, and L is the length between the two metal electrodes.

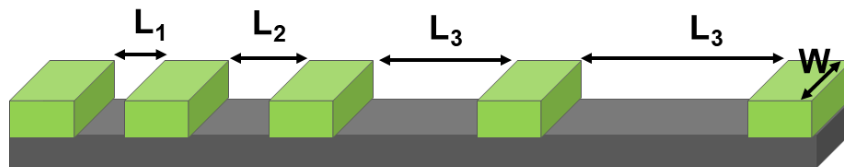

Figure 2.16. Schematic diagram of the electrode pattern for TLM measurements.

References

[1] K. Verguts, K. Schouteden, C. Wu, L. Peters, N. Vrancken, X. Wu, Z. Li, M. Erkens, C. Porret, C. Huyghebaert, C. V. Haesendonck, S. D. Gendt, and S. Brems, ACS Appl. Mater. Interfaces, **9.42**, 37484-37492 (2017).

[2] K. Verguts, J. Coroa, C. Huyghebaert, S. D. Gendt, and S. Brems, Nanoscale, **10**, 5515 (2018).

[3] S. Achraa, T. Akimoto, J. d. Marneffe, S. Sergeant, X. Wu, T. Nuytten, S. Brems, I. Asselberghs, Z.Tokei, K. Ueno, M. Heyns, Appl. Surf. Sci., **538**, 148046 (2021).

[4] X. Wu, Y. Chuang, A. Contino, B. Sorée, S. Brems, Z. Tokei, M. Heyns, C. Huyghebaert and I. Asselberghs, Adv. Mater. Interfaces. **5**, 1800454 (2018).

[5] L. Huang, Q.H. Chang, G.L. Guo, Y. Liu, Y.Q. Xie, T. Wang, B. Ling, H.F. Yang, Carbon **50**, 551-556 (2012).

[6] C. Mattevi, H. Kim and M. Chhowalla, J. Mater. Chem., **21**, 3324–3334 (2011).

[7] G. Odahara, S. Otani, C. Oshima, M. Suzuki, T. Yasue, T. Koshikawa, Surf. Sci, **605**, 1095–1098 (2011).

[8] 64 (1997).

[9] J. Mittal and M. Inggaki, Synth. Met., **95**, 23-28 (1998).

[10] A. Jorio, International Scholarly Research Notices 2012 (2012).

[11] C. C. Moura, R S. Tare, R.O. C. Oreffo, and S. Mahajan, J. R. Soc. Interface **13**, 20160182 (2016).

[12] U. P. Agarwal, R. H. Atalla, and J. S. Bond, Surface analysis of paper: 152-181 (1995).

[13] B. Alberto, H. Cheng, T. Enoki, Y. Gogotsi, R. H. Hurt, N. Koratkar, T. Kyotani, M. Monthioux, C. R. Park, J. M.D. Tascon, J. Zhang, Carbon, **65**, 1-6 (2013).

[14] L.M. Malard, M.A. Pimenta, G. Dresselhaus, M.S. Dresselhaus, Phys. Rep, 473, 51-**87** (2009).

[15] E. Lancelot, "Perspectives on Raman Spectroscopy of Graphene." HORIBA, Jun. 2013

[16] L. G. Cançado, K. Takai, T. Enoki, M. Endo, Y. A. Kim, H. Mizusaki, A. Jorio, L. N. Coelho, R. Magalhães-Paniago, and M. A. Pimenta, Appl. Phys. Lett., **88**, 163106 (2006).

[17] M. S. Uddin, “Fabrication of multilayer graphene by solid-phase reaction and application to gallium nitride based Schottky diodes”, Shibaura Institute of Technology (2017).

[18] A. Chauhan, “Deformation and damage mechanisms of ODS steels under high-temperature cyclic loading”, Karlsruher Institut für Technologie, (2018).

[19] Antonis Nanakoudis “EDX Analysis - SEM - EDS Analysis - Accelerating Microscopy.”https://www.thermofisher.com/blog/author/antonisnanakoudis/, 28 Nov. 2019.

[20] C. Zeng, C. Vitale-Sullivan, and X. Ma, Minerals, **7**, 158 (2017).

[21] T. J. Fellers and M. W. Davidson, “Confocal Microscopy – Introduction.” www.olympus-lifescience.com/ja/microscope-resource/primer/techniques/confocal /confocalintro/. Accessed 23 Feb. 2021.

[22] Kirti Prakash, bioRxiv, 121061 (2017).

[23] F. M. Smits, The Dell System Technical Journal, 711-718 (1985).

CHAPTER 3
INTERCALATION TO FEW LAYER GRAPHENE

3.1 Introduction

Based on the discussion in the Chapter 1, optimized FLG intercalated with $MoCl_5$ is a candidate low resistance material for narrow interconnects to replace Cu [1-8]. Improved electrical properties of bilayer graphene (BLG) and MLG by $MoCl_5$ intercalation were reported using a low concentration of $MoCl_5$ at a reaction temperature over 200°C and with a relatively long reaction time to minimize graphene damage at a high doping state [6]. In addition, $MoCl_5$ intercalation shows higher chemical stability than other metal chlorides [6-7, 9-12]. Moreover, FLG retains a high carrier mobility of ~1000 cm^2/Vs after scaling down to 20 nm [13]. Efficient doping without damage is still required for MLG.

In a previous study of our laboratory, higher intercalant vapor pressure was found to be more efficient for higher doping concentration in MLG flakes exfoliated from HOPG at 300°C [5, 12]. Our approach for the optimization of $MoCl_5$ intercalation in FLG uses high chemical concentration to reduce intercalation temperature and time and investigates the doping efficiency and damage of graphene.

In this chapter, we investigate the optimum chemical concentration, intercalation temperature, and reaction time on the layer number of CVD graphene up to tri-layer graphene (TLG), in terms of doping efficiency, crystallinity, and damage. This chapter also discusses the potential mechanism for layer number dependence of intercalation.

3.2 Experimental methods

Single-layer graphene (SLG) including FLG areas was grown by CVD on Pt film and subsequently transferred to a SiO_2/Si substrate. The sample was inserted into a glass capsule with a high ($MoCl_5$ at 0.3412 g and MoO_3 at 0.0665 g) or reduced ($MoCl_5$ at 0.1706 g and MoO_3 at 0.0333 g) concentration of chemicals. After enclosing the glass capsule, it was inserted into a glass tube. Ar gas was flowed through the glass tube for 10 min. Before the

reaction, the glass tube was pre-annealed at 110°C for 120 min to dry out water. The reaction temperature was varied between 150°C and 250°C for the temperature dependence experiment. For the reaction time dependence experiment, the reaction time was varied between 30 min and 120 min. The pre-annealing and reaction temperatures were controlled during the experiment. The heating rate was 10°C/min, and the natural cooling was done in the atmosphere used in this experiment.

The doping efficiency and crystallinity of graphene were analyzed using a HORIBA HR-Evolution Raman spectroscope with 532-nm laser excitation. The RMS roughness and surface morphology were characterized using a Hitachi AFM5000II AFM with a scanning area of $5 \times 5\ \mu m^2$. The morphology and layer number were determined by optical microscope observations.

3.3 Results and discussion

After transferring the FLG to the SiO_2/Si substrate, the morphology and layer number were determined by optical microscope observations. Figure 3.1 shows the morphology from the optical microscope and Raman spectra of the FLG. SLG, BLG, and TLG areas can be distinguished in the optical image. The Raman spectra shows the intensity ratio between the G- and 2D-bands depends on the layer number of the FLG. This chapter is separated into two parts. The first part discusses the high chemical concentration used from previous optimization for Stage 1 intercalation in flakes exfoliated from HOPG. The second part discusses the use of reduced chemical concentration to reduce damage in the FLG.

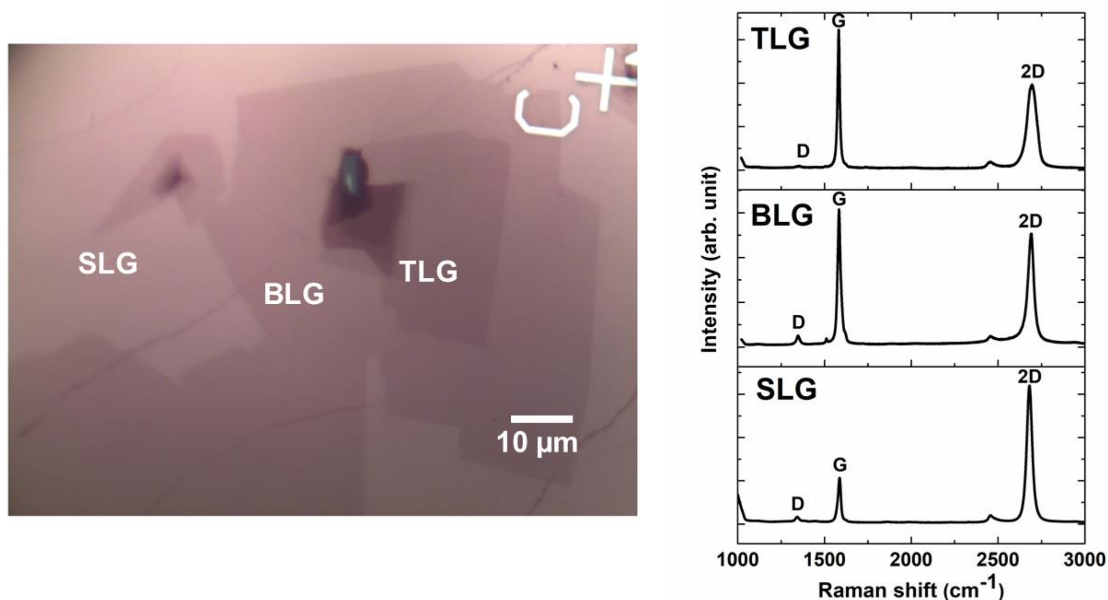

Figure 3.1. Optical microscopy morphology (left) and Raman spectra (right) of FLG.

3.3.1 High chemical concentration intercalant process

In our previous study, higher vapor pressure of intercalant was found to be more efficient for higher doping concentration in MLG flakes exfoliated from HOPG at 300°C [5, 12]. Here, we optimized the intercalation process using a high concentration of intercalant in FLG (specifically SLG and BLG). Figure 3.2 shows Raman spectra of BLG and SLG areas in samples after reaction at different reaction temperatures (between 250°C and 130°C). According to the position of the G peak, we can determine the doping state as surface doping, G peak at 1600 cm^{-1}, and intercalation doping between graphene layers, G peak at 1612 cm^{-1} [6, 12].

At 250°C, the BLG area was clearly intercalated as the G peak is located at 1612 cm^{-1} in Figure 3.2. At 150°C, the BLG area was intercalated according to the G peak position, but the peak intensity was reduced. Surface doping was also observed at 150°C, as indicated by the small peak observed at 1600 cm^{-1}. Further reduction to 130°C resulted in no intercalation in the BLG area and the observation of only surface doping. From these results, we can conclude that the process temperature can be lowered to 150°C for intercalating BLG areas. On the other hand, surface doping was observed down to 130°C.

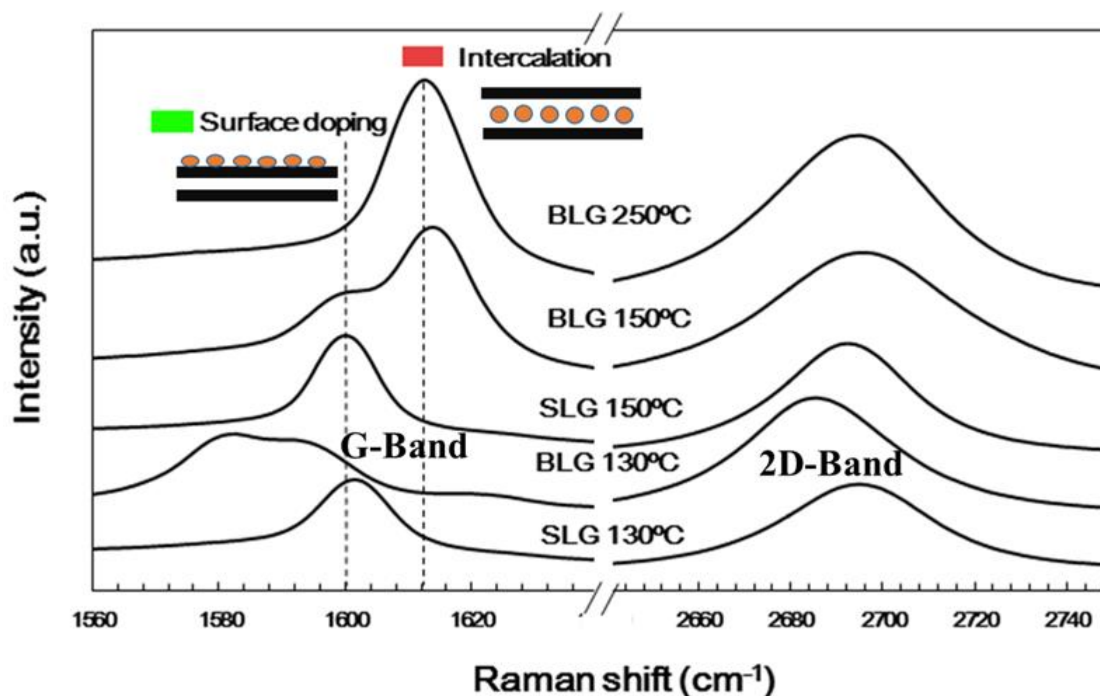

Figure 3.2. Raman spectra of BLG and SLG after intercalation with a high concentration of $MoCl_5$ for 60 min at different temperatures.

Figure 3.3 shows Raman mapping of the G peak position at 150 °C for 30 and 60 min with high chemical concentration and 30 min with reduced chemical concentration. The SLG areas and BLG areas can be distinguished in the optical image. By looking at the G peak position of graphene doped at high chemical concentration, we conclude that the BLG is intercalated while the SLG is surface doped. It is also noted that a reaction time of 60 min shows more uniform doping than that of 30 min. With reduced chemical concentration, the BLG area is not intercalated in 30 min and longer time reaction time is required.

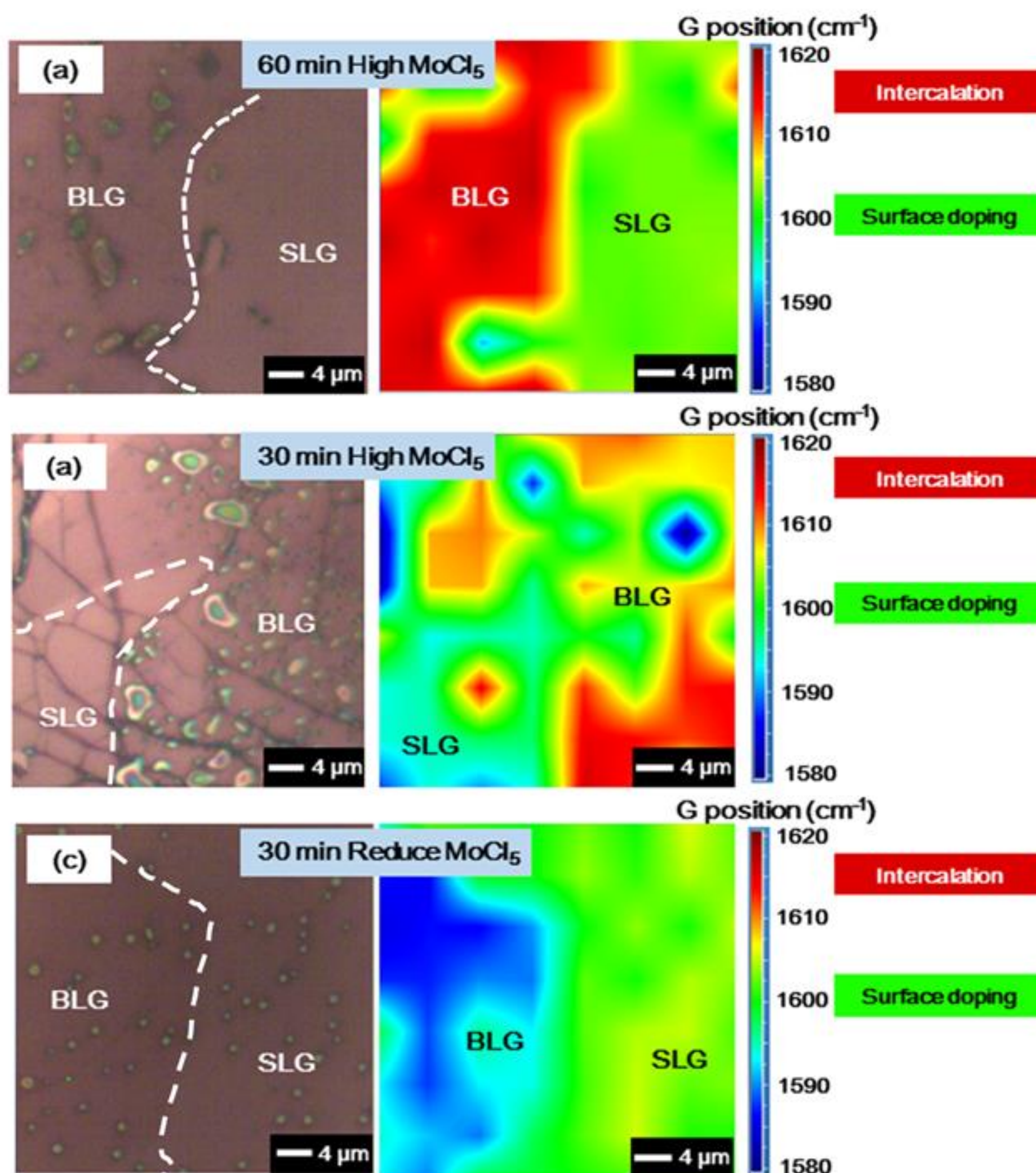

Figure 3.3. Optical image and Raman mapping of the G peak position in SLG and BLG areas. High concentration at 150°C (a) for 60 min and (b) 30 min and (c) reduced concentration for 30 min.

Figure 3.4 shows optical surface images of CVD graphene on a SiO_2/Si substrate before and after reaction with high concentration $MoCl_5$ for 60 min at 250°C, 150°C, and 130°C. At 250°C, all of the SLG area was damaged during the reaction, but some BLG areas

remained, as shown in Figure 3.4(a). At 150°C, damage on the BLG areas were drastically reduced though the SLG areas still had some damage. The morphology after reaction at 130°C shows similar morphology to that before the reaction. From these results, the damage can be reduced by reducing the reaction temperature and non-damaged BLG areas intercalated with $MoCl_5$ can be obtained at 150°C for 60 min.

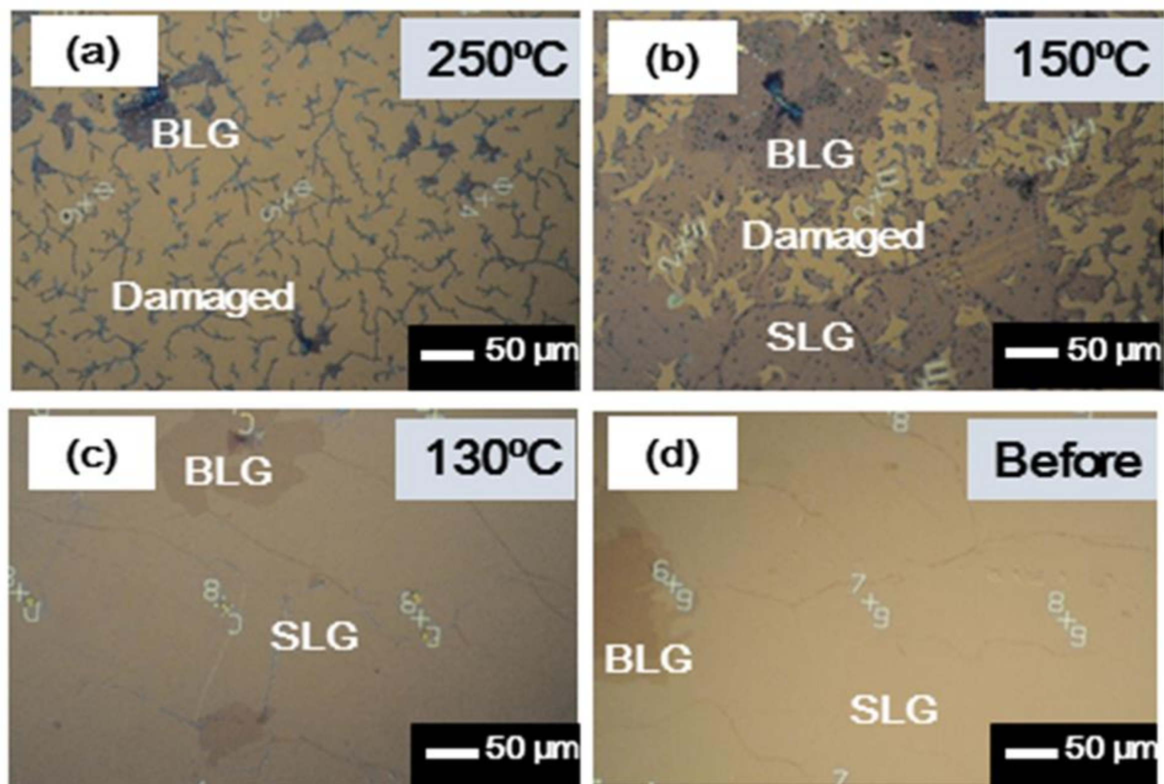

Figure 3.4. Optical microscope images of surface morphology after reaction with high concentration $MoCl_5$ for 60 min at different reaction temperatures: (a) 250°C, (b) 150°C, and (c) 130°C. (d) Pristine graphene on SiO_2.

Figure 3.5 shows the morphology of SLG and BLG after intercalation at different reaction times with high concentration $MoCl_5$ at 150°C. From AFM analysis, the RMS roughness increased, from 4.9 nm to 9.5 nm, after increasing the reaction time from 30 min to

60 min. Damage increased with increasing reaction time after intercalation with high chemical concentration.

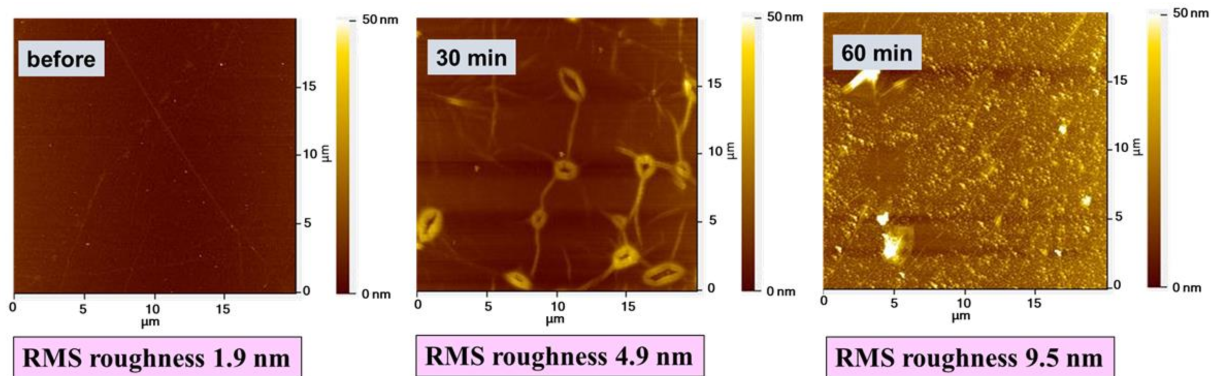

Figure 3.5. AFM results of BLG after reaction with high concentration $MoCl_5$ at 150°C.

From the above results, the intercalation temperature can be reduced to 150°C to reduce process damage while using high chemical concentrations. The doping uniformity was improved by increasing the process time. Reduced resistance of MLG interconnects is expected with the use of the proposed process However, nano-patterned interconnects were damaged from this intercalation process. To reduce damage, we have reduced the chemical concentration for low temperature $MoCl_5$ intercalation and analyzed doping efficiency and damage on the BLG area.

Figure 3.6 shows the G-band Raman spectra in the BLG area after 60 min of the intercalation process. At 150°C, BLG was intercalated using high concentration chemicals but was not intercalated using the half of the high chemical concentration. With reduced concentration, BLG was intercalated by raising the temperature to 175°C.

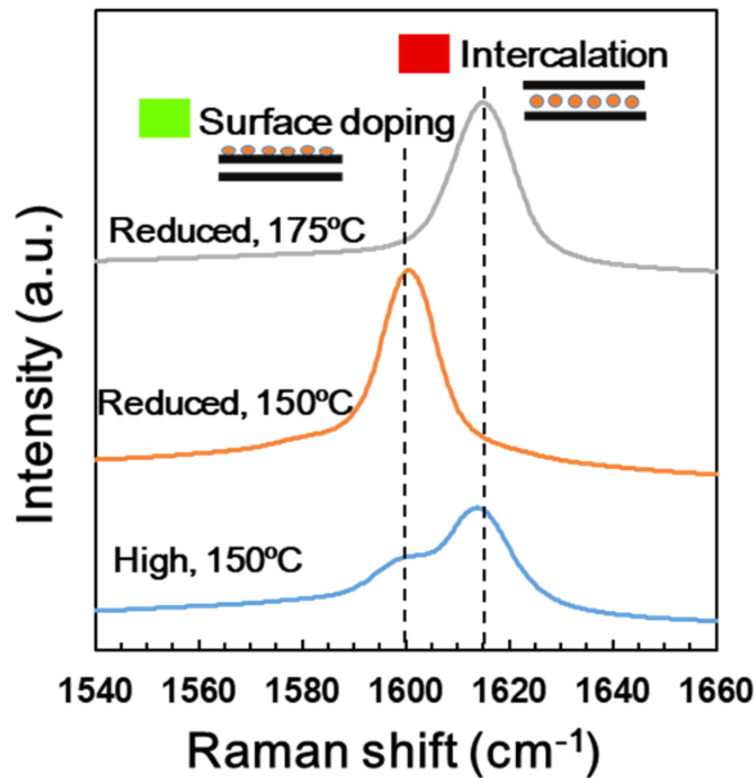

Figure 3.6. G-band of BLG after intercalation using high chemical concentration at 150°C and 175°C and with reduced chemical concentration at 175°C.

Figure 3.7 shows optical images of BLG after intercalation for 60 min. Although serious damage was observed with high chemical concentration, damage was suppressed with reduced chemicals at both 150 and 175°C. From these results, reduced chemical concentration is considered more appropriate for doping narrow graphene interconnects.

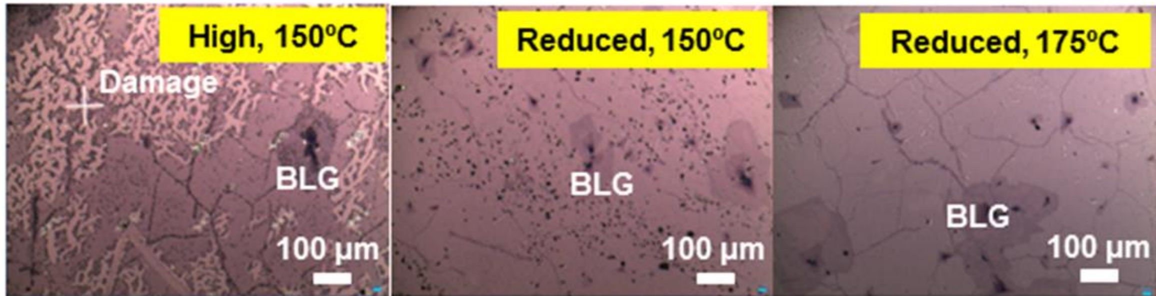

Figure 3.7. Optical images after intercalation for 60 min.

3.3.2 Reduced chemical concentration intercalation

From the results of high chemical concentration intercalation in the previous section, reduced chemical concentration intercalation was considered more appropriate for doping narrow graphene interconnects. In this section, reduced chemical concentration intercalation was investigated in terms of doping efficiency and damage.

3.3.2.1 Doping efficiency characterization by Raman spectroscopy

3.3.2.1.1 Reaction temperature dependence of doping efficiency

Figure 3.8 shows the G-band spectra of BLG and TLG after intercalation at different temperatures. The G-band spectra tend to shift to larger wave numbers or blue shift the G-band with increasing reaction temperature. At the low reaction temperature of 150°C, the G-band of both BLG and TLG is located around 1600 cm^{-1}, which corresponds to surface doping [6, 12]. The peak position of TLG was shifted to lower values than that of BLG, below 1600 cm^{-1}, since the reported peak position of the TLG G-band has a component without surface doping. With a reaction temperature of 175°C, the BLG G-band of BLG shifted to 1615 cm^{-1}, which corresponds to intercalation doping of BLG. On the other hand, the TLG G-band shifted to a relatively lower wave number than the BLG of 1607 cm^{-1}. The G-band of TLG can be fitted with three components corresponding to non-doping, surface doping, and intercalation doping [12]. The mix of G-band components leads to shift of the band to lower values for TLG due to the surface doping component. With a reaction temperature of 200°C, the G-bands of both BLG and TLG were shifted to a wave number of

around 1620 cm^{-1}. The G-band of TLG consists of components at 1605 cm^{-1} and 1620 cm^{-1}, which correspond to surface doping and intercalation doping of TLG, respectively.

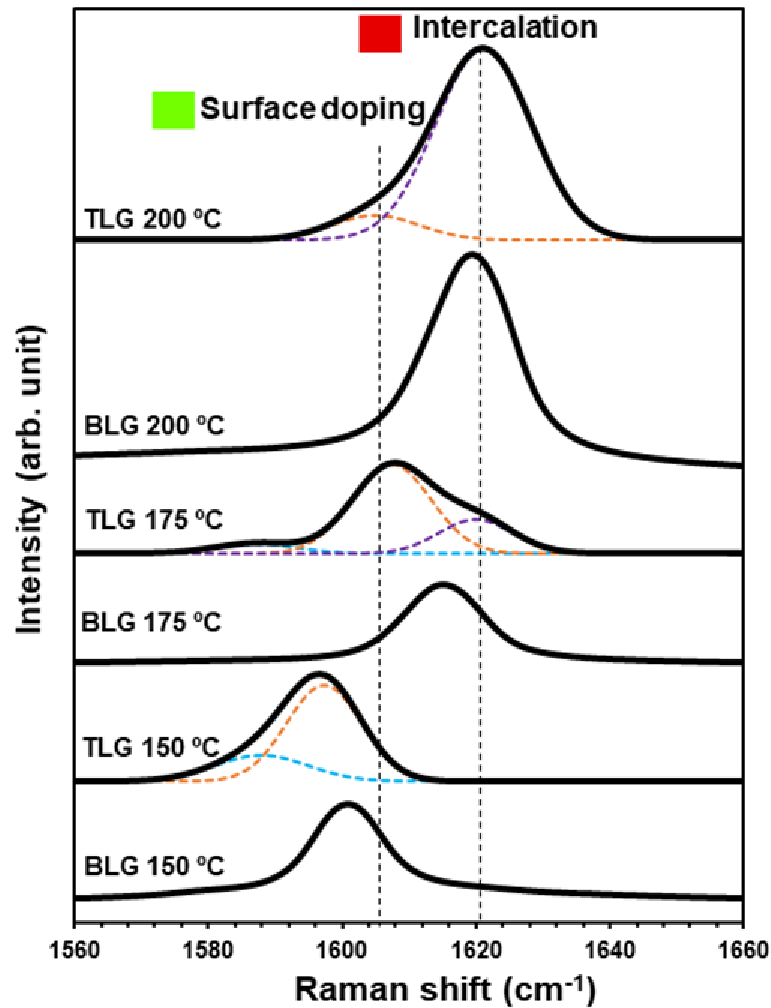

Figure 3.8. G-band spectra of BLG and TLG after intercalation for 60 min.

According to the position of the G-band, we can determine the doping level of surface doping, at 1600 cm^{-1}, and intercalation doping between graphene layers, at wavenumbers greater than 1615 cm^{-1}. From the Raman spectra, the G peak positions were averaged from five positions in each layer number of graphene. Figure 3.9 shows the relationship between the average G peak position and the reaction temperature after intercalation for 60 min. At a low temperature of 150°C, only surface doping was observed for all graphene layer numbers.

At a temperature of 175°C, only BLG was intercalated and SLG and TLG were observed at the surface doping level. Although TLG was not intercalated at 175°C, both BLG and TLG were successfully intercalated at a high temperature of 200°C. These results indicate that the increase of reaction temperature, from 150°C to 200°C, leads to enhancement of doping efficiency, which corresponds to a blue shift in the G-band of the Raman spectra. Moreover, TLG requires a higher temperature to introduce $MoCl_5$ into the interlayers, compared to BLG.

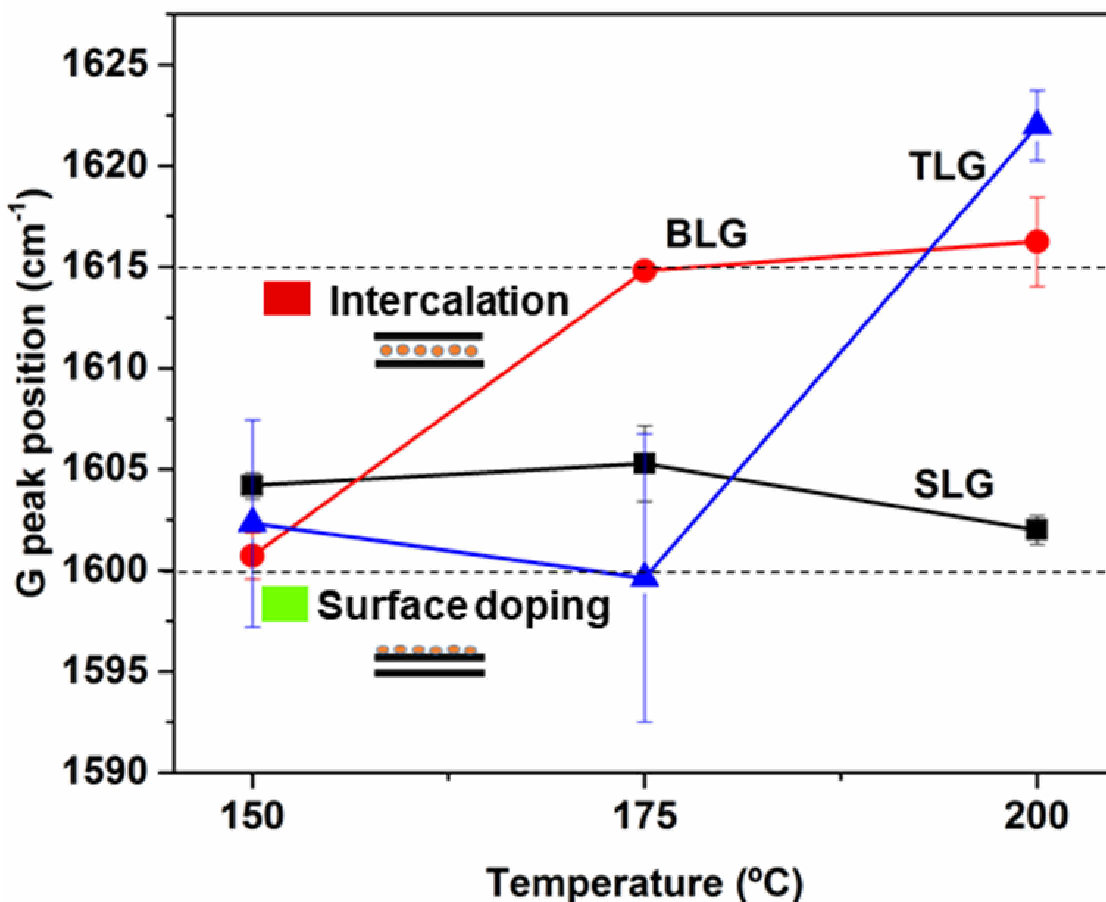

Figure 3.9. Relationship between the average G peak position and reaction temperature after intercalation for 60 min.

Figure 3.10 shows Raman mapping of the G peak position on FLG after intercalation at different reaction temperatures. At 150°C, only the BLG area was intercalated and non-uniform intercalation of the BLG area was observed (red color area in the figure). Surface-

level doping was observed in the TLG area at 150°C. At 175°C, more uniform intercalated area was observed in the BLG, as shown in Fig. 3. This indicates that increasing the reaction temperature from 150°C to 175°C can enhance the uniformity of the intercalation area in BLG. With an increase in reaction temperature to 200°C, higher peak intensity was observed in the BLG area, which extended into the TLG area. This result indicates that the doping density and uniformity of the intercalation area were improved by increasing the reaction temperature.

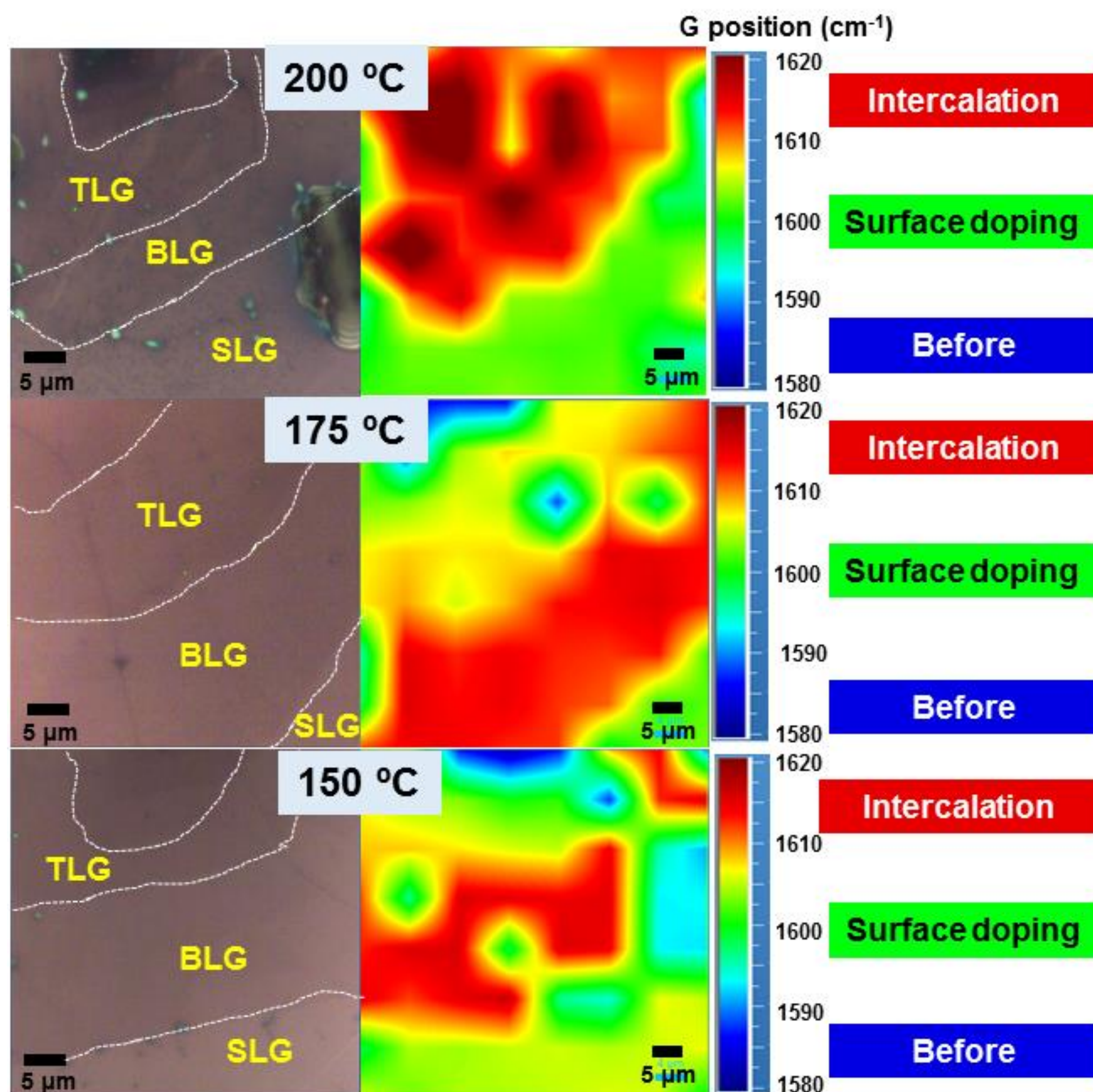

Figure 3.10. Raman mapping of the G peak position of FLG after intercalation for 60 min.

3.3.2.1.2 Reaction time dependence of doping efficiency

From Figure 3.8 and Figure 3.9, the lowest temperatures that can be used to intercalate $MoCl_5$ into BLG and TLG are 175°C and 200°C, respectively. Focusing on the reaction temperature of 175°C, intercalation doping on BLG can be achieved and the G-band of TLG blue shifts more than that for the reaction temperature of 150°C. From this result, TLG is expected to intercalate by extending the reaction time to more than 60 min at a fixed reaction temperature of 175°C.

Figure 3.11 shows the G-band spectra of the TLG after intercalation at 175°C for different reaction times. The G-band spectra of reaction times of 60 min and 90 min are located between the wave numbers 1600 cm^{-1} and 1615 cm^{-1}. However, the G-band of TLG shifted to a value higher than 1615 cm^{-1} after extending the reaction time to 120 min. After G-band deconvolution, a mix of three components (1590 cm^{-1}, 1605 cm^{-1}, and 1620 cm^{-1}) was found. The 1590 cm^{-1} peak disappeared after extending the reaction time to 120 min, showing peaks only at 1609 cm^{-1} and 1620 cm^{-1}. The ratio of peak intensity between 1609 cm^{-1} and 1620 cm^{-1} was 1:2, which corresponds to Stage 2 intercalation [14]. From this result, it appears that $MoCl_5$ was intercalated on only one side of the intermediate graphene layer and surface doping remains after extending the reaction time to 120 min.

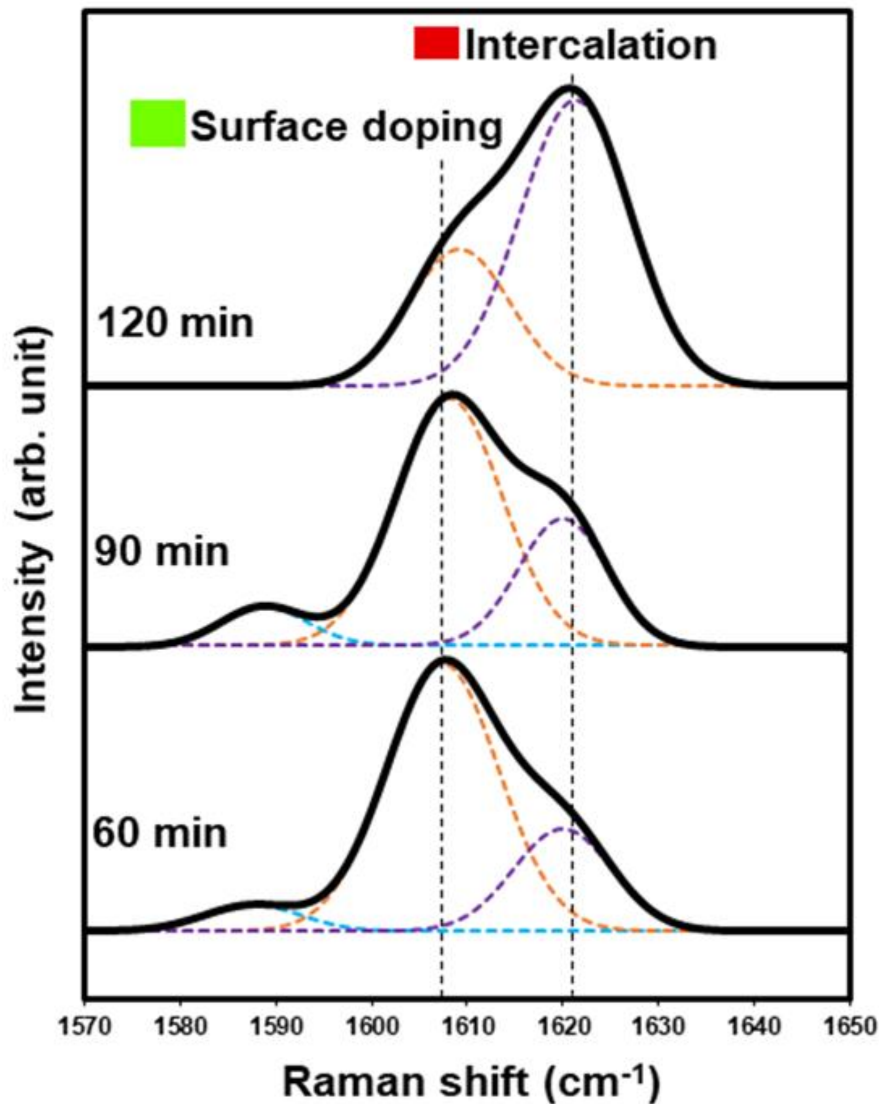

Figure 3.11. G-band spectra of TLG after intercalation at 175°C.

Figure 3.12 shows the relationship between the average G peak position of the TLG and the reaction time. The average G peak position tends to increase as the reaction time increases from 60 min to 120 min. This indicates that TLG was successfully intercalated after extending the reaction time to 120 min. Therefore, the longer reaction time in the intercalation process is an alternative approach for intercalating more layers of graphene, such as TLG, instead of increasing the temperature. For process optimization, it is important to consider not only the doping efficiency but also the damage from the intercalation process for nano-interconnect applications.

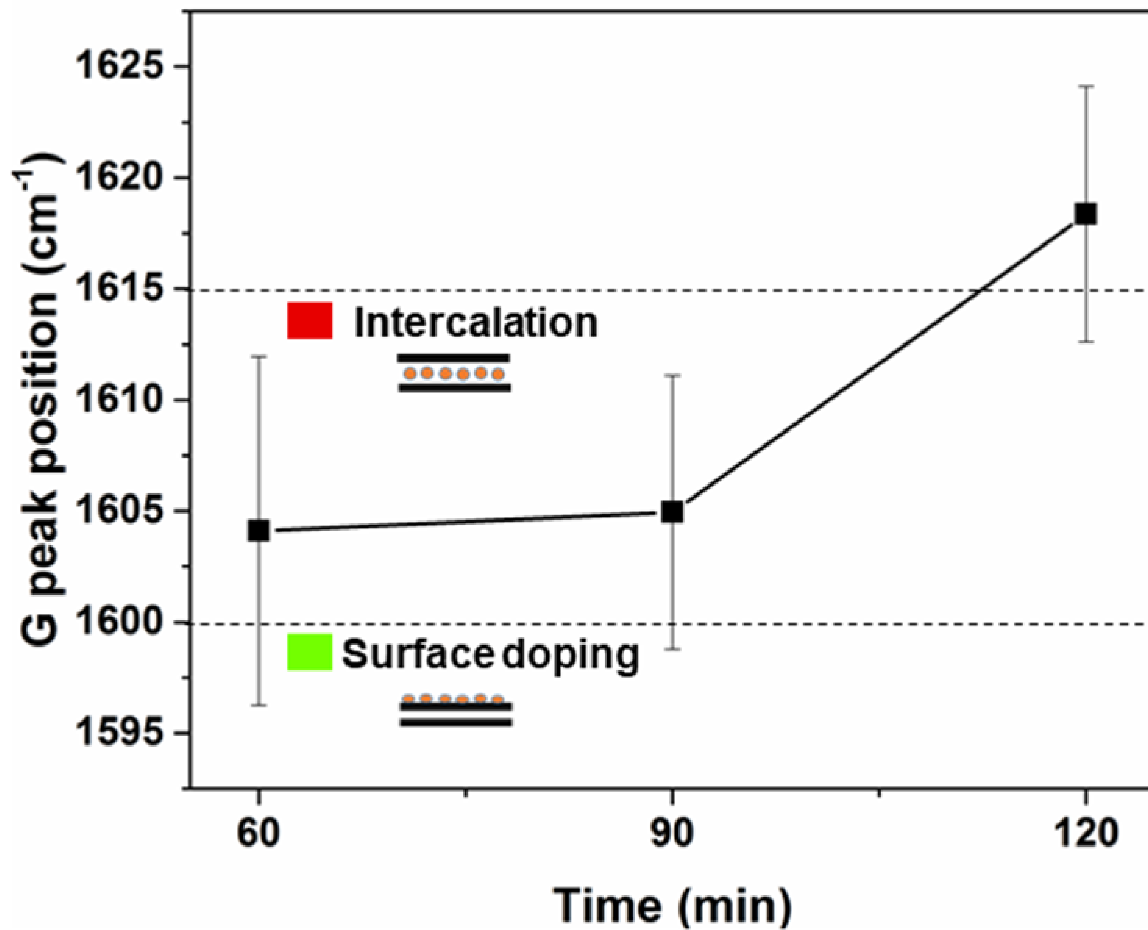

Figure 3.12. Relationship between average G peak position of TLG and reaction time after intercalation at 175°C.

3.3.2.2 Damage in FLG from the intercalation process

3.3.2.2.1 Reaction temperature dependence of FLG damage

Figure 3.13 shows optical images after the intercalation process for 60 min at different reaction temperatures. The sample consists of an entire area of SLG and includes small islands of FLG areas. The damage to the SLG was enhanced with increasing reaction temperature. With low reaction temperatures of 150°C and 175°C, no serious damage was observed. However, with a higher temperature of 200°C, serious damage was observed on the SLG area.

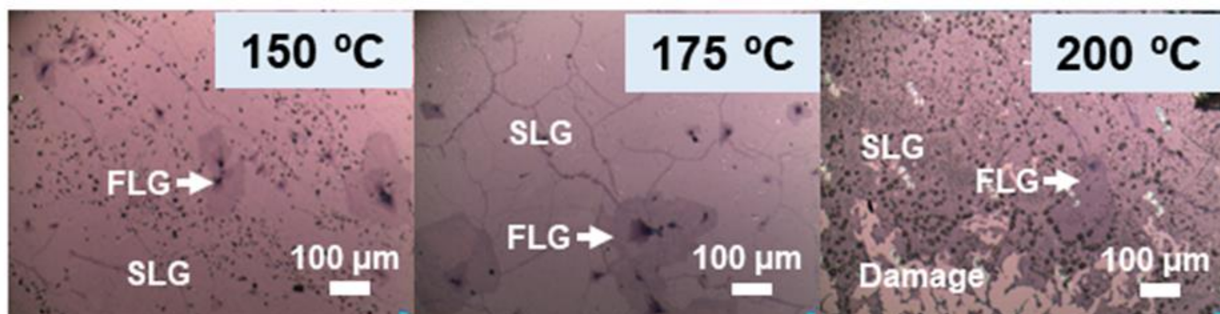

Figure 3.13. Optical images after 60 min of the intercalation process at different reaction temperatures.

Figure 3.14 shows the surface morphology via AFM of the BLG area after intercalation at different reaction temperatures. There was minimal morphology difference between the reaction temperature of 150°C and 175°C, which is consistent with the optical images in Figure 3.13. Only a small dot on the BLG surface was observed for reaction temperatures of 150 and 175°C. However, larger hillocks were observed at a higher reaction temperature of 200°C.

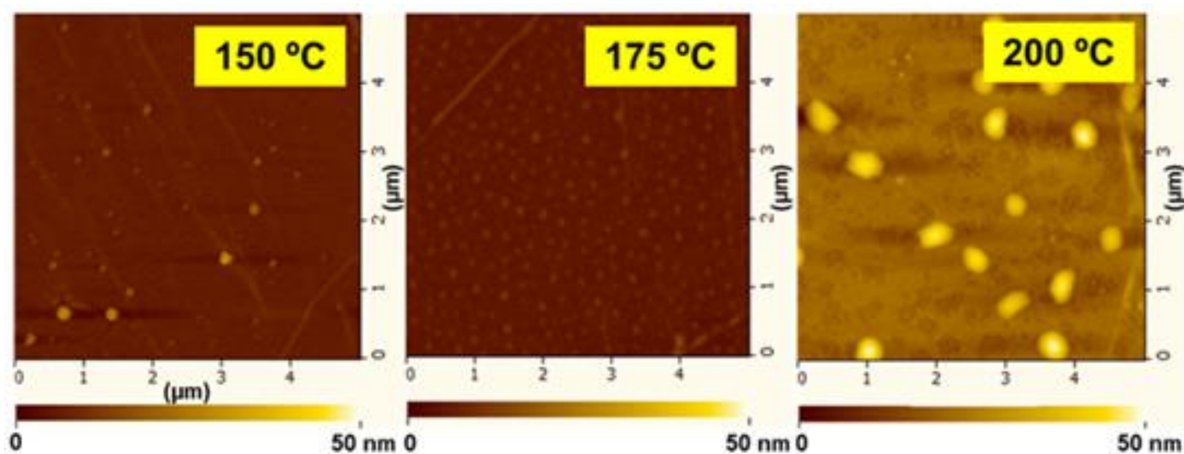

Figure 3.14. AFM morphology of BLG after the intercalation process for 60 min at different temperatures.

Figure 3.15 shows the relationship between RMS roughness from AFM and reaction temperature. The RMS roughness of the reaction temperature of 200°C is larger than those of the lower reaction temperatures. The RMS roughness was significantly increased at 200°C due to damage in the SLG and BLG areas.

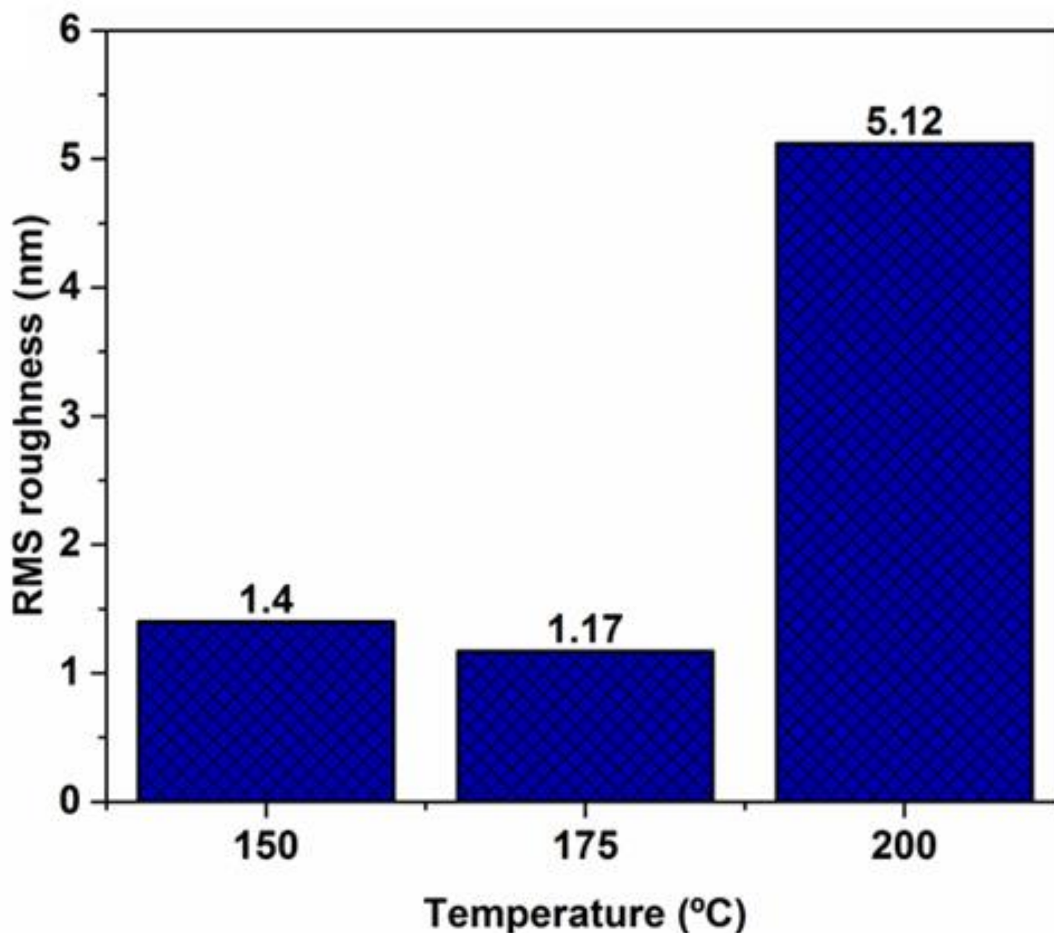

Figure 3.15. AFM RMS roughness for different reaction temperatures of 150, 175, and 200°C.

Table 3.1 shows the G/D ratios of different FLGs, which indicate the crystallinity and crystallite size of graphene before the intercalation process [15-17]. The intercalation process consists of a pre-annealing process at 110°C for 120 min and the reaction process at different temperatures and times. During the process, the crystallinity of FLG was improved by the pre-annealing process and damaged by the $MoCl_5$ reaction.

Table 3.1. G/D ratios of FLGs before the intercalation process.

Layer number	G/D ratio	
	Average	SD
SLG	6.17	0.96
BLG	15.10	3.93
TLG	15.29	7.09

Figure 3.16 shows the relationship between the G/D ratios and the reaction temperature for the SLG, BLG, and TLG areas. For SLG and BLG, the G/D ratio after intercalation tends to decrease as the reaction temperature increases. However, for TLG after reaction at 200°C, the G/D ratio was higher than that of BLG after reaction at 175°C and 200°C. Moreover, the G/D ratios of BLG and TLG were higher than that of SLG at all reaction temperatures. This indicates that both BLG and TLG have greater resistance to damage from the intercalation process compared to SLG.

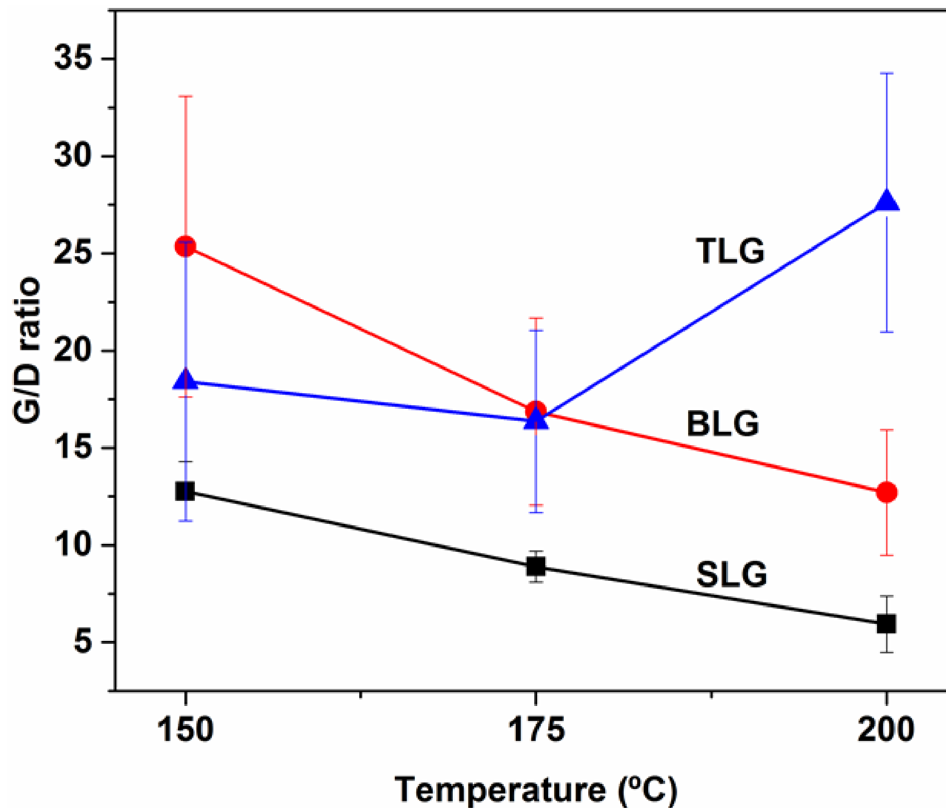

Figure 3.16. Relationship between G/D ratios and reaction temperature after the intercalation process for 60 min.

From the temperature dependence of damage, the increase of reaction temperature leads to increase in damage in FLG. In addition, TLG is more resistant against damage at a higher temperature compared to BLG.

3.3.2.2.2 Reaction time dependence of FLG damage

Figure 3.17 shows optical images after the intercalation process at different reaction times. The sample consists of an entire SLG area that includes small islands of FLG areas. Only after a long reaction time of 120 min was damage on the SLG area observed. In the case of a shorter reaction time, no serious damage was observed on FLG.

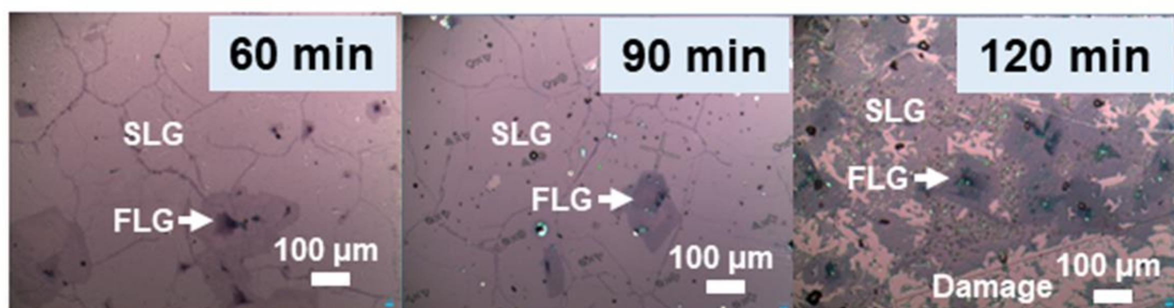

Figure 3.17. Optical images after the intercalation process at 175°C for various reaction times.

Figure 3.18 shows the surface morphology from AFM of the BLG area after intercalation at different reaction times. Rougher surface morphology was observed after extending the reaction time from 60 min to 120 min. The size of dots on the BLG surface appears to have increased after extending the reaction time.

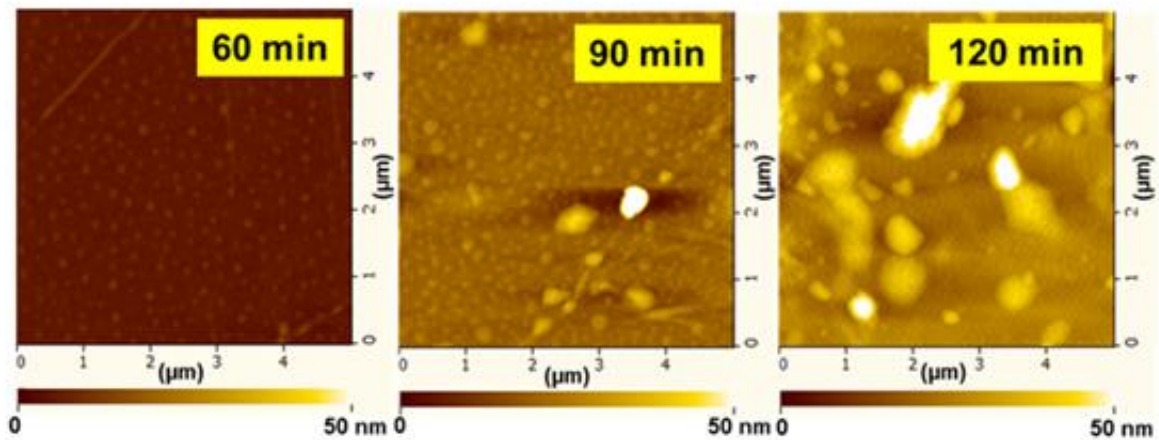

Figure 3.18. Morphology from AFM after the intercalation process at 175°C for different reaction times.

Figure 3.19 shows the AFM RMS roughness dependence of the BLG area on the reaction time. The RMS roughness tends to increase with increasing reaction time. Comparing the roughness at 120 min with that in Figure 3.15, this RMS roughness was highest among all conditions.

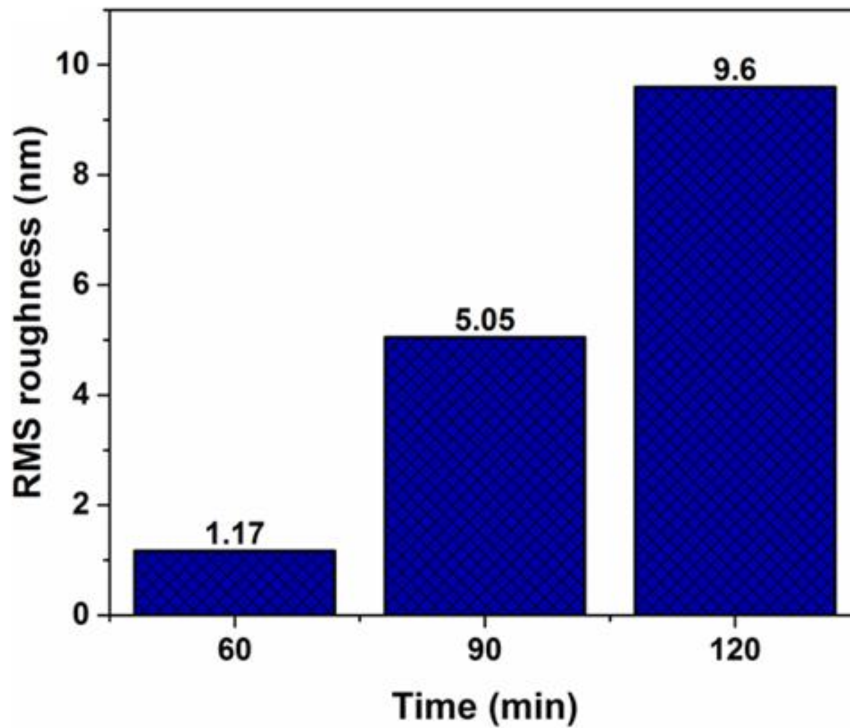

Figure 3.19. RMS roughness for different reaction times of 60, 90, and 120 min.

Figure 3.20 shows the relationship between the G/D ratios and the reaction time. The G/D ratio for the BLG and TLG decreased with increasing reaction time. The G/D ratio of SLG does not depend on the reaction time. The longer chemical reaction during the $MoCl_5$ intercalation process may degrade the crystallinity of graphene due to the generation of highly corrosive Cl_2 gas from the $MoCl_5$ intercalation reaction [9,18]. However, the G/D ratios of the TLG and BLG are higher than that of SLG, even after extended reaction time. This indicates that TLG and BLG are more resistant to process damage than SLG.

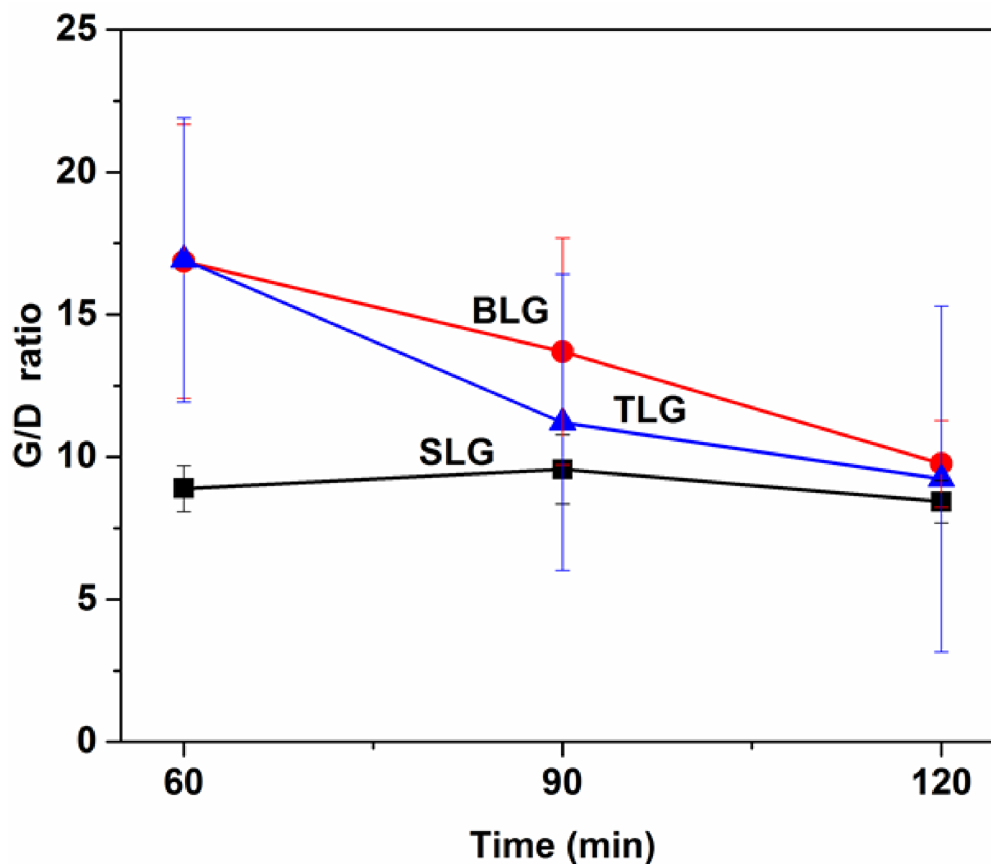

Figure 3.20. Relationship between G/D ratios and reaction time at 175°C.

To optimize the $MoCl_5$ intercalation process for more effective doping and lower damage for TLG, the temperature and time conditions of 200°C and 60 min appear better than that of 175°C and 60 min because of the larger G peak shift and higher G/D ratio of the former. Considering the damage in the FLG areas, as shown in Figures 3.13–3.20, the longer

reaction time leads to reduction of the G/D ratio, which indicates degradation of TLG crystallinity. In addition, the highest RMS roughness and larger damage area observed by AFM were found for the longer reaction time of 120 min. Using the optimized condition, the electrical charactarization was carried out at imec. The carrier concentration reached ~3.8×10^{13} cm^{-2} after intercalation using a high chemical concentration. Resistivities of 14 μΩ cm and 40 μΩ cm were reached for a micron-sized graphene device and graphene nanoribbons, respectively [20].

Figure 3.21 shows a schematic model explaining the temperature and time dependence of $MoCl_5$ intercalation into FLG depending on the number of graphene layer. The stacked upper layers may effect damage protection from the chemical reaction of $MoCl_5$ [19]. At the same time, stacked layers should avoid the penetration of intercalant molecules, which leads to an increase in activation energy for intercalation [6, 13]. Therefore, a higher reaction temperature or longer reaction time are required to intercalate $MoCl_5$ into an increasing number of layers.

The doping efficiency results shows that the doping stage was started from the surface doping stage. The vapor pressure and the reaction rate depend on the chemical amount and the temperature of the intercalation process. After the energy higher than the activation energy of intercalation doping through the increase of the intercalation parameters (chemical amount, temperature and time), the $MoCl_5$ molecules can be penetrated into the interlayers of few-layer graphene, the intercalation doping will be performed.

The compressive strain (in-plane direction) of the few-layer graphene was induced during the doping process [21]. The high reaction rate of $MoCl_5$ intercalation doping induces non-uniform doping areas on few-layer graphene in short time. The non-uniformity of doping areas leads to the non-uniformity of strain in few-layer graphene. The non-uniformity of high strain in the intercalation doping process is considered to be the cause of damage on the few-layer graphene.

The structure of $MoCl_5$ intercalated graphene is reported in Ref. 12, which shows a cross-sectional TEM image of $MoCl_5$-intercalated MLG and the atomic structure of Stage 2 $MoCl_5$ GIC. The structure and packing of $MoCl_5$ intercalated into FLG will be a topic of future study.

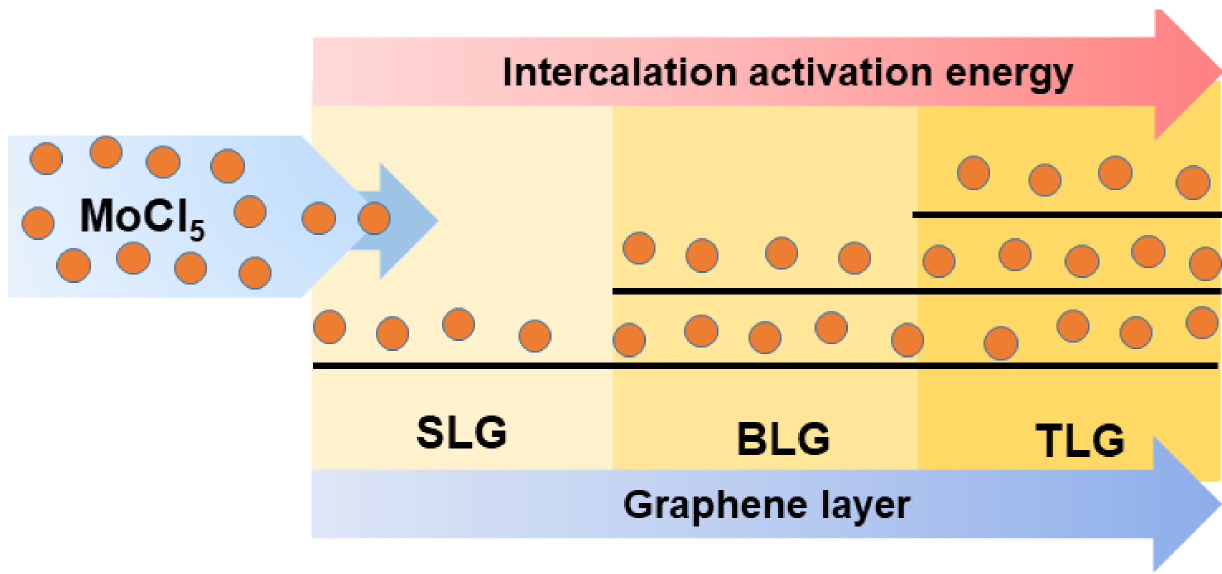

Figure 3.21. Schematic model explaining the graphene layer number dependence of $MoCl_5$ intercalation into FLG.

3.4 Summary and conclusions

For high chemical concentrations, the intercalation temperature can be reduced to 150°C to reduce the damage of FLG. The doping uniformity was improved by increasing the reaction time.

For intercalation with reduced chemical concentrations, the temperature and time dependencies of $MoCl_5$ intercalation in FLG were investigated to optimize process conditions from the viewpoint of doping efficiency and process damage. It was found that intercalation efficiency and damage of FLG depend on the number of graphene layers. The optimum temperature and time increase as the layer number increases. Either a higher temperature or a longer time leads to increased doping efficiency and damage. By comparing the G peak shift and the G/D ratio, better conditions for TLG intercalation were determined to be 200°C for 60 min rather than 175°C for 120 min. It is suggested that optimization of the intercalation temperature and time is important and depends on the layer number implemented for device applications of FLG. With the optimized condition, the carrier concentration reached ~3.8×10^{13} cm^{-2} after intercalation using a high chemical concentration. Resistivities of 14 μΩ cm and 40 μΩ cm were reached for a micron-sized graphene device and graphene nanoribbons, respectively [20].

References

[1] J. Jiang, J. Kang, W. Cao, X. Xie, H. Zhang, J.H. Chu, W. Liu and K. Banerjee, Nano Lett. **17**, 1482 (2017).

[2] J. Jiang, J. Kang, J.H. Chu and K. Banerjee, Proc. IEEE Int. Electron Devices Meeting, 2017, p. 14.3.1.

[3] S. Dutta, S. Kundu, A. Gupta, G. Jamieson, J.F.G. Granados, J. Bömmels, C.J. Wilson, Z. Tőkei and C. Adelmann, IEEE Electron Device Lett. **38**, 949 (2017).

[4] X. Wu, I. Asselberghs, C. Huyghebaert, A. Contino, B. Soree, M. Heyns and Z. Tokei, Proc. IEEE Int. Interconnect Technology Conf., 2018, p. 25.

[5] K. Kawamoto, Y. Saito, M. Kenmoku and K. Ueno, Proc. IEEE Electron Devices Technology and Manufacturing Conf., 2017, p. 252.

[6] H. Kinoshita, I. Jeon, M. Maruyama, K. Kawahara, Y. Terao, D. Ding, R. Matsumoto, Y. Matsuo, S. Okada and H. Ago, Adv Mater. **29**, 1702141 (2017).

[7] R. Matsumoto and Y. Okabe, Synth. Met. **212**, 62 (2016).

[8] X. Wu, I. Asselberghs, M. Politou, A. Contino, I. Radu, C. Huyghebaert, Z. Tokei, B. Soree, S. De Gendt, S. De Feyter and M. Heyns, Microelectron. Eng. **167**, 42 (2017).

[9] K. Yokosawa, T. Akimoto, Y. Okada and K. Ueno, Proc. Electron Devices Technology and Manufacturing Conf., 2019, p. 47.

[10] J. Mittal and M. Inagaki, Synth. Met. **92**, 87 (1998).

[11] J. Mittal and M. Inagaki, Synth. Met. **99** 79 (1999).

[12] H. Miyazaki, R. Matsumoto, M. Katagiri, T. Yoshida, K. Ueno, T. Sakai and A. Kajita, Jpn. J. Appl. Phys. **56**, 04CP02 (2017).

[13] X. Wu, Y. Chuang, A. Contino, B. Sorée, S. Brems, Z. Tokei, M. Heyns, C. Huyghebaert and I. Asselberghs, Adv. Mater. Interfaces. **5**, 1800454 (2018).

[14] D. Zhan, L. Sun, Z. H. Ni, L. Liu, X. F. Fan, Y. Wang, T. Yu, Y. M. Lam, W. Huang, and Z. X. Shen, Adv. Funct. Mater. **20**, 3504 (2010).

[15] T. Akimoto and K. Ueno, Proc. Electron Devices Technology and Manufacturing Conf., 2019, p. 351.

[16] L. G. Cançado, K. Takai, T. Enoki, M. Endo, Y. Kim, H. Mizusaki, A. Jorio, L.

Coelho, R. Magalhaes-Paniago and M. Pimenta, Appl. Phys. Lett. **88**, 163106 (2006).

[17] M.S. Uddin and K. Ueno, Jpn. J. Appl. Phys. **56**, 04CP08 (2017).

[18] M. Kosaka, S. Takano, K. Hasegawa and S. Noda, Carbon. **82**, 254 (2015).

[19] Q. Chen, L. Zhang and H. Zhu, Nano Res. **11**, 440 (2018).

[20] X. Wu, I. Asselberghs, E. Ketsombun, K. Yokosawa, S. Achra, S. Brems, C. Huyghebaert, M. Heyns, B. Sorée, K. Ueno and Z. Tokei, Proc. IEEE Int. Interconnect Technology Conf. / Materials for Advanced Metallization Conf., 2019, p. 4.21.

[21] J. E. Lee, G. Ahn, J. Shim, Y. S. Lee, S. Ryu, Nat. Commun. **3**, pp. 1-8 (2012).

CHAPTER 4
INTERCALATION TO EXFOLIATED HIGHLY ORIENTED PYROLYTIC GRAPHITE (e-HOPG)

4.1 Introduction

In Chapter 3, we have optimized the intercalation conditions for FLG. The FLG is expected for the applications such as transparent electrodes for solar cell [1] and others. The thicker MLG films are required for the application of interconnects and inductors to reduce the resistance further.

The theoretical studies have revealed that multilayer graphene is promising for on-chip inductor applications owing to its large momentum relaxation time, leading to large kinetic inductance [2–4]. Such inductor applications require high-crystalline thick MLG films with thicknesses of micrometer order. High inductance densities with good quality factors (up to 12) in on-chip spiral inductors at room temperature, using e-HOPG to mimic thick MLG films, demonstrated the advantage of bromine-doped MLG for inductor applications [3].

However, there was serious damage in e-HOPG while using the previously optimized condition for FLG in our preliminary experiment. Therefore, we optimized the intercalation condition, in terms of the doping efficiency, damage, and reduction of the sheet resistance for thick e-HOPG, by varying the chemical concentration, reaction temperature, and reaction time [5]. We discuss the mechanism of damage during the $MoCl_5$ intercalation process with strain analysis using the correlation plots of G and 2D peak positions in the Raman spectra [6-8]. Further, we investigated the stability of the $MoCl_5$-intercalated e-HOPG.

4.2 Experimental methods

The films exfoliated from a highly oriented pyro-lytic graphite (e-HOPG) were transferred to a SiO_2/Si substrate to mimic high-crystalline MLG film. The thickness was relatively high (10 ± 3 μm). The samples were inserted into a glass capsule with different

amounts of the chemical. The standard (STD) amount of chemical that was optimized for FLG in the previous study [5] was 0.62×10^{-3} mol-$MoCl_5$ and 0.23×10^{-3} mol-MoO_3, and it was varied as STD/2, STD/4, STD/5, and STD/6 in this study. After enclosing the sample and the chemicals in a glass capsule, it was inserted into a glass tube. Argon (Ar) gas flowed through the glass tube for 10 min. Before the reaction, the glass tube was pre-annealed at 110 °C for 120 min in an Ar atmosphere to remove moisture. The reaction temperature varied between 200 °C and 250 °C; the reaction time varied from 5 to 30 min. The heating rate was 10 °C/min, and the system was cooled naturally in the atmosphere.

The doping efficiency of e-HOPG was analyzed using a HORIBA HR-Evolution Raman spectroscope with 532 nm laser excitation. The root mean square (RMS) roughness and surface morphology were characterized using a Hitachi AFM5000II atomic force microscope (AFM) with the scanning area 5×5 µm^2 and Olympus LEXT OLS 4000 confocal laser microscope with evaluation area 1280×1280 µm^2. The morphology of e-HOPG was observed using a JEOL JSM-7100F scanning electron microscope (SEM). The sheet resistance was characterized by the 4-point probe method using a resistance meter, Hioki RM3544.

4.3 Results and discussion

Figure 4.1 shows the cross-sectional photo from SEM and surface morphology of the e-HOPG after transferring to a SiO_2/Si substrate. The Raman spectra of e-HOPG shows very high G/D ratio when compare to the few layer graphene from CVD process. So, the thickness is relatively thick as about 10 µm of e-HOPG was used to mimic a high crystallinity MLG film in this chapter.

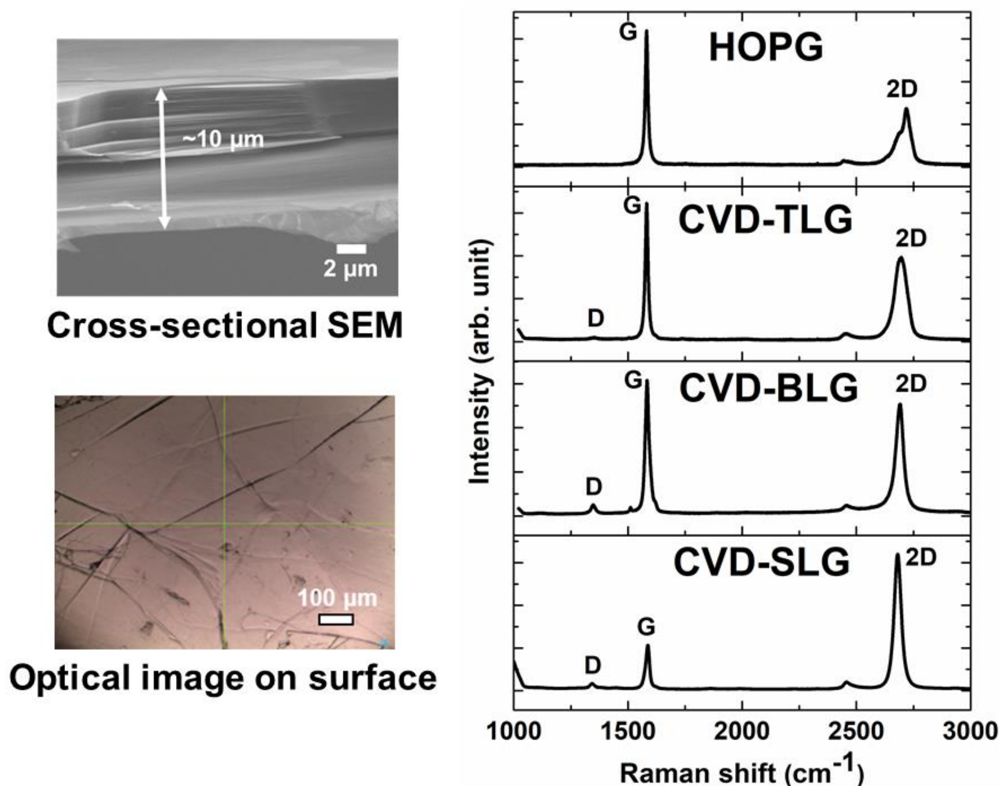

Figure 4.1. Cross-sectional photo from SEM, surface morphology from OM and Raman spectra of e-HOPG and FLG.

4.3.1 Chemical amount dependence of doping efficiency and damage

Figure 4.2 shows the G-band spectra of e-HOPG after intercalation at 200 °C for 30 min with varying amounts of the chemical. According to the position of the G-band, we could determine the intercalation stage. The G-band position around 1582 cm^{-1} (G_0) corresponds to the pristine graphite. After the $MoCl_5$ intercalation, the G-band position shifted to higher wavenumbers (G_1 and G_2 at 1605 and 1625 cm^{-1}, respectively) [9-11]. G_2 and G_1 correspond to stages 1 and 2 structures, respectively. In the case of higher-stage structures, the peak position depends on the ratio of the intensity of G_1 to that of G_0 (I_{G0}/I_{G1}). I_{G0}/I_{G1} of 0.5, 1, and 2 indicates stages 3, 4, and 5, respectively [10–11]. With the STD chemicals, only G_2 around 1625 cm^{-1} was observed in the G-band, indicating that stage 1 intercalation was achieved at a high amount of chemical. Reducing the amount of chemicals caused the G-band position to shift to a lower wavenumber, around 1616 cm^{-1} for STD/2 and STD/4

chemicals. The G-band of STD/2 and STD/4 could be fitted with two components corresponding to G_1 and G_2 positions, indicating the mixed structure of stages 2 and 1 intercalation. Further reduction of the amount of the chemical to STD/5 resulted in a non-doping state

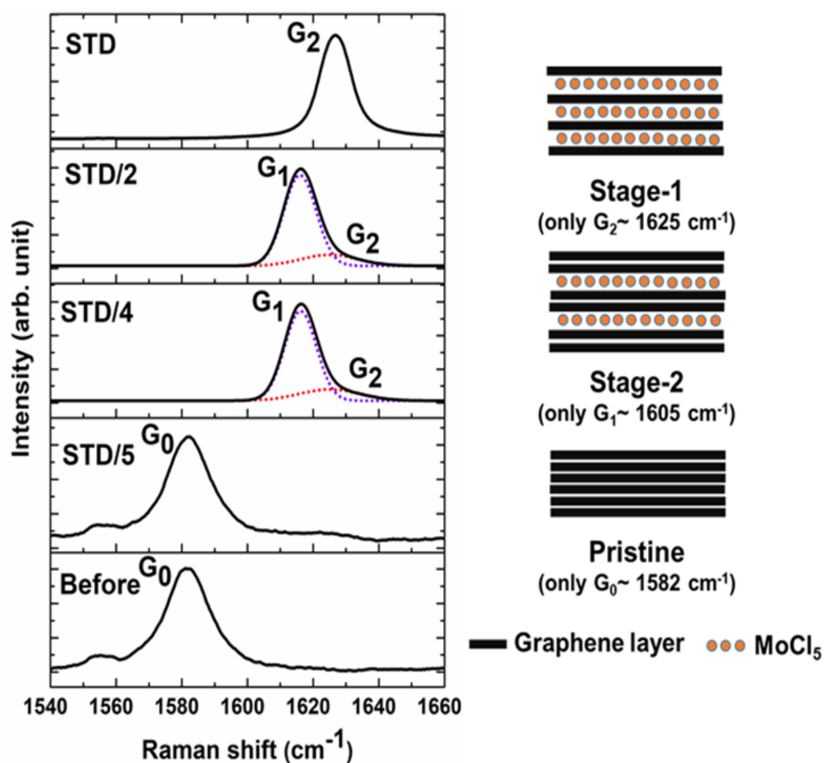

Figure 4.2. G-band spectra of e-HOPG after intercalation using 200ºC for 30 min.

Figure 4.3 shows the SEM images of the e-HOPG surface after intercalating with different amounts of chemicals at 200 ℃ for 30 min. The sample damage was reduced by reducing the amount of the chemical. The sample intercalated using STD/5 showed a smooth surface as that before the intercalation.

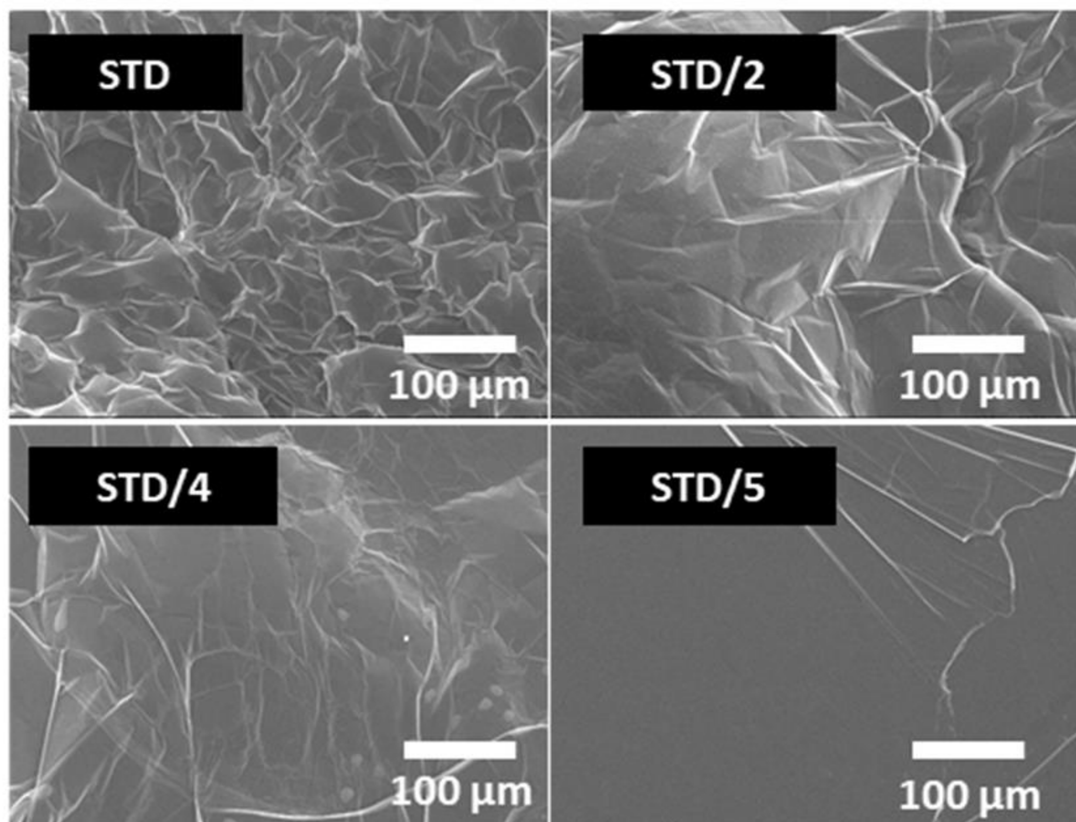

Figure 4.3. Surface SEM images of e-HOPG after intercalation at 200ºC for 30 min.

Table 4.1 shows the RMS roughness of e-HOPG obtained using a confocal laser microscope in an evaluation area of 1280 × 1280 µm^2 after intercalation with different amounts of chemicals at 200 °C for 30 min. The RMS roughness of the STD chemical was very high (55.98 µm) because of the MLG film's deformation after intercalation. However, the roughness was reduced to 3.24 µm by reducing the amount of chemical to STD/5. The RMS roughness of the STD/5 chemical was not much different from that before the intercalation.

Table 4.1. RMS roughness of e-HOPG after intercalation from confocal laser microscope.

Chemical amount	RMS roughness (μm)	
	Average	**SD**
STD	55.98	6.33
STD/2	52.83	2.50
STD/4	48.56	3.02
STD/5	3.24	1.88
Before intercalation	1.62	0.21

These results indicate that both doping efficiency and damage were reduced by reducing the chemicals, and there is a trade-off relation between doping efficiency and damage. Further optimization was performed with the reaction temperature using the low-chemical conditions.

4.3.2 Reaction temperature dependence of doping efficiency and damage

To enhance the doping efficiency of the damage-less chemical conditions, we explored the effect of temperature using STD/5 and STD/6 chemicals. Figure 4.4 shows the samples' G-band spectra after intercalating with STD/5 and STD/6 at different temperatures for 30 min.

At a low reaction temperature of 200 °C, the G-band spectra of the samples intercalated with STD/5 and STD/6 chemicals show only G_0 the same as that before the intercalation. At a reaction temperature of 225 °C, the G-bands of both STD/5 and STD/6 chemicals show G_0 and G_1 peaks. After fitting the peak for STD/6, the I_{G0}/I_{G1} was 0.99, which is similar to that of the stage 4 intercalation (I_{G0}/I_{G1} =1.00) [10–11]. For STD/5, both G_0 and G_1 peaks shifted to higher wavenumbers than those of STD/6. The I_{G0}/I_{G1} was 0.22, which is lower than 0.5 (stage 3), indicating that both stages 3 and 2 intercalations occurred. Increasing the chemical amount at the reaction temperature of 225 °C enhanced the doping efficiency.

When the temperature increased to 250°C, the G-band for both STD/5 and STD/6 chemicals shifted to a higher wavenumber than that of reaction temperature at 225 °C. After peak fitting, the G-band could be fitted with a small component of G_0 and the main component of G_1. I_{G0}/I_{G1} was 0.09 and 0.08 for STD/6 and STD/5, respectively, close to that of stage 2 intercalation (I_{G0}/I_{G1} = 0.00), but the small peak of G_0 was retained. Therefore, the

intercalation stage at the reaction temperature of 250 ℃ is considered mainly stage 2 and a small part of stage 3. The doping efficiency is higher than that at low reaction temperatures. These results indicate that increasing the temperature with a reduced amount of chemical enchanced the doping efficiency.

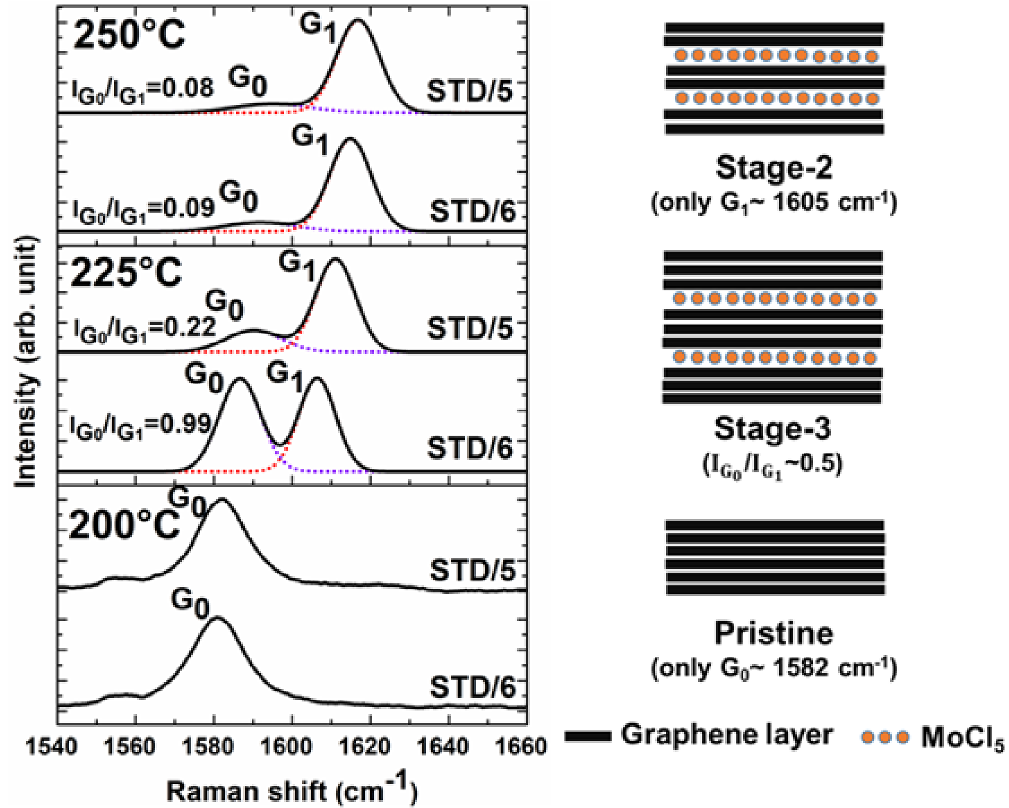

Figure 4.4. G-band spectra after intercalation using the STD/5 and STD/6 chemicals for 30 min.

Figure 4.5 shows the temperature-dependence of the sheet resistance (R_s)-reduction ratio before and after intercalation, ($R_{s\text{-}before} - R_{s\text{-}after}$) / $R_{s\text{-}before}$, with STD/5 and STD/6 chemicals for 30 min. The reduction ratio of sheet resistance increased with an increase in the reaction temperature. The higher amount of chemical (STD/5) showed more reduction in the sheet resistance than the lower amount of STD/6. At a low reaction temperature of 200 ℃, both STD/5 and STD/6 showed a very low sheet resistance decrease, below 10%. It agrees with the G-band results that show the non-doping stage at a low reaction temperature (Figure 4.4). At a reaction temperature of 225 ℃, STD/6 showed a lower percentage

reduction of 34% than the 73% for STD/5. At a high reaction temperature of 250 °C, the percentage of reduction of STD/5 and STD/6 increased to 88% and 80%, respectively. The sheet resistance reduction ratio is consistent with the G-band shifts shown in Figure 4.4.

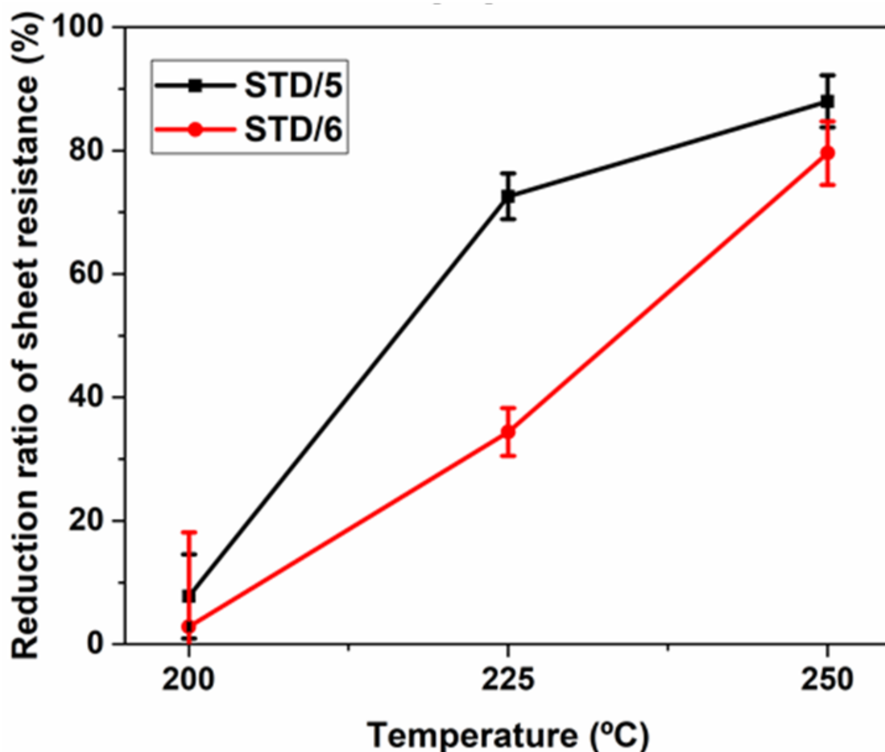

Figure 4.5. Relationship between the reduction ratio of sheet resistance between before and after intercalation for 30 min and the reaction temperature.

Figure 4.6 shows the samples' SEM images after the intercalation with STD/5 and STD/6 chemicals at different temperatures for 30 min. The line-shaped defects increased with an increase in temperature, both for STD/5 and STD/6. The defects could be the edge of MLG polycrystals, which is considered formed by the intercalation's compressive strain, as discussed later. At 200 °C, both STD/5 and STD/6 chemicals' surface morphology showed a smooth surface, the same as before the intercalation process. At the reaction temperature of 225 °C, STD/6 retained the smooth surface. In contrast, the morphology of STD/5 showed more damage than that of STD/6. However, the morphology of STD/6 degraded after raising the temperature to 250 °C, but it was still less damaged than that of STD/5 chemicals at the same temperature.

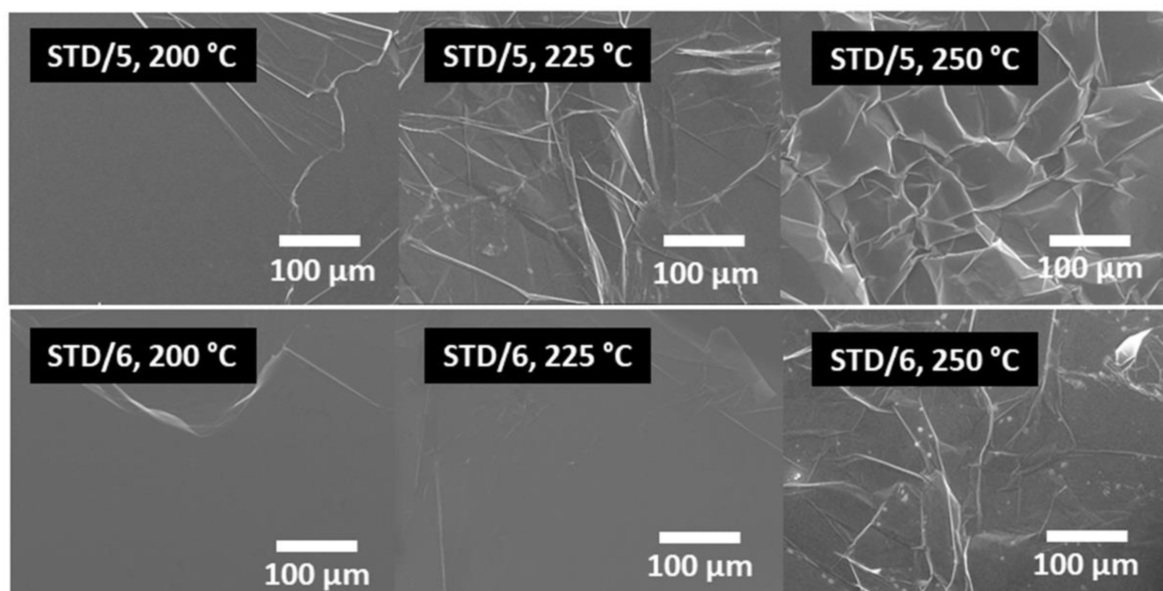

Figure 4.6. Surface morphology after intercalation process of STD/5 and STD/6 chemical for 30 min from SEM.

Figure 4.7 shows the surface morphology obtained from AFM after intercalating with STD/5 and STD/6 chemicals at different temperatures for 30 min. With STD/6, small hillocks were observed only at the high temperature of 250 ℃; however, with STD/5, they were observed at the reaction temperatures of 225 ℃ and 250 ℃. The images of the STD/5-intercalated sample also show line-shaped defects at 225 ℃ and 250 ℃. The defects are not the same as those observed in the SEM images.

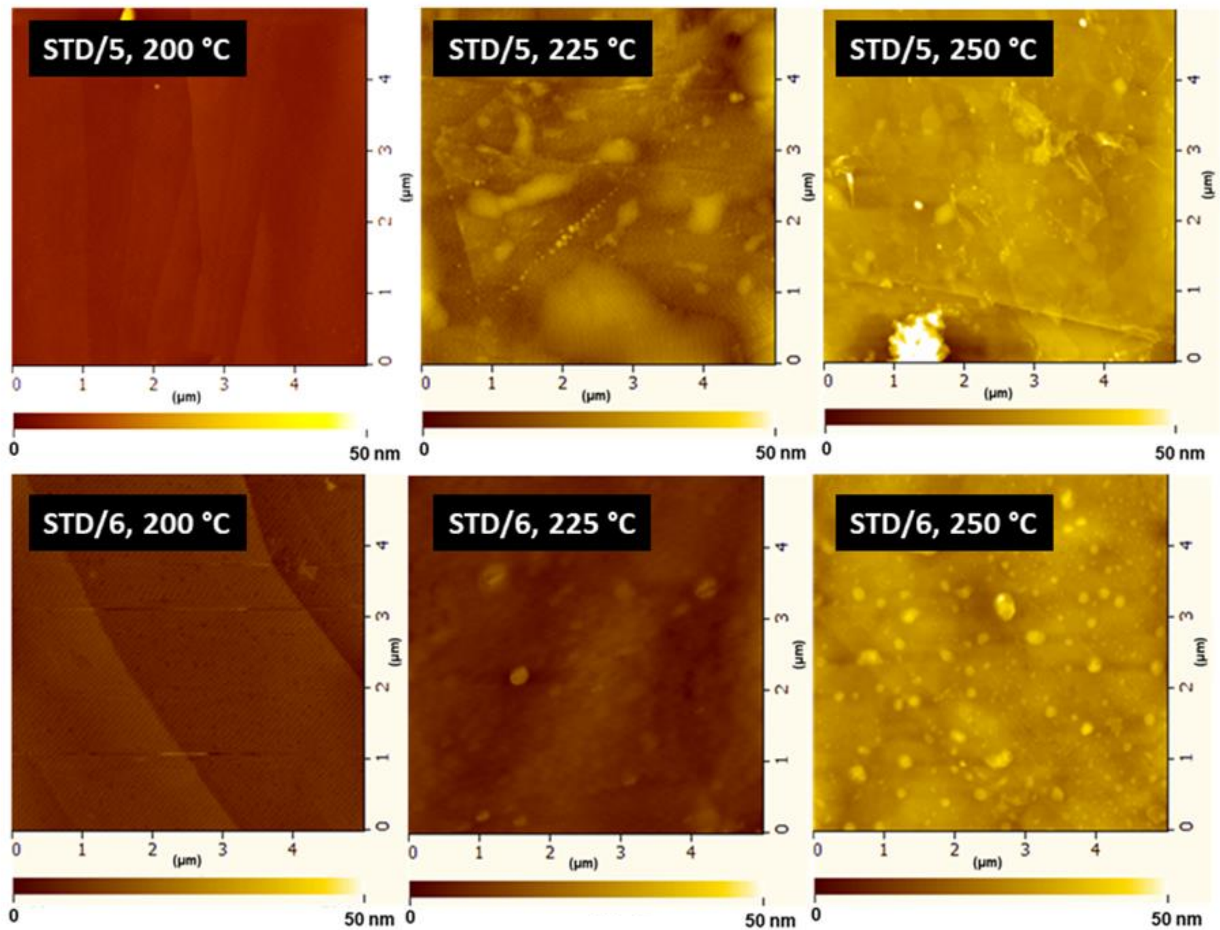

Figure 4.7. Surface morphology after intercalation process of STD/5 and STD/6 chemical for 30 min from AFM.

Table 4.2 lists the RMS roughness measured using the AFM in the scanning area of 5 × 5 μm^2. For the STD/6, the RMS roughness increased from 1.68 to 3.78 nm after increasing the reaction temperature from 200 °C to 250°C. The RMS roughness for STD/5 was higher than that of STD/6, and it increased from 1.73 to 11.07 nm as the reaction temperature increased from 200 °C to 250 °C. The hillocks and line defects increased the roughness.

Table 4.2. RMS roughness of e-HOPG after intercalation from AFM.

Chemical amount	Temperature (ºC)	RMS roughness (nm)
STD/5	250	11.07
	225	2.83
	200	1.73
STD/6	250	3.78
	225	1.75
	200	1.68
Before intercalation		1.47

These results indicate that both doping efficiency and damage were increased by increasing the reaction temperature, and further optimization is required to reduce the damage. On the other hand, a 73% decrease in the sheet resistance with less damage was achieved after intercalating with STD/5 chemical at 225°C for 30 min. To further reduce the damage, we optimized the reaction time using the STD/5 chemical at 225 °C, as presented in the next section.

4.3.3 Reaction time dependence of doping efficiency and damage

To optimize the intercalation conditions further, the effect of reaction time was explored using the STD/5 chemical with 225°C conditions. Figure 4.8 shows the G-band spectra after intercalating at 225°C for different reaction times using STD/5. When the reaction time was reduced to 15 min, the G-band could be fitted with two components corresponding to the G_0 and G_1 positions, and I_{G0}/I_{G1} was 0.22, indicating the combination of stages 2 and 3 intercalation, the same as for the reaction time of 30 min. For the reaction time of 10 min, the G_0 and G_1 positions shifted to lower positions than those of 15 and 30 min, and I_{G0}/I_{G1} was 0.44, close to 0.50 (stage 3), indicating the intercalation was almost stage 3. Reducing the reaction time further to 5 min, the G-band showed the non-doping stage.

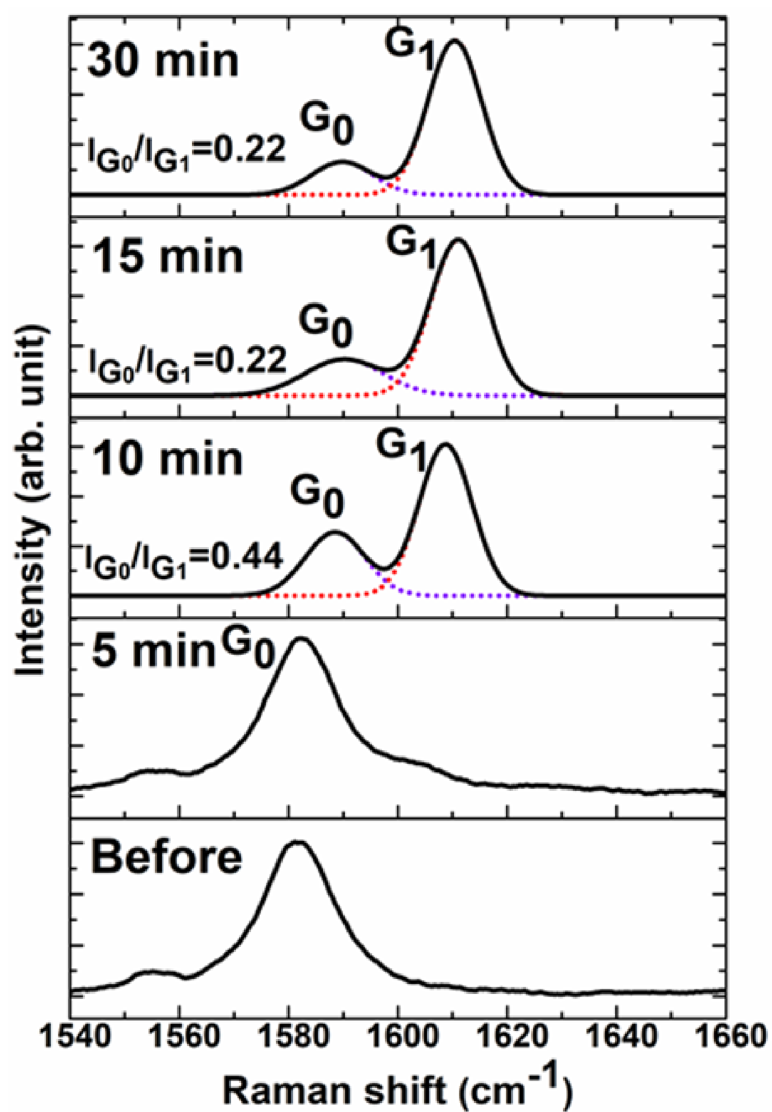

Figure 4.8. G-band spectra after intercalation using the STD/5 chemicals with 225°C.

Figure 4.9 shows the reaction time-dependence of sheet resistance reduction before and after intercalation at 225 °C using STD/5. The percentage reduction ratio of sheet resistance increased with an increase in the reaction time. The sheet resistance reduction was significant, 57% and 77%, for 10 and 15 min reaction times, respectively. The reduction is comparable with that of Br_2 intercalation [3].

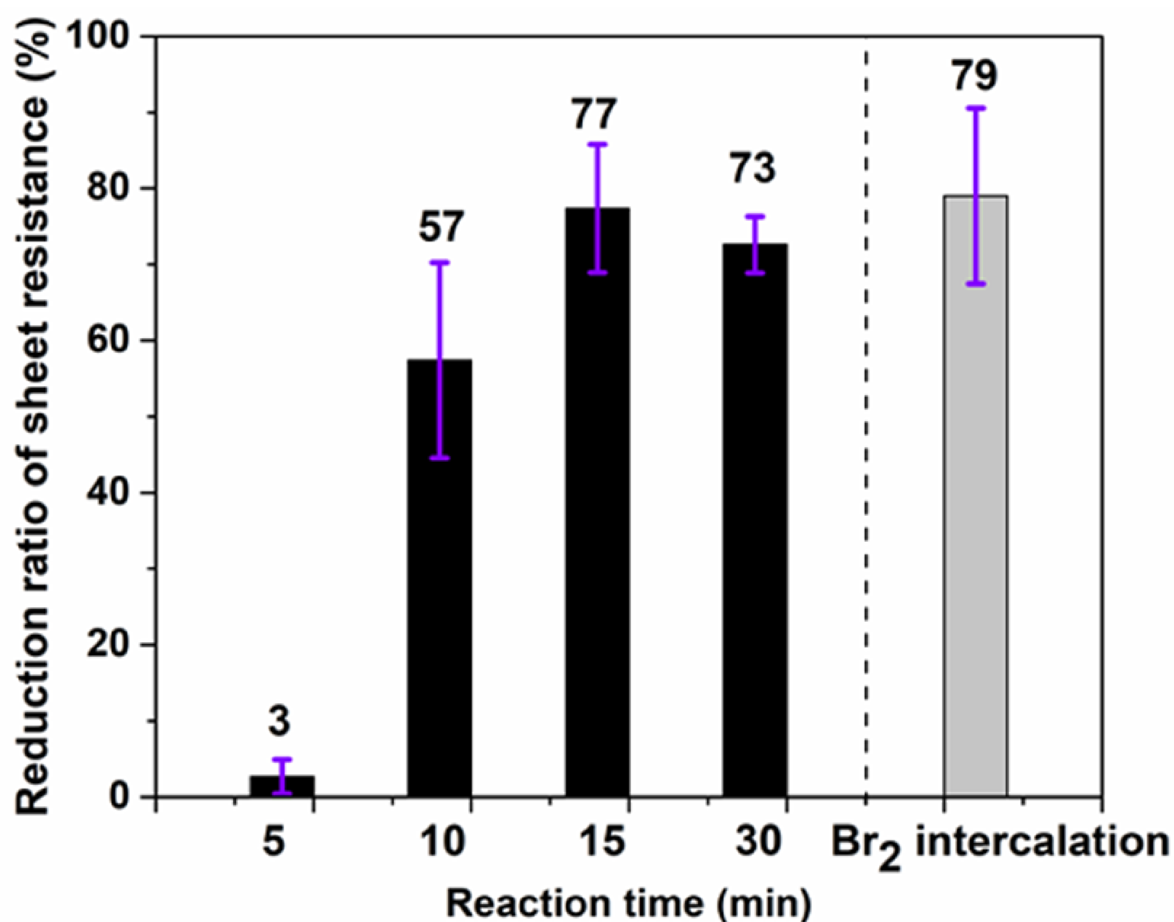

Figure 4.9. Relationship between the reduction ratio of sheet resistance between before and after intercalation using the STD/5 chemical with 225℃ and the reaction time.

Figure 4.10 shows the SEM images of e-HOPG after intercalating with STD/5 at 225 ℃ for different reaction times. As expected, the damage of samples reduced as the reaction time was reduced. The surface damage was relatively reduced as the reaction time reduced from 30 to 15 min, and a smooth surface similar to the pristine surface was obtained at the reaction time of 10 min.

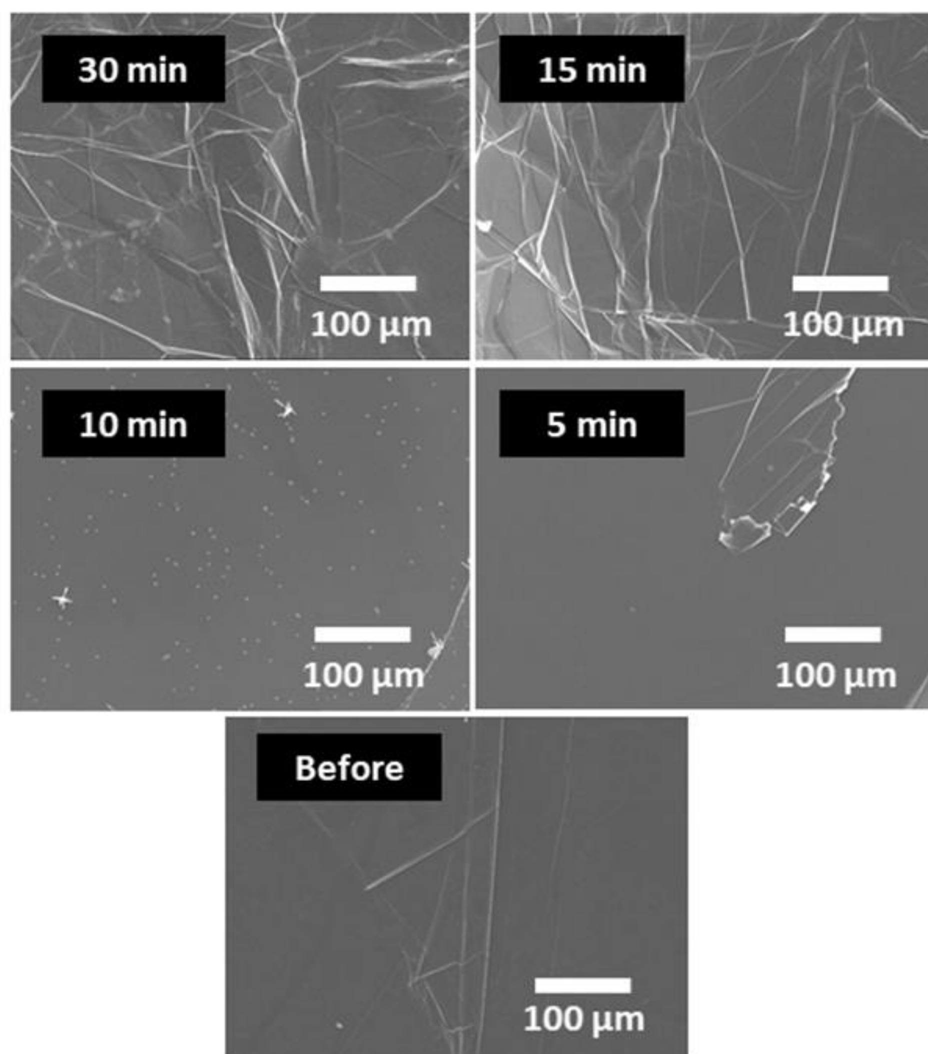

Figure 4.10. Surface SEM images of e-HOPG after intercalation process using STD/5 chemical with 225°C.

Figure 4.11 shows the surface morphology obtained from AFM after intercalation at 225 °C using STD/5. The size of the hillocks was reduced as the reaction time decreased. Although the line-shaped defects appeared in the SEM image of the sample with a reaction time of 15 min, the AFM images show a smoother surface at a reaction time of 15 min than that of 30 min. The stress that was induced by the intercalation process could be the cause of the small hillocks on the surface and the line-shaped defects. Longer reaction times could enhance the stress and defects simultaneously.

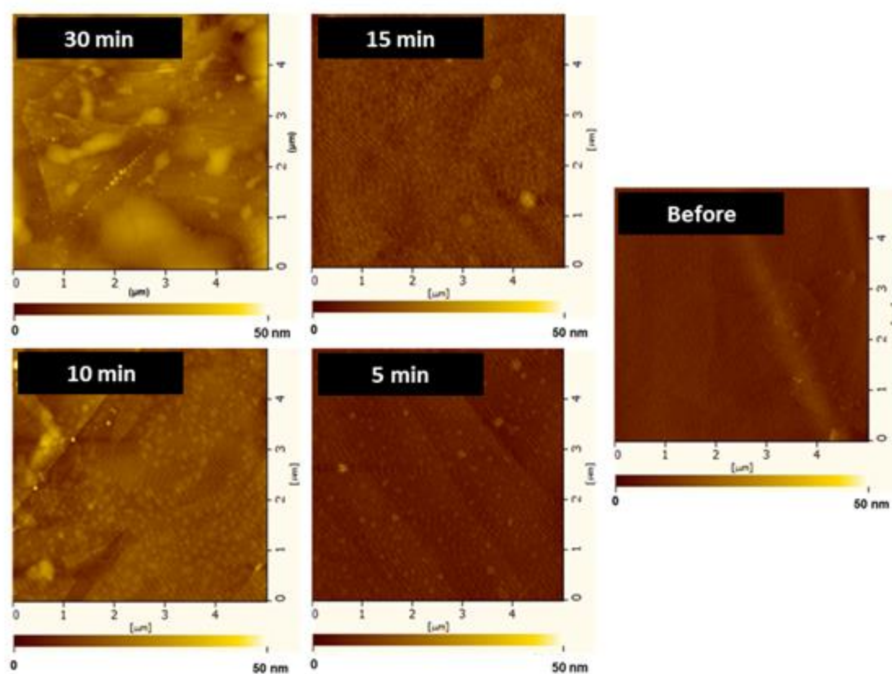

Figure 4.11. Surface morphology images of e-HOPG after intercalation process using STD/5 chemical with 225°C from AFM.

Table 4.3 lists the RMS roughness measured using the AFM in the scanning area of $5 \times 5\ \mu m^2$. The RMS roughness increased from 1.58 to 2.83 nm as the reaction time increased from 5 to 30 min. We infer that the hillocks and defects caused the increase in the RMS roughness.

Table 4.3. RMS roughness of e-HOPG after intercalation using STD/5 chemical with 225°C by AFM.

Time (min)	RMS roughness (nm)
Before intercalation	1.47
5	1.58
10	3.11
15	2.35
30	2.83

Considering the doping efficiency, reaction times above 15 min were preferable. On the other hand, considering the surface's smoothness, reaction times below 15 min were better.

4.3.4 Strain and charge density of HOPG after $MoCl_5$ intercalation process

This section shows the correlation between the G- and 2D-peak positions after the intercalation process. The mechanical strain (ε) and hole density (*n*) of e-HOPG could be determined from the correlation. In this section also shows the experimental and theoretical suspended graphene data (without strain and doping stage), strain line, and hole-doping line and those from previous reports [6–8]. Negative values of strain indicate compressive strain (graphene sheet is shrinking in-plane).

Figure 4.12 shows the correlation between the G- and 2D-peak positions after intercalation at temperatures of 225 °C and 250 °C using STD/6 and STD/5 for the reaction time of 30 min. With the STD/6 chemical, the strain increased from −0.2% to −0.4%, and the hole density increased from about 10×10^{12} to 15×10^{12} cm^{-2} as the temperature increased from 225 °C to 250 °C. With the STD/5 chemical, the hole density was high 15×10^{12} cm^{-2} at both 225 °C to 250 °C. The strain was also higher at 225 °C than that of STD/6. These indicate that higher compressive strain after intercalation induces damage on e-HOPG. Also, higher hole density results in more sheet resistance reduction, as shown in Figure 4.5. Moreover, the temperature effect was more significant for lower amounts of the chemical.

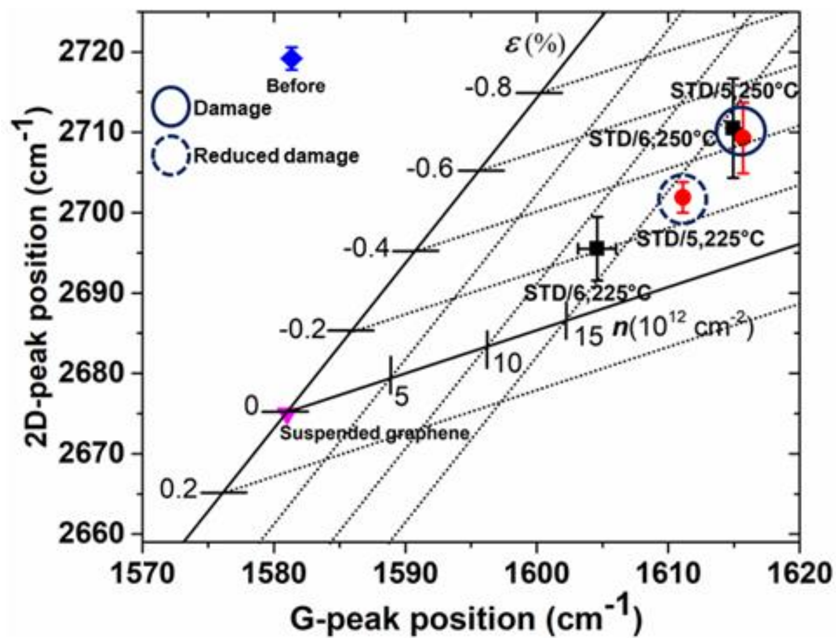

Figure 4.12. Correlation between the G-peak position and 2D-peak position after intercalation of temperature dependence of STD/5 and STD/6 chemicals for 30 min.

Figure 4.13 shows the correlation between the G- and 2D-peak positions at 225 ℃ for different reaction times using STD/5. The mechanical strain was independent of the reaction time. On the other hand, the hole density increased from about 10×10^{12} to above 15×10^{12} cm^{-2} as the reaction time increased from 10 to 30 min. The SEM images show that the damage on e-HOPG increased as the reaction time increased from 15 to 30 min (Figure 4.10). There was no much difference between the mean value of strain for 15 and 30 min, and the strain variation reduced at the reaction time of 30 min. The uniformity of the $MoCl_5$ intercalation improved with increasing time.

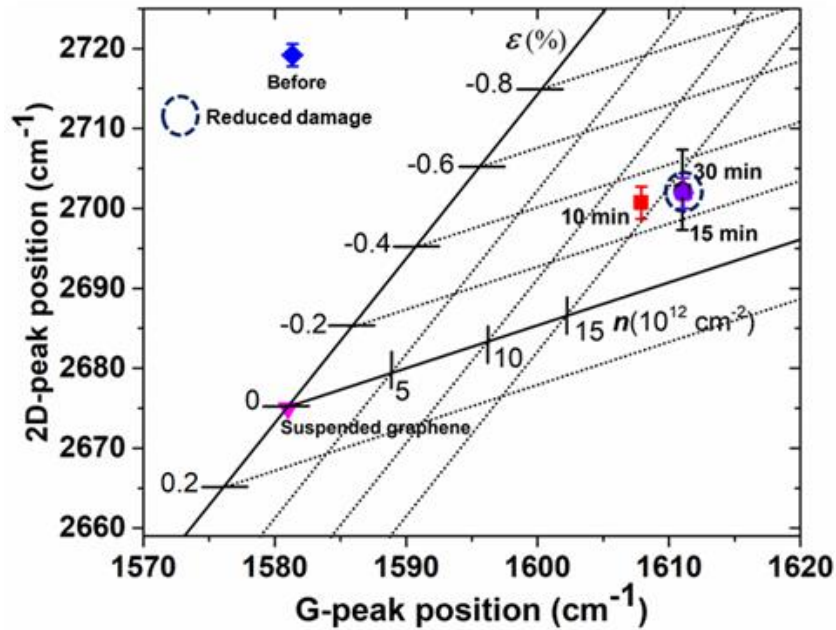

Figure 4.13. Correlation between the G-peak position and 2D-peak position after intercalation of time dependence using STD/5 chemical at 225°C.

Figure 4.14 shows a schematic illustration of the mechanism of damage formation during the $MoCl_5$ intercalation process. The e-HOPG consists of polycrystals of high-crystalline MLGs. During the intercalation process, a higher amounts of chemicals and temperature result in a higher vapor pressure and intercalation rate. The higher vapor pressure and temperature, in turn, result in more intercalation and increase the interlayer space, inducing more strain (Figure 4.12 and Figure 4.13). This results in the formation of defects in the polycrystalline e-HOPG [1, 9, 13]. If there is nonuniform intercalation in each MLG crystal, the defect will form at the MLG crystals' edge due to the different increase in thickness. It is reasonable that the defect is line-shaped along the MLG edges.

The carrier scattering at the MLG crystals' edge observed as the roughness is considered to reduce the mean free path and leads to the mobility degradation [12]. So, the damage of e-HOPG must be minimized to eliminate the degradation of carrier mobility to reduce the sheet resistance after the intercalation process.

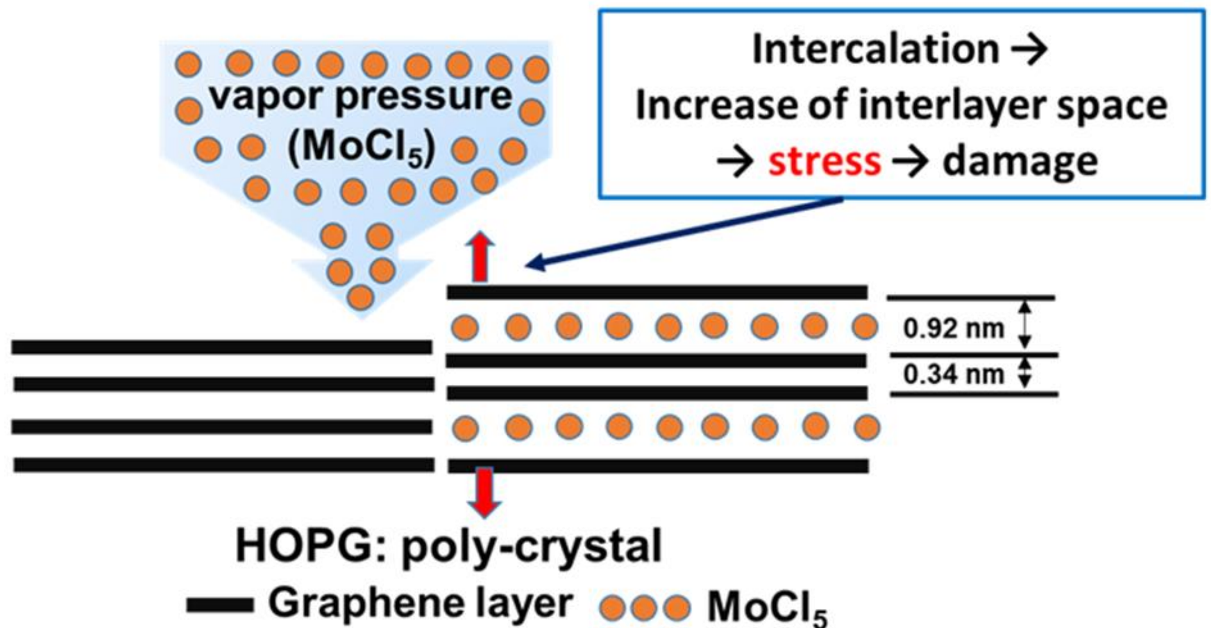

Figure 4.14. Schematic model to explain the mechanism for damage with $MoCl_5$ intercalation process.

For a e-HOPG thickness of about 10 μm, the optimized intercalation was a combination of stages 2 and 3, which enlarges the interlayer spacing between 85% and 43% of the pristine graphite (the interlayer spacing increased from 0.34 nm for graphite to 0.92 nm after $MoCl_5$ intercalation). Accordingly, stress and strain were induced. The accumulated stress is considered the cause of damages, increasing with the number of layers. Therefore, the damage induced by the intercalation should be reduced by reducing the number of layers. Although further investigation is required, further enhancement of doping density is expected for thinner MLGs by optimizing the intercalation conditions and balancing between high doping density and less damage for the optimum condition to realize the lowest sheet resistance.

4.3.5 Stability of doping efficiency and sheet resistance

To study the stability of doped e-HOPG, the samples were stored in an N_2 box, and we evaluated the doping efficiency and sheet resistance every week. Figure 4.15 shows the G-band spectra after intercalation with STD/5 at 225 °C and 225 °C for 30 min and stored in an N_2 box for 12 and 40 weeks. The G-bands at both reaction temperatures did not significantly change after storing in the N_2 box for 40 weeks.

Figure 4.16 shows the relationship between the reduction ratio of the sheet resistance before and after intercalating with STD/5 for 30 min at different storage times and reaction temperatures. The percentage reduction of sheet resistance decreased after storing in the N_2 box for 40 weeks. However, the error bars overlap, indicating no significant change in the sheet resistance. These results confirm the stability of $MoCl_5$-doped MLG, as reported previously.

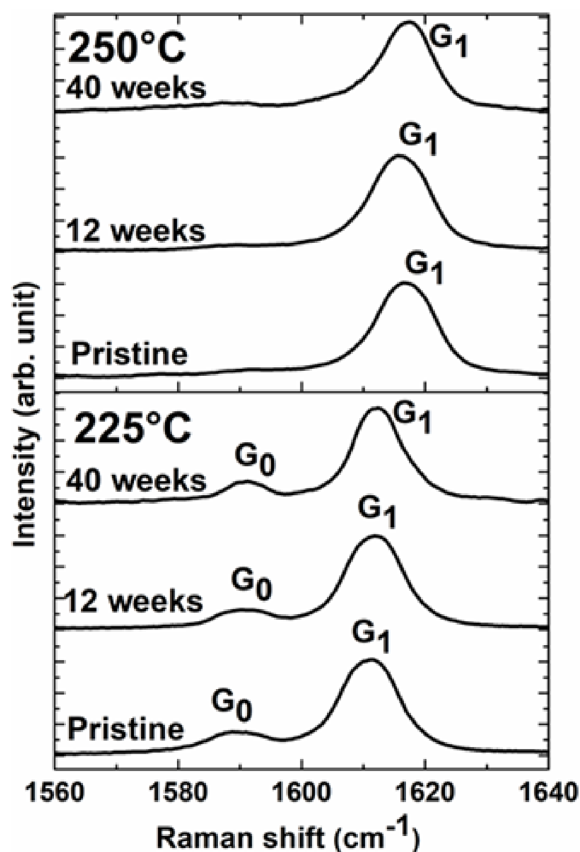

Figure 4.15. G-band spectra after intercalation using the STD/5 with 225℃ and 250℃ for 30 min after storage for 40 weeks.

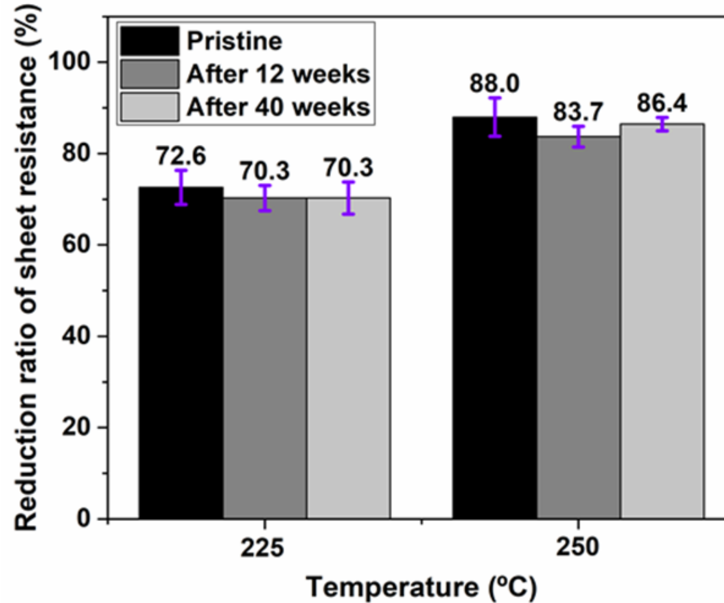

Figure 4.16. Reduction ratio of sheet resistance between before and after intercalation using the STD/5 chemical for 30 min after storage for 40 weeks.

4.4 Summary and conclusions

This chapter optimized the $MoCl_5$ intercalation process for relatively thick e-HOPG films in terms of resistance and damage. We achieved a 77% decrease in sheet resistance with reduced damage by reducing the amount of chemical to 1/5 of that of FLG at 225 °C for 15 min. The strain and hole density induced during the intercalation process were analyzed using G and 2D peaks' correlation plots. The changes in the strain and carrier density agree well with the observed damage and sheet resistance. Strain is considered to be induced during the intercalation, resulting in line-shaped defects. Since the induced strain depends on the MLG thickness, a further decrease in damage is expected for thinner films. The sheet resistance reduction effect of $MoCl_5$ intercalation is comparable to that of Br-intercalation used to demonstrate doped MLG inductors with high inductance density. Therefore, $MoCl_5$ intercalation is promising for thick MLG applications, such as on-chip inductors, due to its environmental stability and doping efficiency. Optimizing the intercalation conditions in terms of thickness is essential for $MoCl_5$ intercalation to resolve the trade-off between doping concentration and damage due to intercalation.

References

[1] H. Kinoshita, I. Jeon, M. Maruyama, K. Kawahara, Y. Terao, D. Ding, R. Matsumoto, Y. Matsuo, S. Okada and H. Ago, Adv Mater. **29**, 1702141 (2017).

[2] X. Li, J. Kang, X. Xie, W. Liu, D. Sarkar, J. Mao and K. Banerjee, Proc. IEEE Int. Electron Devices Meeting, 2014, pp. 5-4.

[3] J. Kang, Y. Matsumoto, X. Li, J. Jiang, X. Xie, K. Kawamoto, M. Kenmoku, J. H. Chu, W. Liu, J. Mao, K. Ueno and K. Banerjee, Nat. Electron. **1**, 46-51(2018).

[4] K. Agashiwala, A. Pal, W. Cao, J. Jiang and K. Banerjee, Proc. IEEE Int. Electron Devices Meeting, 2018, p. 24.4.

[5] E. Ketsombun and K. Ueno, Proc. Int. Conf. Solid State Devices and Materials, 2020, pp127-128.

[6] J. E. Lee, G. Ahn, J. Shim, Y. S. Lee, S. Ryu, Nat. Commun. **3**, pp. 1-8 (2012).

[7] U. Lee, Y. Han, S. Lee, J. S. Kim, Y. H. Lee, U. J. Kim, H. Son, ACS Nano. **14**, pp.919−926 (2019).

[8] B. Li, D. Luo, L. Zhu, X. Zhang, S. Jin, M. Huang, F. Ding, R. S. Ruoff, Adv. Mater. **30**, 1706504 (2018).

[9] H. Miyazaki, R. Matsumoto, M. Katagiri, T. Yoshida, K. Ueno, T. Sakai and A. Kajita, Jpn. J. Appl. Phys. **56**, 04CP02 (2017).

[10] R. Matsumoto and N. Akuzawa, Mater. Today Commun. **20**, 100532 (2019).

[11] M.S. Dresselhaus and G. Dresselhaus, Adv. Phys. **30**, 139-326 (1981).

[12] A. Contino, I. Ciofi, X. Wu, I. Asselberghs, U. Celano, C. J. Wilson, Z. Tőkei, G. Groeseneken, and B. Sorée, IEEE Electron Device Lett., 39, pp. 1085-1088 (2018).

[13] P. Xiong, F. Zhang, X. Zhang, S. Wang, H. Liu, B. Sun, J. Zhang, Y. Sun, R. Ma, Y. Bando, C. Zhou, Z. Liu, T. Sasaki and G. Wang, Nat. Commun. **11**, 3297 (2020).

CHAPTER 5
INTERCALATION OF CVD-MLG

5.1 Introduction

From the discussion in Chapter 1, doped MLG is expected to be a high-inductance material because of its large kinetic inductance, which has not been apparent in conventional metals, such as copper [1–4]. Principle verification of the high-inductance density of doped MLG was demonstrated using MLG e-HOPG and Br intercalation [1]. To realize the production of high-performance inductors using doped MLG, it is necessary to develop a more practical manufacturing method. In Chapter 4, we optimized the intercalation conditions for thick MLG using e-HOPG to mimic thick MLG. However, e-HOPG is not a practical method for device manufacture. In this chapter, we study the intercalation of thick MLG fabricated by CVD as a practical fabrication method. We developed a thermal CVD process that is expected to deposit high-crystallinity MLG patterns at a wafer scale, although the accompanying deposition temperature is high. We optimized the conditions for CVD and $MoCl_5$ intercalation to obtain a lower sheet resistance of doped CVD-MLG.

5.2 Experimental methods

Multilayer graphene was grown on an 800-nm-thick Ni film on SiO_2/Si by the CVD process using an ethanol precursor with Ar bubbling gas. The CVD temperature was varied between 800 ℃ and 900 ℃, with the same Ar flow rate of 50 sccm, for 10 min. The CVD-MLG on Ni catalyst was inserted into a glass capsule with 0.0374 g of $MoCl_5$ and 0.0073 g of MoO_3. After enclosing the glass capsule, it was inserted into a glass tube. Ar gas was flowed through the glass tube for 10 min, then heated up to a pre-annealed temperature of 110 ℃ for 120 min before reaction. The reaction temperature was varied between 225 ℃ and 130 ℃ for 30 min. The doping efficiency and crystallinity of the CVD-MLG were analyzed using a HORIBA HR-Evolution Raman spectroscope with 532-nm laser excitation. The morphology was observed by optical microscopy. The root mean square (RMS) roughness and surface morphology were characterized using a Hitachi AFM5000II atomic force

microscope with scanning areas of 5 × 5 μm^2 and 500 × 500 nm^2. The cross-section and surface morphology of the CVD-MLG were observed using a JEOL JSM-7100F SEM. The composition of the CVD-MLG was analyzed using an energy-dispersive X-ray analyzer (EDX) installed with a SEM. The sheet resistance was characterized by the four-point probe method using a resistance meter, Hioki RM3544.

5.3 Results and discussion

5.3.1 Optimization of CVD temperature from crystallinity and morphology of CVD-MLG

Figure 5.1 shows optical images of CVD-MLG at different CVD temperatures. The morphology from optical microscopy is different at each CVD temperature. At lower magnification, the region of uniformity appears to increase with the increase in CVD temperature, from 800 ºC to 900 ºC. The more uniform surface morphology may be an advantage for patterning.

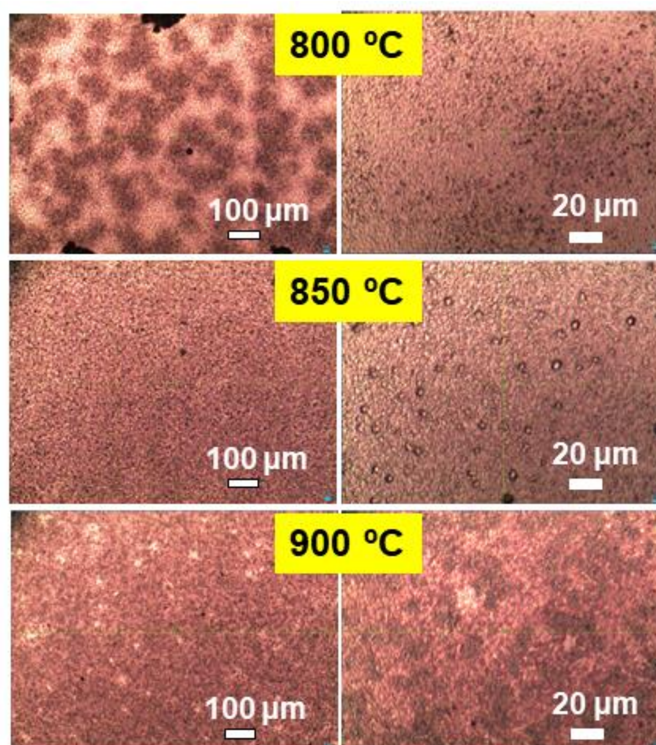

Figure 5.1. Optical images of CVD-MLG at different CVD temperatures.

Figure 5.2 shows the Raman spectra of CVD-MLG on Ni catalyst at different CVD temperatures. The spectra consist of D-, G-, and 2D-bands [5]. The G/D ratio, which indicates the crystallinity [6–8] of MLG, tends to increase from 9 to 88 as the CVD temperature increases from 800 ºC to 900 ºC. Higher CVD temperatures may lead to the formation of higher crystallinity CVD-MLG.

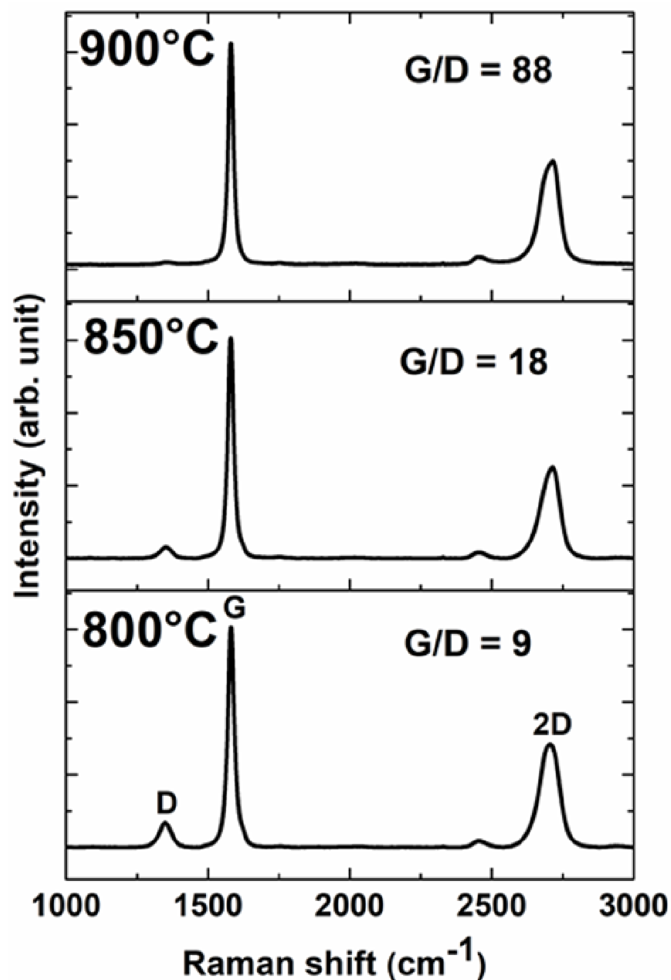

Figure 5.2. Raman spectra of CVD-MLG on Ni catalyst at different CVD temperatures.

Figure 5.3 shows the surface morphology via SEM images at different CVD temperatures. There is little difference in the morphology for CVD temperatures ranging from 800 ºC to 850 ºC. However, the surface of CVD-MLG at a CVD temperature of 900 ºC appears smoother than that grown at lower CVD temperatures. The lesser thickness of CVD-MLG grown at higher CVD temperatures may be the cause of the smooth surface at 900 ºC.

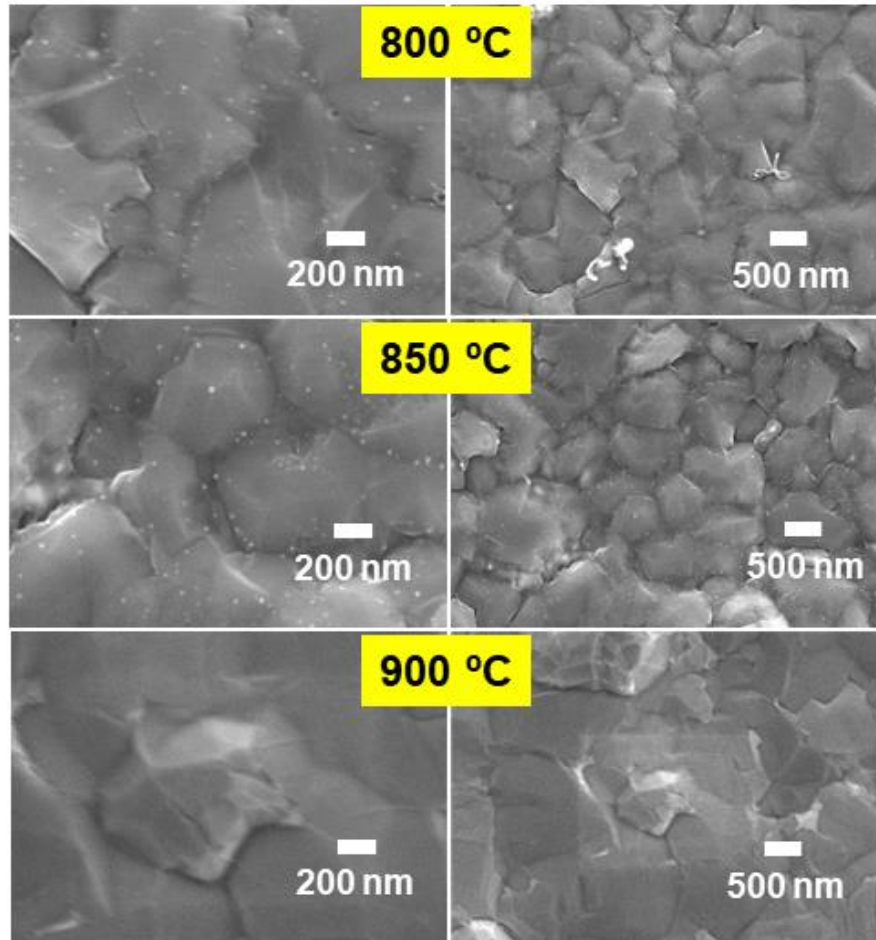

Figure 5.3. Surface morphology of CVD-MLG on Ni catalyst grown at different CVD temperatures via SEM.

Figure 5.4 shows the surface morphology and RMS roughness using scanning area 500×500 nm^2 of CVD-MLG at different CVD temperatures via AFM. The AFM surface morphology corresponds to the surface morphology observed in the SEM results. A CVD temperature of 850 ℃ shows a higher RMS roughness of 3.88 nm than that for CVD temperatures of 800 ℃ and 900 ℃. However, the high-crystallinity CVD-MLG at 900 ℃ shows the lowest RMS roughness at 1.2 nm. Higher crystallinity with low roughness may be suitable for use during the patterning of CVD-MLG for inductor applications.

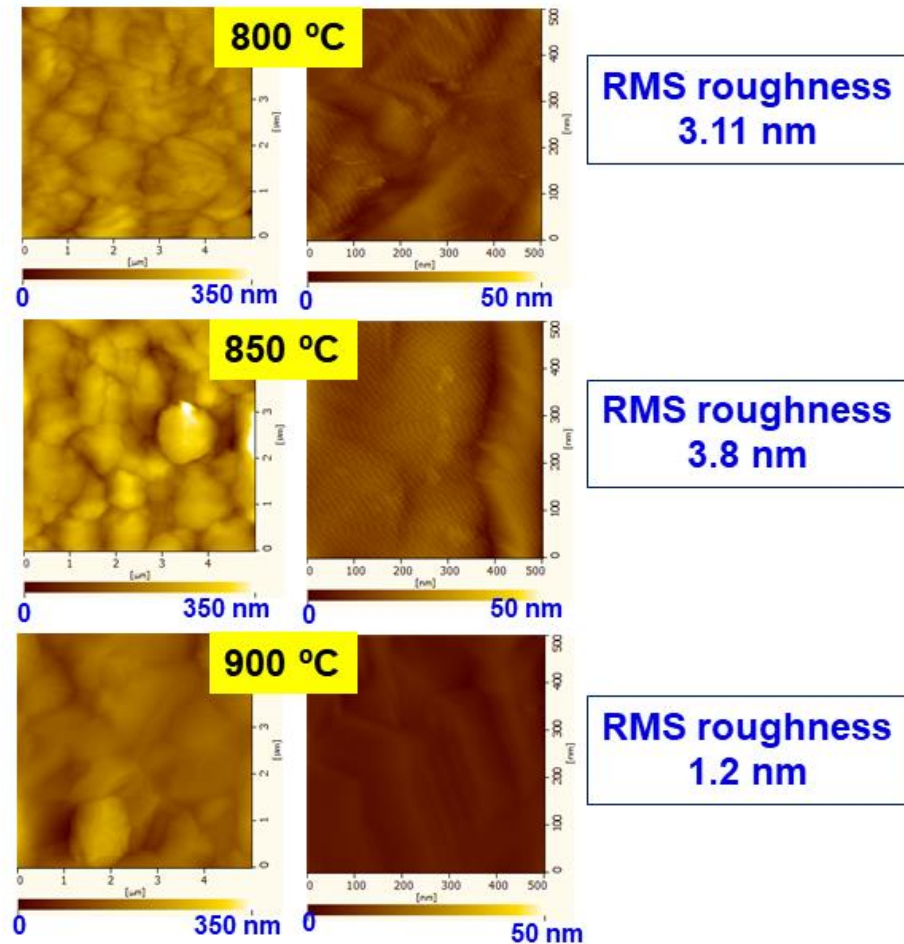

Figure 5.4. AFM surface morphology and RMS roughness of CVD-MLG grown at different CVD temperatures.

Figure 5.5 shows cross-sectional SEM images of CVD-MLG at different CVD temperatures. The cross-sectional SEM shows the film was composed with the stacked layers of MLG layer and Ni layer. As the CVD temperature increases from 800 ºC to 900 ºC, the thickness of the CVD-MLG decreases, although exact thickness is difficult to be measured due to the deformation of Ni film during scribing.

Figure 5.6 shows cross-sectional EDX mapping of CVD-MLG at a CVD temperature of 900 ºC. The top of the surface indicates a C-rich area, which corresponds to the CVD-MLG layer. Under the CVD-NLG layer, the Ni area is observed, followed by the SiO_2 layer,

as indicated by an O-rich line, and the last layer is the Si substrate. The EDX results confirm the composition of the CVD-MLG.

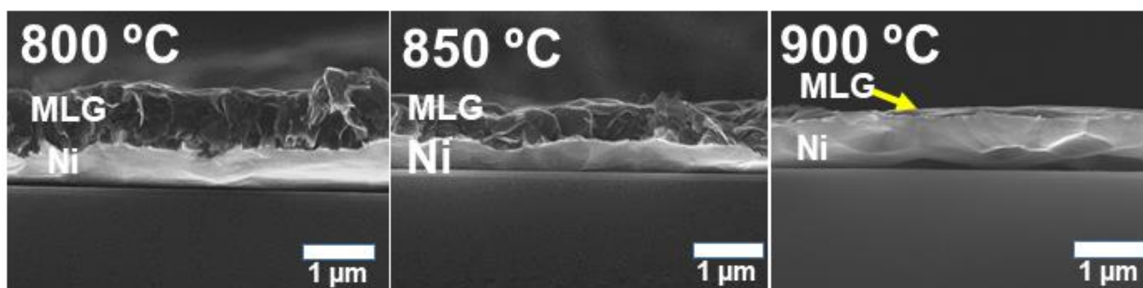

Figure 5.5. Cross-sectional SEM images of CVD-MLG at different CVD temperatures.

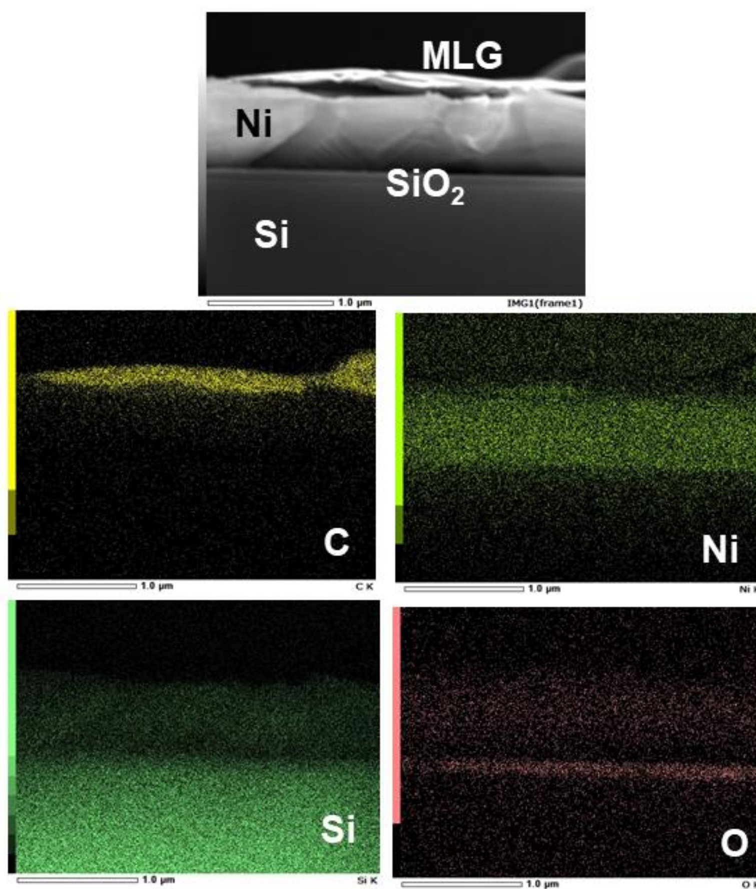

Figure 5.6. EDX mapping of cross-sectional CVD-MLG after CVD growth at 900 ºC.

Figure 5.7 shows the sheet resistance of CVD-MLG grown at different CVD temperatures. The resistance of the CVD-MLG films is lower than that of the Ni catalyst (0.388 Ω/sq. This lower resistance after the CVD process may be from the effect of the resistance of graphene and improved crystallinity of Ni by annealing at a high temperature. Moreover, the resistance of CVD-MLG decreases, from 0.236 to 0.140 Ω/sq, with increasing CVD temperature, from 800 ℃ to 900 ℃. The higher crystallinity of CVD-MLG and the lesser surface roughness at 900 ℃ may reduce the sheet resistance.

From the abovementioned results, variations in CVD temperature lead to CVD-MLG with different properties. Higher crystallinity, greater uniformity, and lower roughness are properties necessary for inductor fabrication. A CVD temperature of 900 ℃ provides the best CVD-MLG film properties for inductor fabrication. However, $MoCl_5$ intercalation of CVD-MLG must be optimized for the patterning of CVD-MLG.

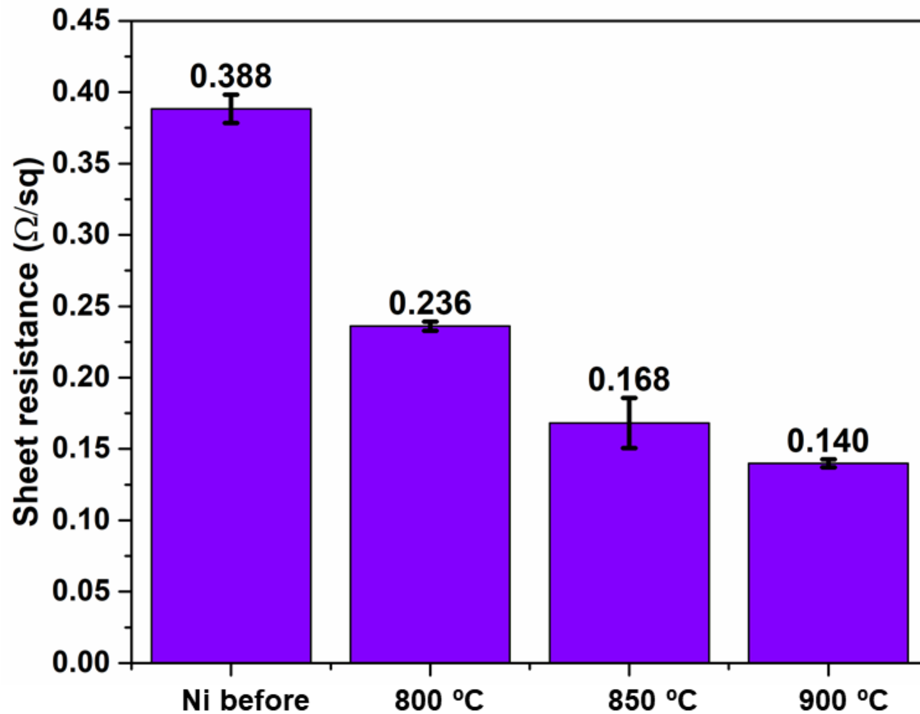

Figure 5.7. Sheet resistance of CVD-MLG after the CVD process at different CVD temperatures.

5.3.2 Doping efficiency dependence on CVD-MLG

Figure 5.8 shows the Raman spectra of CVD-MLG on Ni catalyst after reaction at different reaction temperatures. According to the position of the G-band, we can determine the intercalation stage. The G-band position around 1582 cm^{-1} (G_0) corresponds to pristine graphite. After $MoCl_5$ intercalation, the G-band position shifts to a higher wave number ($G_1 \approx 1605$ cm^{-1} and $G_2 \approx 1625$ cm^{-1}) [9–12]. G_1 and G_2 correspond to stage 1 and stage 2 structures, respectively. In the case of higher stage structures, the peak position depends on the ratio between the intensity of the G_1 and G_0 bands (I_{G0}/I_{G1}). In the case of a lower CVD temperature of 800 ºC, the G-band after low intercalation at 225 ºC and 250 ºC is the same as that before the intercalation process (only G_0). After raising the intercalation temperature to 300 ºC, the G-band shifted to 1606 cm^{-1} and was mixed between G_0 and G_1 with a ratio of 0.22 (mixed stage 2 and stage 3). On the other hand, the G-band for high CVD temperature (900 ºC) shows a mix between G_0 and G_1 at a ratio of 2.66 (stage 5) at a low intercalation temperature of 225 ºC. The intensity of G_1 increases as the intercalation temperature increases and, consequently, the I_{G0}/I_{G1} ratio decreases from 0.25 to 0.08 (stage 2) after raising the intercalation temperature from 250 ºC to 300 ºC. This result indicates that the doping efficiency is enhanced by the intercalation temperature.

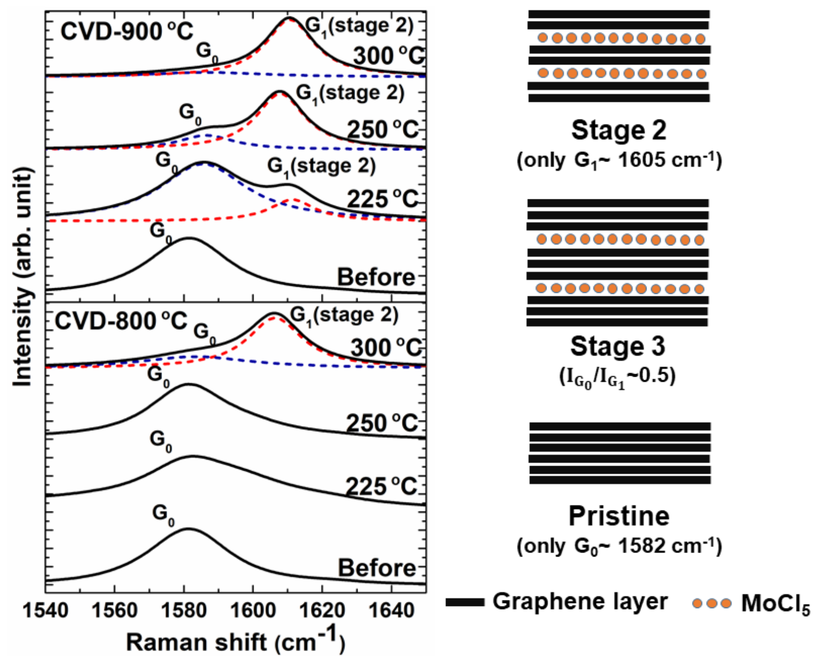

Figure 5.8. G-band spectra of CVD-MLG after intercalation for 30 min.

Figure 5.9 shows the relationship between the G-peak position of CVD-MLG after intercalation at different temperatures and the G/D ratio before intercalation. At low intercalation temperatures of 225 ℃ and 250 ℃, the G-peak position shifted to ~1600 cm^{-1} and was the only high G/D ratio condition. With a higher intercalation temperature of 300 ℃, the G-peak position of all G/D ratios were shifted to more than 1605 cm^{-1}, which corresponds to stage 2 or stage 3. However, the G-peak positions for higher G/D ratios seem to shift by more wavenumbers than the lower G/D ratios.

The Raman results indicate that the intercalation efficiency depends on the G/D ratio or crystallinity of CVD-MLG. Therefore, a G/D ratio higher than 20 may be required for the $MoCl_5$ process. However, potential damage and sheet resistance reduction need to be investigated.

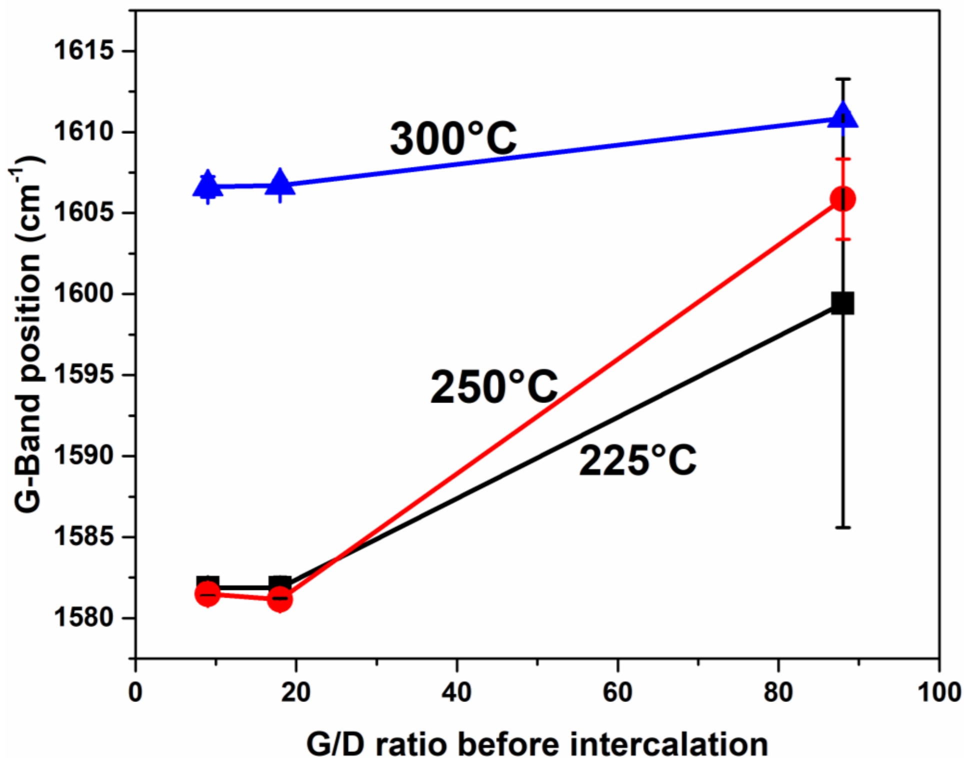

Figure 5.9. Relationship between the G-peak position of CVD-MLG after intercalation at different intercalation temperatures and the G/D ratio before intercalation.

Figure 5.10 shows the optical images of CVD-MLG before and after the intercalation process at different temperatures. In the case of lower CVD temperatures (800 ºC and 850 ºC), the morphology from optical images does not depend on the intercalation temperature. In the case of a high CVD temperature (900 ºC), the surface morphology depended on the intercalation temperature. The surface morphology after intercalation appears less uniform than that before the intercalation process. However, there is an increase in uniform area as the intercalation temperature increases. SEM analysis was required to study the surface morphology in more detail.

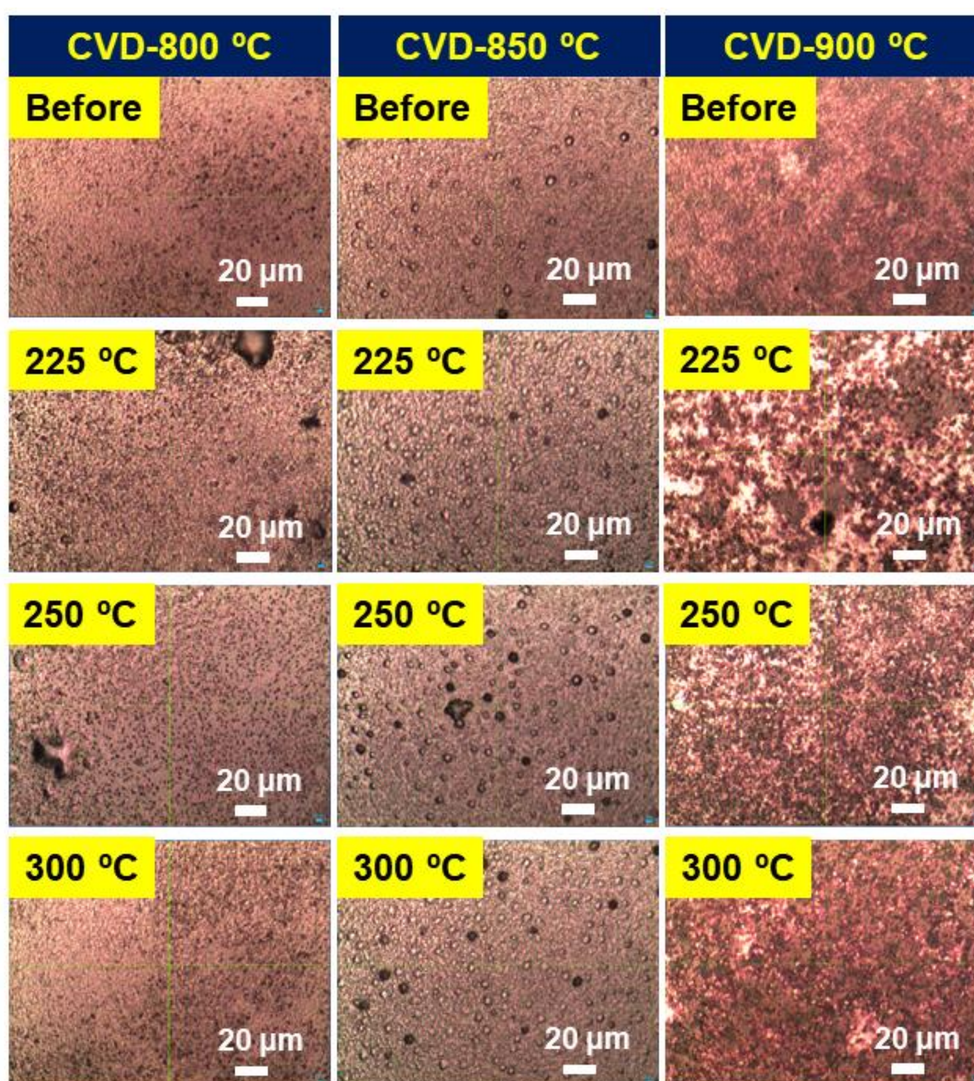

Figure 5.10. Optical images of CVD-MLG before and after the intercalation process.

Figure 5.11 shows the surface morphology of CVD-MLG films obtained by SEM before and after intercalation at different temperatures. In the case of CVD temperatures of 800 ºC and 850 ºC, the surface morphology appears hazy, similar to the optical image results. However, the hazy surface was reduced with a CVD temperature of 900 ºC because of the sample position being far from the chemical source. From the viewpoint of intercalation temperature dependence, a clear or non-hazy surface appeared for a high intercalation temperature of 300 ºC.

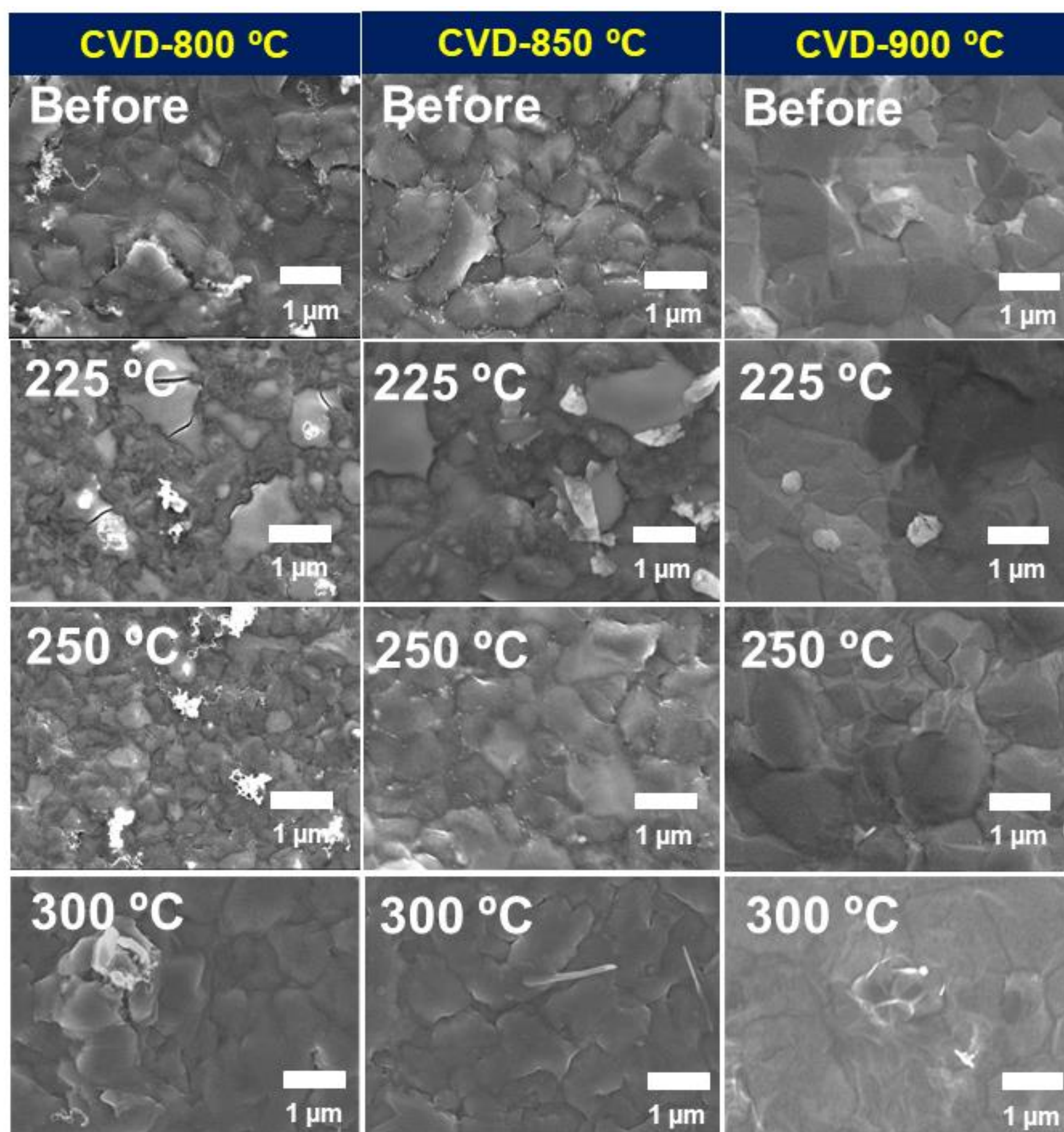

Figure 5.11. SEM surface morphology before and after intercalation at different temperatures.

Figure 5.12 shows cross-sectional SEM images of CVD-MLG before and after intercalation at 300 ℃. After intercalation, Ni was removed from the interlayer of Ni and MLG because of the simultaneous doping/etching process [13,14] at the CVD temperature of 800 ℃. For higher CVD temperatures, the Ni was not removed. The lower crystallinity and proximity to the chemical source may affect the reaction between Cl gas and Ni. It is considered that Cl gas may etch Ni through the MLG layer more easily in the poorer crystallinity MLG films of 800 ℃.

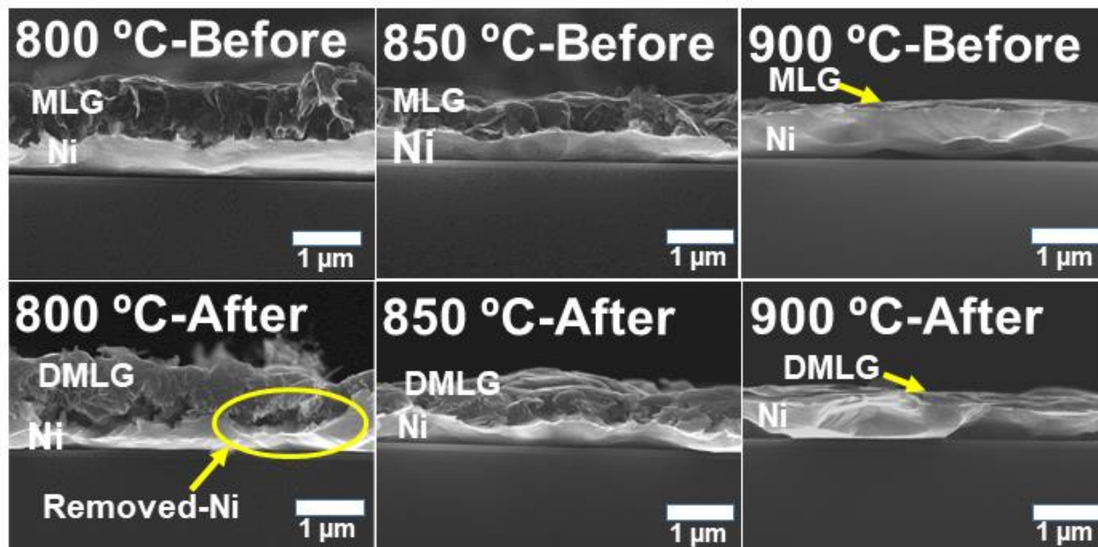

Figure 5.12. Cross-sectional SEM images of CVD-MLG before and after intercalation at 300 ℃.

Figure 5.13 shows cross-sectional EDX mapping before and after intercalation at 300 ℃ of CVD temperature at 800 ℃. On the top of the mapping area, C is present and corresponds to the MLG from the CVD process; C remains before and after intercalation at 300 ℃. After intercalation at 300 ℃, Mo, Cl, and O appear at this top area, with C, in the CVD-MLG layer. EDX mapping results confirm that $MoCl_5$ molecules were intercalated into the CVD-MLG layer after the intercalation process, which corresponds to the Raman spectra results.

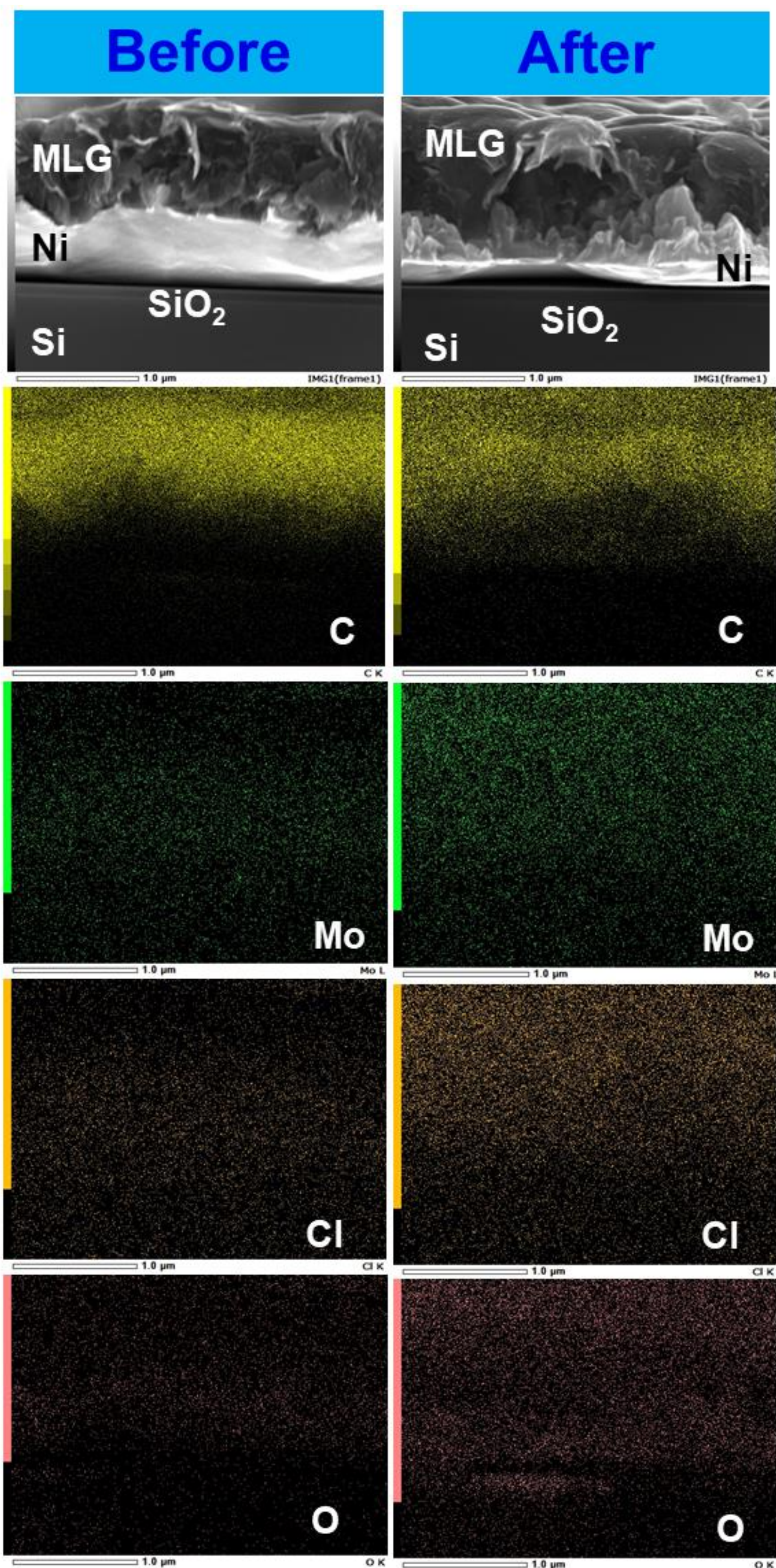

Figure 5.13. EDX mapping of cross-sectional SEM before and after intercalation at 300 ºC.

Figure 5.14 shows the sheet resistance reduction after intercalation at 300 ℃. The CVD temperature at 800 ℃ shows the highest reduction of sheet resistance because of the thicker MLG being intercalated by $MoCl_5$. The reduction of sheet resistance is still lower than that of the e-HOPG film (~80%) because of lower thickness (~10 μm) and lower crystallinity. However, a CVD temperature of 900 ℃ may be used for the pattering of CVD-MLG for inductor fabrication because of the lower sheet resistance before intercalation as shown in Fig. 5.7, although the reduction ratio after intercalation is less than that of 800 ℃.

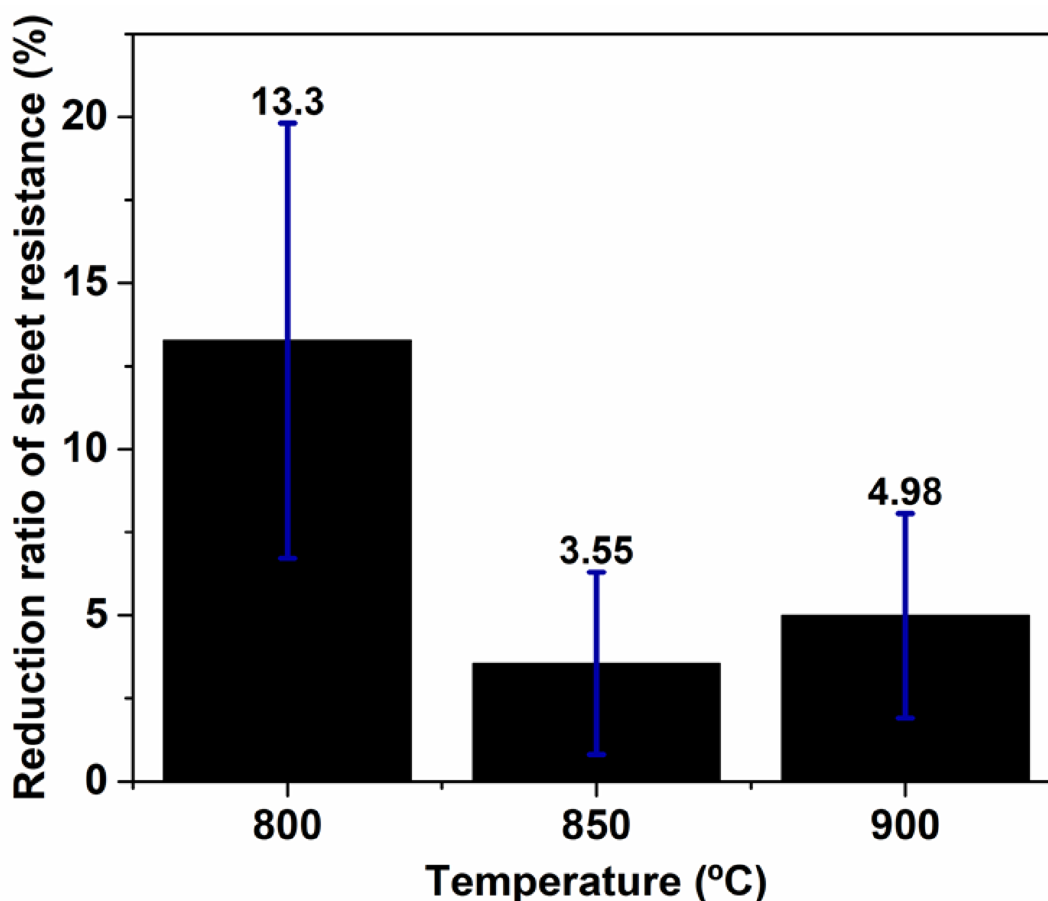

Figure 5.14. Sheet resistance reduction after intercalation at 300 ℃.

5.4 Summary and conclusion

In this chapter, the CVD temperature was optimized for the $MoCl_5$ intercalation process with CVD-MLG. High-crystallinity CVD-MLG with a G/D ratio of 88 was obtained with a high temperature of 900 ℃. A higher crystallinity or a G/D ratio of more than 20 was required for $MoCl_5$ intercalation. The morphology did not differ after the intercalation process, which suggests minimal damage. Cross-sectional SEM showed a stacked layer of CVD-MLG and Ni. Moreover, the Ni layer was partially removed after intercalation at 300 ℃, especially for the CVD film at lower CVD temperature. The sheet resistance reduction of CVD-MLG varied from 3.55% to 13.3% after intercalation at 300 ℃. Although the deposition temperature is high, a CVD temperature of 900 ℃ may be used for the pattering of CVD-MLG and for providing improved electrical and crystallographic properties.

References

[1] J. Kang, Y. Matsumoto, X. Li, J. Jiang, X. Xie, K. Kawamoto, M. Kenmoku, J.H. Chu, W. Liu and J. Mao: Nature Electronics. **1**, 46 (2018).

[2] K. Agashiwala, A. Pal, W. Cao, J. Jiang and K. Banerjee: 2018 IEEE International Electron Devices Meeting (IEDM), p. 24.4. 1 (2018).

[3] W. Xu, H. Wu, D.S. Gardner, S. Sinha, T. Dastagir, B. Bakkaloglu, Y. Cao and H. Yu: Journal of Applied Physics. **109**, 07A316 (2011).

[4] C.-J. Chao, S.-C. Wong, C.-H. Kao, M.-J. Chen, L.-Y. Leu and K.-Y. Chiu: IEEE transactions on semiconductor manufacturing. **15**, 19 (2002).

[5] E. Lancelot, "Perspectives on Raman Spectroscopy of Graphene." HORIBA, Jun. 2013

[6] L. G. Cançado, K. Takai, T. Enoki, M. Endo, Y. A. Kim, H. Mizusaki, A. Jorio, L. N. Coelho, R. Magalhães-Paniago, and M. A. Pimenta, Appl. Phys. Lett., **88**, 163106 (2006)

[7] T. Akimoto and K. Ueno, Proc. Electron Devices Technology and Manufacturing Conf., 2019, p. 351.

[8] M.S. Uddin and K. Ueno, Jpn. J. Appl. Phys. **56**, 04CP08 (2017).

[9] E. Ketsombun and K. Ueno, Proc. Int. Conf. Solid State Devices and Materials, 2020, pp127-128.

[10] H. Miyazaki, R. Matsumoto, M. Katagiri, T. Yoshida, K. Ueno, T. Sakai and A. Kajita: Japanese Journal of Applied Physics. **56**, 04CP02 (2017).

[11] R. Matsumoto and N. Akuzawa, Mater. Today Commun. **20**, 100532 (2019).

[12] M.S. Dresselhaus and G. Dresselhaus, Adv. Phys. **30**, 139-326 (1981).

[13] K. Yokosawa, T. Akimoto, Y. Okada and K. Ueno, Proc. Electron Devices Technology and Manufacturing Conf., 2019, p. 47.

[14] M. Kosaka, S. Takano, K. Hasegawa and S. Noda, Carbon. **82**, 254 (2015).

CHAPTER 6
INTERCALATION OF PATTERNED CVD-MLG

6.1 Introduction

In Chapter 5, a thermal CVD process expected to deposit high-crystallinity material was developed for MLG patterning at the wafer scale. $MoCl_5$ was intercalated in CVD-MLG and the reduction of sheet resistance after the intercalation process was observed.

In this chapter, high-crystallinity MLG patterns at the wafer scale are developed using a thermal CVD process. High-crystallinity MLG patterns were deposited selectively on Ni patterns using the optimized CVD conditions obtained in Chapter 5. Moreover, $MoCl_5$ intercalation doping is adopted to reduce the resistance using optimized intercalation conditions. We observed pattern width dependencies of crystallinity and doping efficiency in the patterned doped MLG. Issues needing further improvements in patterned and doped CVD-MLG are also discussed in this chapter.

6.2 Experimental methods

Figure 6.1 shows the fabrication procedure used to obtain doped MLG patterns. Ni patterns with a thickness of 800 nm were formed on a SiO_2/Si substrate by sputtering with a shadow mask. The pattern width was 1–2.5 mm, which is much wider than the target size for inductors, but was chosen because of the experimental limitations of shadow mask patterning. MLG films were then deposited on the patterned Ni by CVD using an ethanol precursor with Ar bubbling gas. The CVD temperature was controlled at 900 ℃, with an Ar flow rate of 70 sccm for 5 min. For the TLM measurement, the CVD-time at 7 min was used for CVD-MLG fabrication. For intercalation, the CVD-MLG on Ni catalyst was inserted into a glass capsule with 0.0374 g of $MoCl_5$ and 0.0073 g of MoO_3. The chemical concentrations were optimized in previous studies of e-HOPG [1]. After enclosing the glass capsule, the capsule was inserted into a glass tube and pre-annealed at 110 ℃ in an Ar atmosphere for degassing before intercalation. The intercalation temperature was varied between 225 ℃ and 300 ℃ for 30 min. The crystallinity of CVD-MLG and the doping states were analyzed by Raman spectroscopy.

The cross-section and surface morphology were observed by SEM. The sheet resistance was characterized by the four-terminal method.

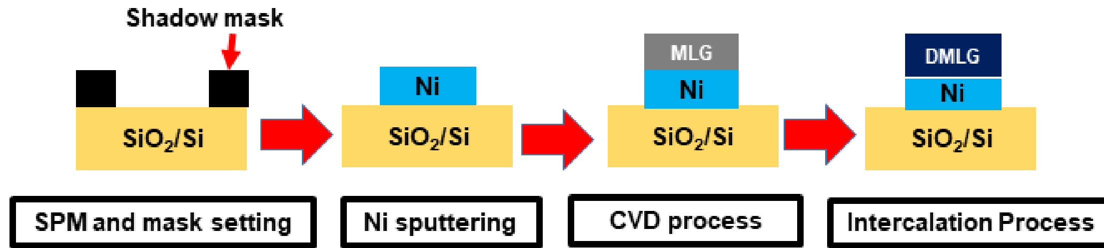

Figure 6.1. Fabrication procedure of doped MLG patterns.

6.3 Results and discussion

6.3.1 Fabrication of CVD-MLG patterns

Based on the optimized CVD process and intercalation conditions for CVD-MLG/Ni provided in Chapter 5, the patterned structures of CVD-MLG/Ni were fabricated as shown in Figure 6.2. Pd electrodes with a thickness of 50 nm were evaporated to measure sheet resistance. The sheet resistance can be calculated using the following equation [2]:

$$R_s = \frac{V}{I}\frac{W}{L} \quad (6.1)$$

where R_s is the sheet resistance, I is the applied current, V is the feedback voltage, W is the width of the patterned MLG, and L is the length of the patterned MLG.

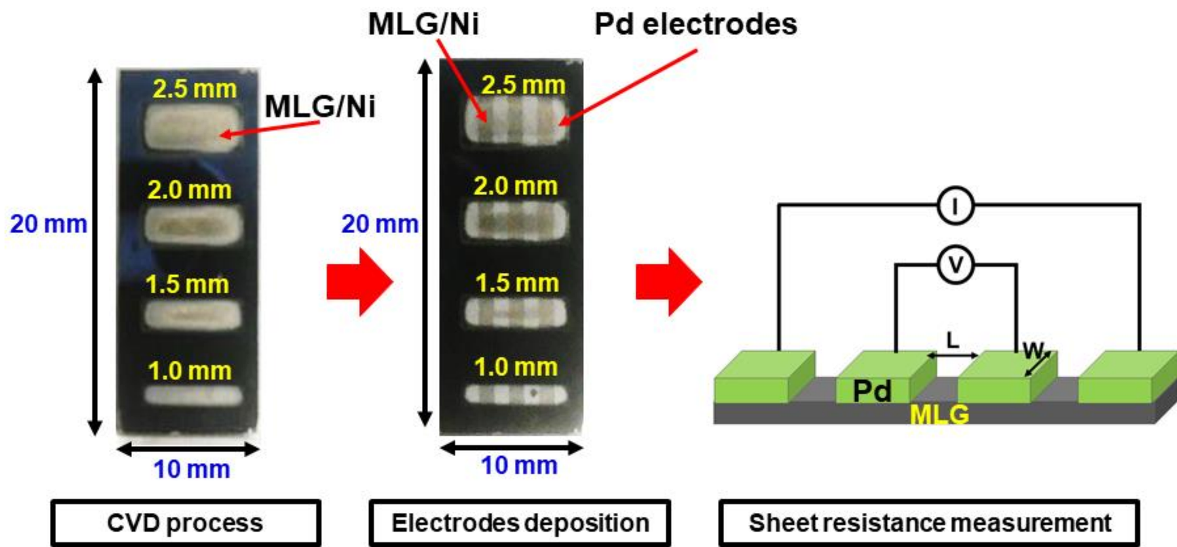

Figure 6.2. Fabricated MLG/Ni patterns (left) and a schematic of the four-terminal Pd electrodes (right) to measure sheet resistance.

Figure 6.3 shows the Raman spectra of CVD-MLG on Ni catalyst for each width. The spectra consist of D-, G-, and 2D-bands for all widths [3]. The spectra confirmed the uniformity of the CVD process for the patterning of each width.

Figure 6.4 shows the G/D ratio of patterned CVD-MLG on Ni for different widths. The G/D ratio corresponds to the crystallinity of CVD-MLG [4–6]. The G/D ratio exceeded 20 for all widths and, therefore, is suitable for effective intercalation. The G/D ratio increased as the width increased. A large uniform area of Ni catalyst may enhance MLG growth with higher crystallinity. It was speculated that the reduction of Ni thickness at the pattern edge by shadowing with the mask may have resulted in the reduction of the G/D ratio, as shown by the width dependence of the thickness.

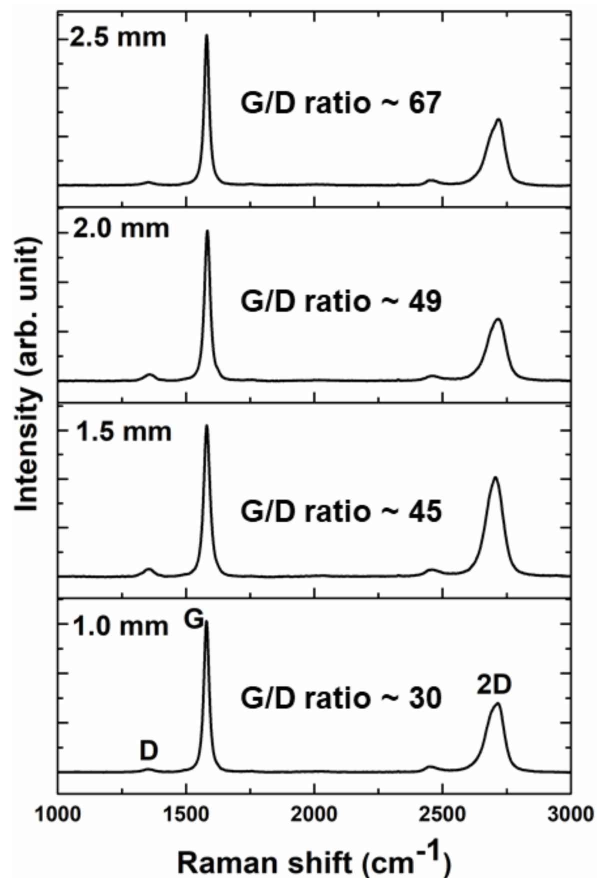

Figure 6.3. Raman spectra of CVD-MLG on Ni catalyst for each width.

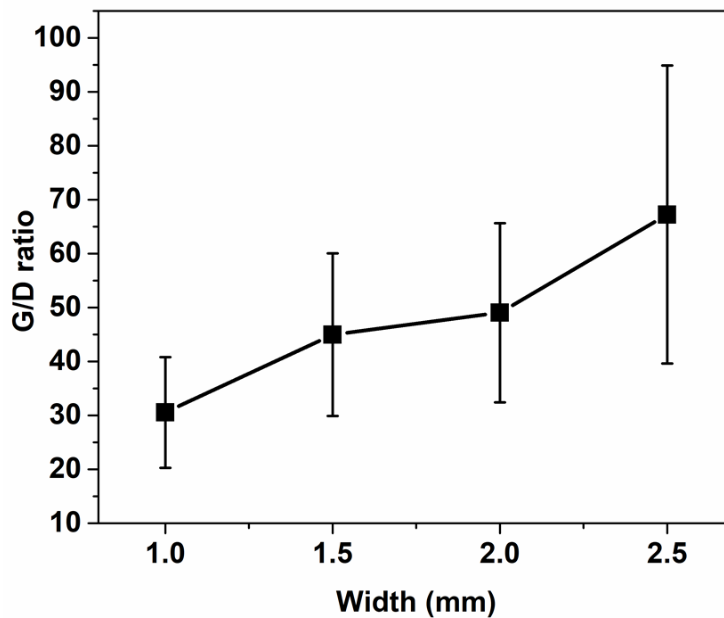

Figure 6.4. G/D ratio of CVD-MLG on Ni patterns of different widths.

Figure 6.5 shows that the thickness of patterned CVD-MLG/Ni increased as the width increased. It was also noted that the thickness was different between the center and edge of the patterned CVD-MLG because of the shadow effect during Ni deposition [7]. It is expected that the shadow effect will not be a problem if photolithography is used for future patterning.

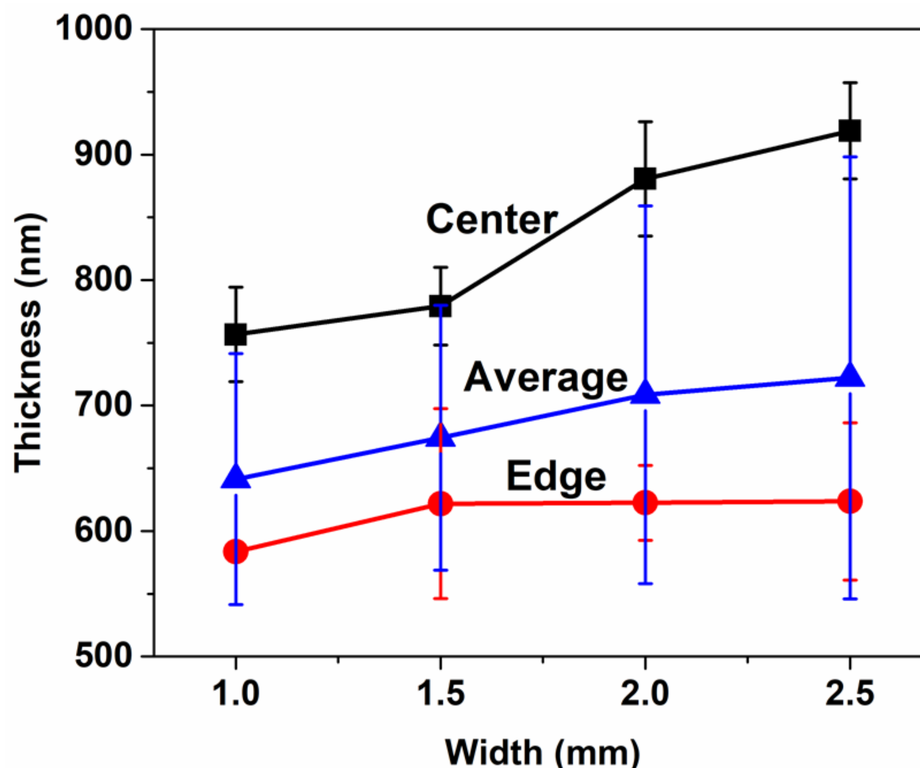

Figure 6.5. Thickness of MLG/Ni at the center and edge of the pattern for each width.

6.3.2 Doping efficiency of CVD-MLG patterns

Figure 6.6 shows the doping efficiency of different widths. The G-band at the center of the pattern was shifted to a higher wavenumber than that at the edge of the pattern because of the variation of the G/D ratio on the patterned CVD-MLG. However, all widths can be intercalated in the uniform area, between the center and edge, with high doping of stage 2 and above [1, 8-9].

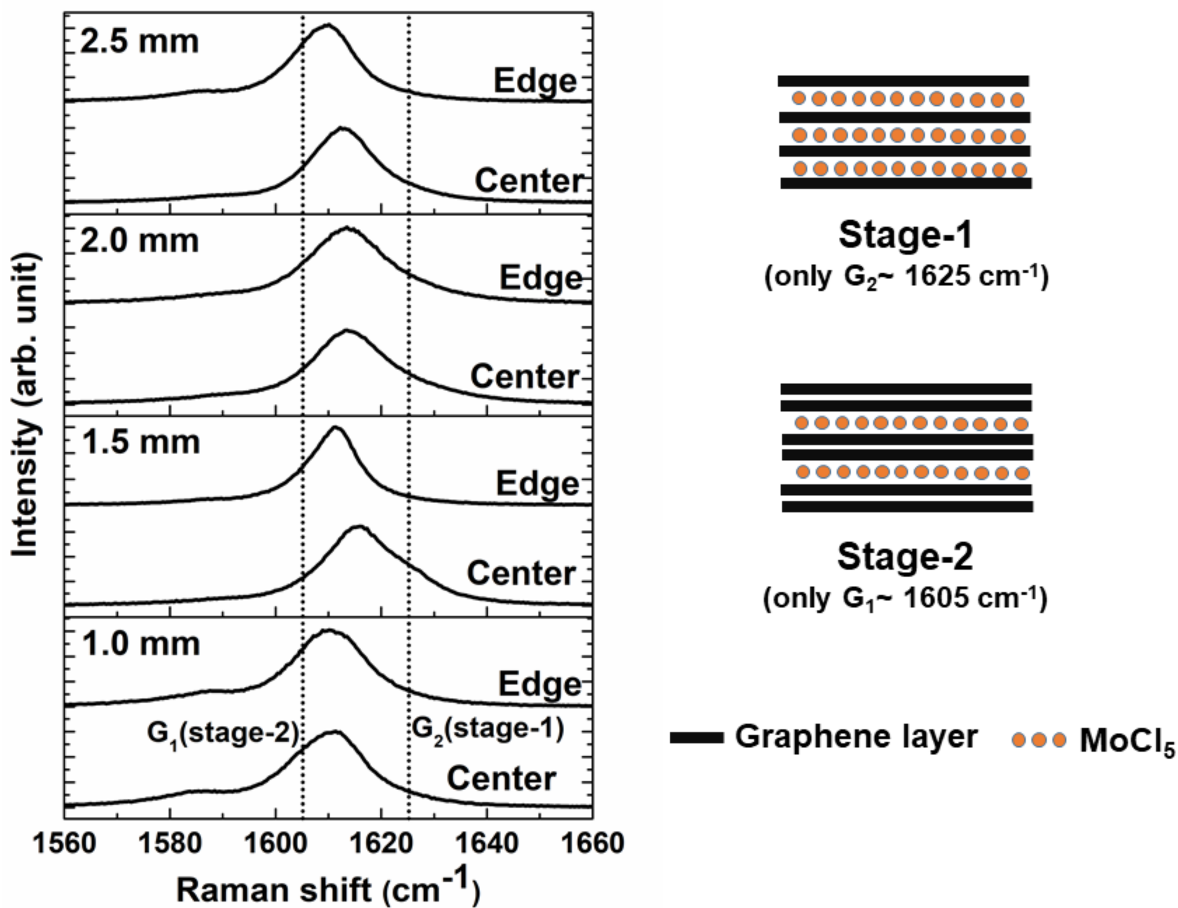

Figure 6.6. G-band spectra at the center and edge of the pattern for each width.

Figure 6.7 shows optical images of the surface of patterned CVD-MLG on Ni catalyst for each width before and after intercalation. The surface morphology does not show much difference before and after intercalation. Damage on the surface of the CVD-MLG may not be observable by optical microscopy. Higher-magnification observations are required to confirm surface damage after the intercalation process.

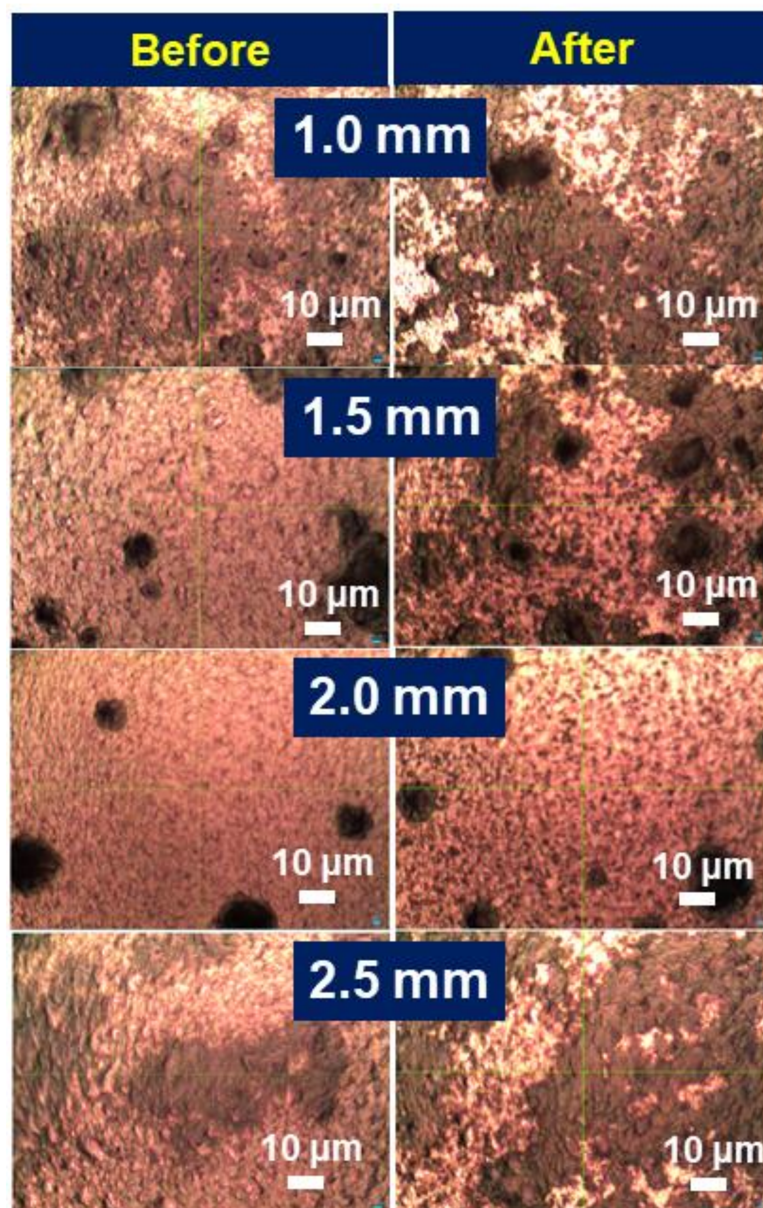

Figure 6.7. Optical images of the surface of patterned CVD-MLG on Ni catalyst for each width.

Figure 6.8 shows SEM images of the surface morphology before and after the intercalation process at the center and edge of the patterns. From the morphology at the center of the patterns, a hole 1–2 μm in size was found in the width of the pattern and more area was observed for the 1.0-mm width than for the higher widths. However, the surface

morphology at the center of the patterns was not different after the intercalation process. For the edge of the patterns, more hole morphology was found than at the center of the patterns. The lower thickness at the edge of the pattern, as shown in Figure 6.6, may have induced the holes at the edge of the sample. However, the surface morphology at the edge of the patterns was not different after the intercalation process. Damage was not observed on the patterned CVD-MLG after the intercalation process. The low thickness of MLG on the patterned CVD-MLG may make it difficult to distinguish a damaged area with such a rough surface.

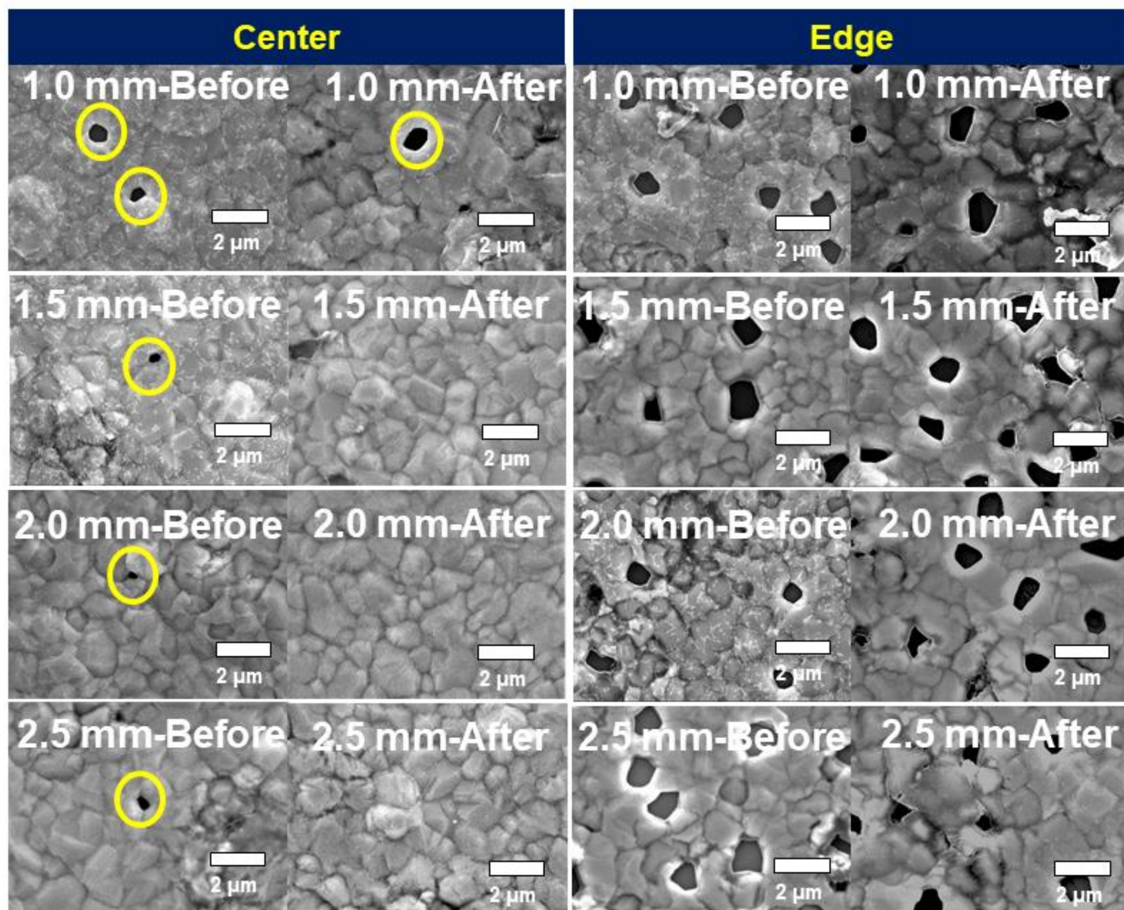

Figure 6.8. SEM surface morphology of patterned CVD-MLG on Ni catalyst for each width.

Figure 6.9 shows the sheet resistance dependence on the width before and after intercalation. The sheet resistance increases in the narrower width because the Ni thickness became thinner for narrower patterns because of shadowing effects. After intercalation, the sheet resistance decreased for the 2.5-mm width but increased for the 1-mm width. The sheet

resistance of MLG/Ni is considered the combined resistance of MLG and Ni layers. As the Ni layer was potentially simultaneously etched by the chlorine (Cl) gas generated from $MoCl_5$ during the intercalation process [10, 11], it is considered that some portion of Ni was etched during intercalation at the pattern edge. The edge effect is considered to be larger in the 1-mm width than in the 2.5-mm width. As shown in Figure 6.10, the thickness of MLG/Ni is almost the same at the center of the 2.5-mm width before and after intercalation. Considering the potential increase of Ni sheet resistance by etching, the sheet resistance reduction of the 2.5-mm pattern is considered to be due to the reduction of MLG sheet resistance with intercalation. By further optimizing the intercalation process, doped MLG patterns without the Ni layer are expected to be obtained by the simultaneous etching of Ni.

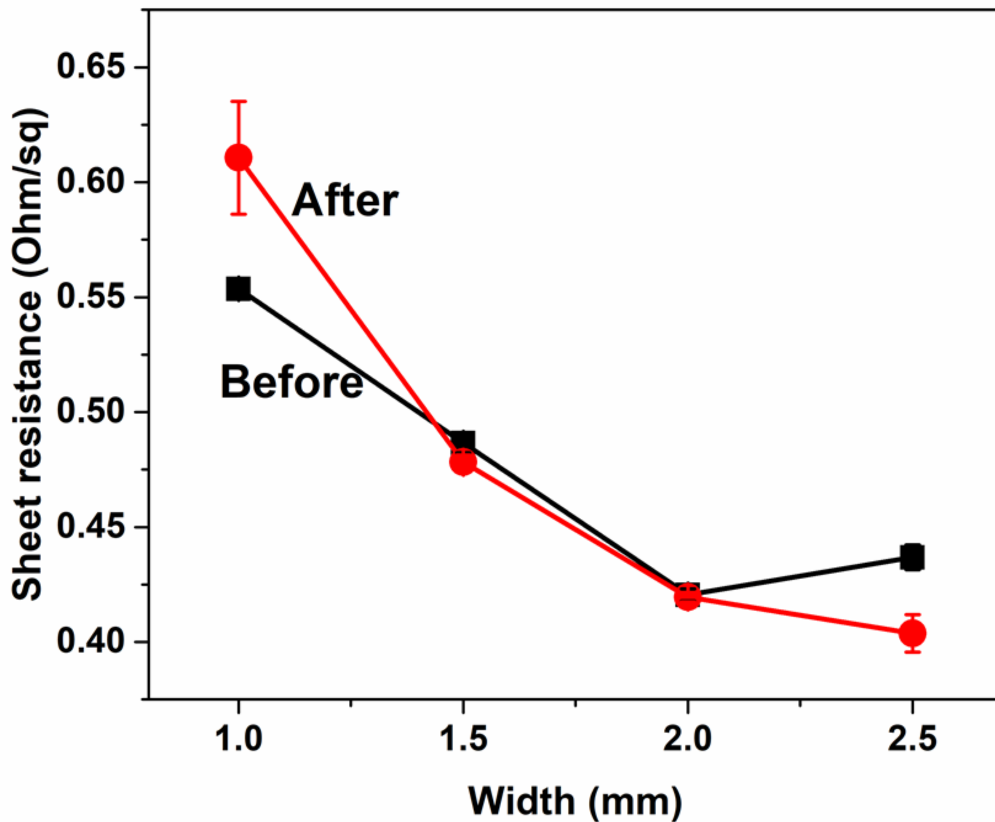

Figure 6.9. Sheet resistance before and after intercalation for different widths.

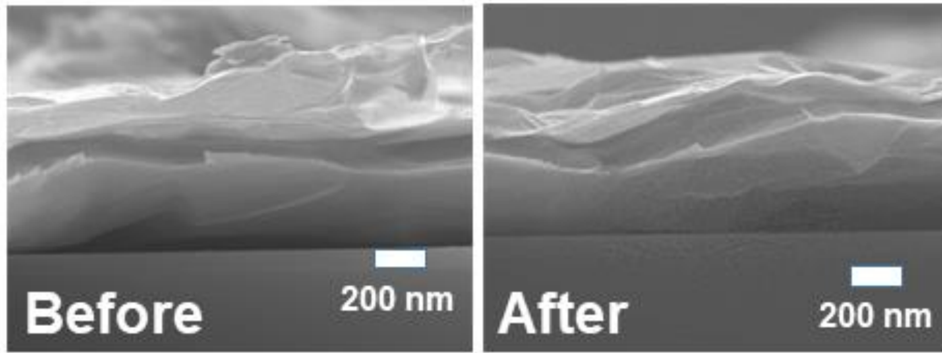

Figure 6.10. Cross-sectional SEM images of 2.5-mm width patterns before and after intercalation at 300 ℃ for 30 min.

6.3.3 TLM measurement of CVD-MLG patterns

To confirm the effect of doping efficiency to the reduction of sheet resistance after the $MoCl_5$ intercalation process, the patterned structures of CVD-MLG/Ni were fabricated for the TLM measurement as shown in Figure 6.11. Pd electrodes with a thickness of 50 nm were evaporated to measure sheet resistance. The contact resistance and sheet resistance can be extracted by fitting the plot of the relationship between length and total resistance (R_T), as given by the equation [12]

$$R_T = R_S \frac{L}{W} + 2R_C, \tag{6.2}$$

where R_s is the sheet resistance, R_C is the contact resistance, W is the width of the patterned MLG, and L is the length between the two metal electrodes.

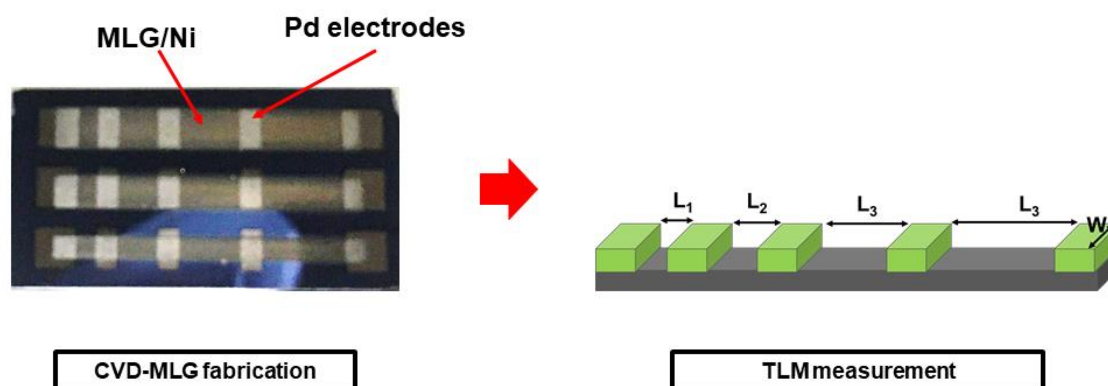

Figure 6.11. Fabricated MLG/Ni patterns for the TLM measurement (left) and a schematic of the TLM measurement (right) to measure sheet resistance and contact resistance.

Figure 6.12 shows optical images of the surface of patterned CVD-MLG on Ni catalyst for the TLM measurement before and after intercalation. The surface morphology does not show much difference before and after intercalation same as Fig. 6.7.

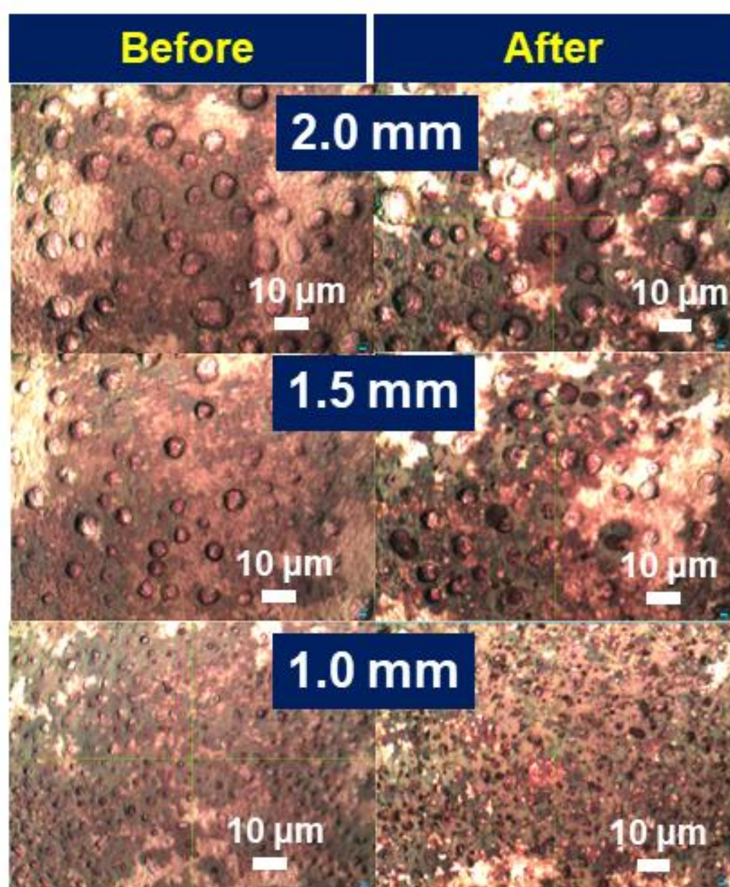

Figure 6.12. Optical images of the surface of patterned CVD-MLG on Ni catalyst for TLM-measurement structure.

Figure 6.13 shows the doping efficiency of of CVD-MLG for the TLM-measurement structure. The G-band shows the G_0 and G_1 peaks, the I_{G0}/I_{G1} ratio is between 0.5 to 1.0 as can be confirmed the mixed stage 3 and 4 intercalation after the intercalation process with all widths.

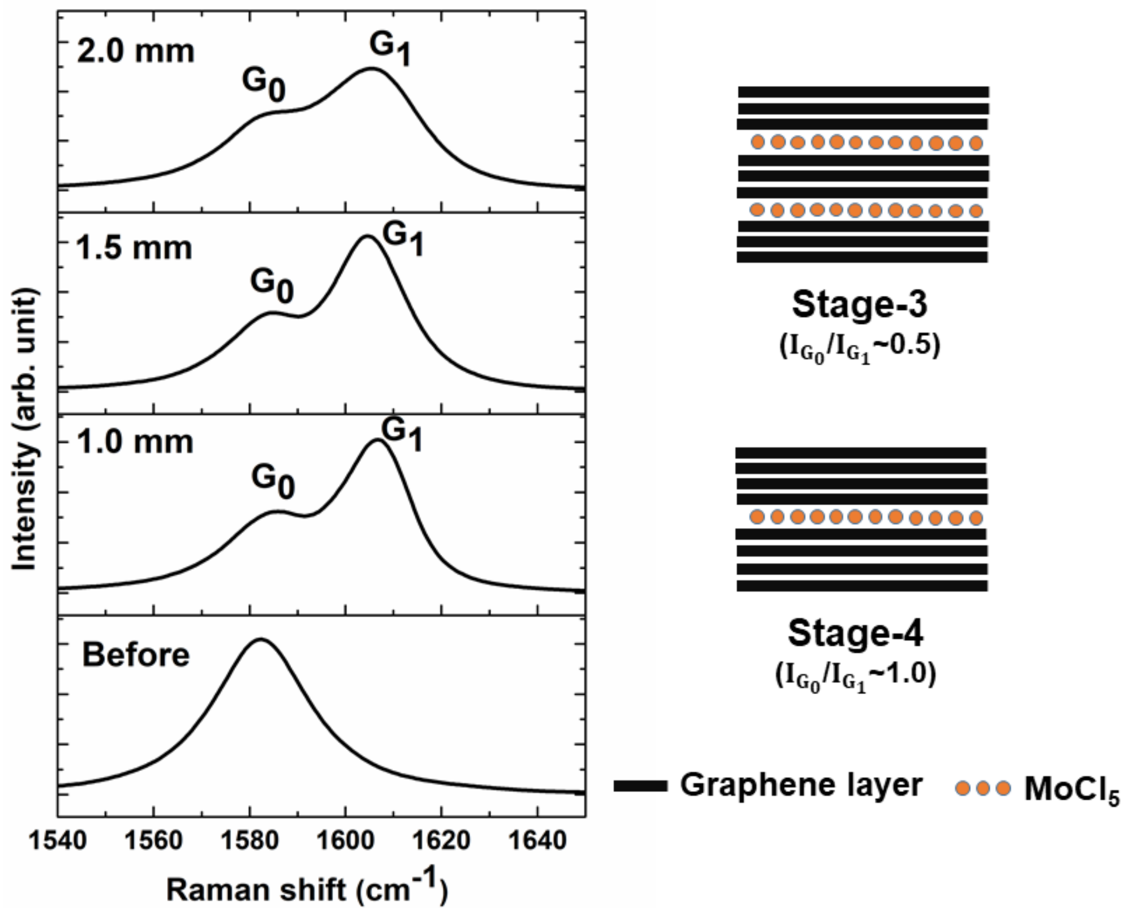

Figure 6.13. G-band spectra of CVD-MLG for the TLM-measurement structure.

Figure 6.14 shows the sheet resistance dependence on the width before and after intercalation from the TLM-measurement. The sheet resistance tends to decrease as increasing the width. The sheet resistance after intercalation of 1.0 mm and 1.5 mm width was lower than before the intercalation process. The sheet resistance of MLG/Ni is considered the combined resistance of MLG and Ni layers. The sheet resistance of 2.0 mm width did not show much difference before and after intercalation, probably the contribution of Ni sheet resistance was relatively higher than those in 1.0 and 1.5 mm width in which the Ni layer thickness was thinner due to the shadow effects. Moreover, the lower doping efficiency in 2.0 mm width as shown in Fig.6.13 may have led to less reduction of sheet resistance. Since the difference of CVD-time and the electrical characterization method, the sheet resistance result seems to show a different trend from Fig. 6.9. MLG thickness uniformity in the narrower width (1.0

mm) may be improved by longer CVD-time. From this result, it is considered that the sheet resistance of MLG was reduced by doping and it is expected that to be used in the narrower width such as micrometer width in the future.

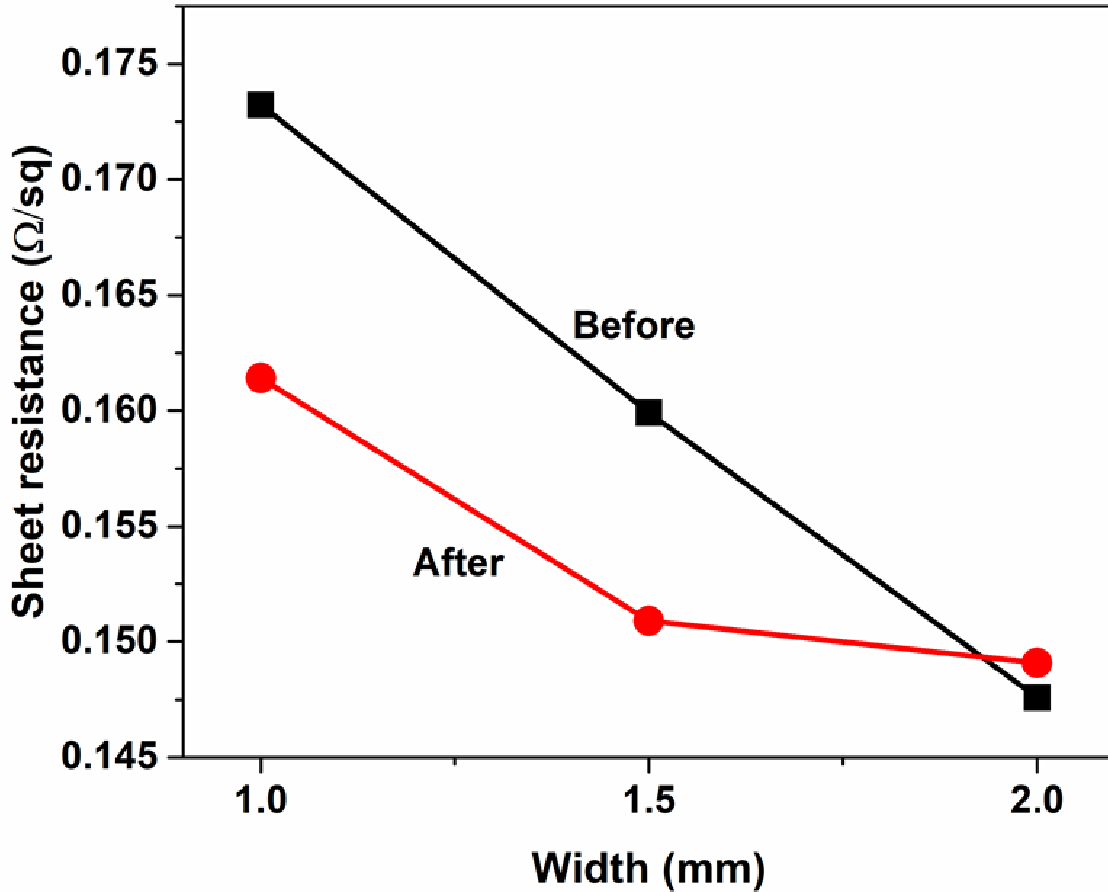

Figure 6.14. Sheet resistance before and after intercalation from the TLM-measurement.

Figure 6.15 shows the contact resistance dependence on the width before and after intercalation from the TLM-measurement. The contact resistance tends to decrease as increasing the width. The contact resistance was also reduced by the effect of intercalation doping. Moreover, the contact resistance of 1.0 mm width seems to reduce more than other widths, it seems that the doping efficiency affects to the contact resistance.

However, further electrical characterization of doped CVD-MLG such as Hall measurement is required to reveal the effect of intercalation doping to the CVD-MLG.

Unfortunately, we have a limit of characterization in terms of Hall measurement in our laboratory. So, it will be a topic of future study.

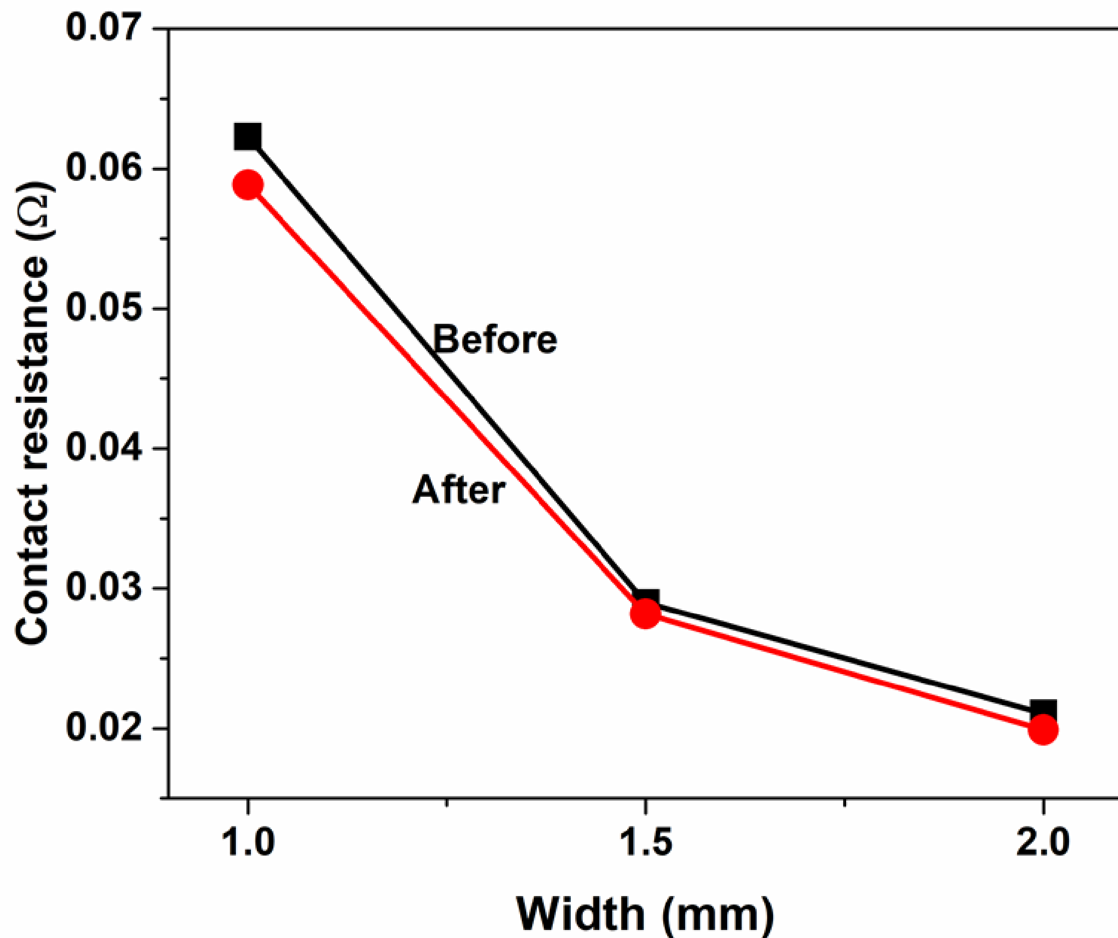

Figure 6.15. Contact resistance before and after intercalation from the TLM-measurement.

In this experiment, the shadow mask was used for the patterning of Ni catalyst before the fabrication of MLG by the CVD process. The shadow effect from the shadow mask leads to the non-uniform thickness of Ni catalyst and also affects the uniformity of MLG thickness. The performance of inductors is expected to be improved by improving the MLG-thickness uniformity. For some inductor applications, thicker MLG will be required. However, the thickness of CVD-MLG was ~200 nm which is thinner than that of reported e-HOPG inductors (more than 700 nm) [13]. The crystallinity improvement of thick CVD-MLG may

be an additional issue that must be solved, since the crystallinity of CVD-MLG was degraded as increasing the thickness. Therefore, further process development is required to improve the uniformity and the crystallinity of CVD-MLG depending on the required thickness.

6.4 Summary and conclusion

In this chapter, a more practical fabrication process for doped MLG patterns, using selective CVD and $MoCl_5$ intercalation, was developed. A higher doping density was obtained by improving the MLG crystallinity with a G/D ratio above 20. Stage 2 and above intercalation was achieved by the optimized intercalation discussed in Chapter 5 using high-crystallinity CVD-MLG. Intercalation damage was not observed clearly, although further improvement of surface morphology is required. The sheet resistance was reduced after intercalation in a wide pattern. However, sheet resistance increased after intercalation in a narrow pattern. The pattern dependence is considered to be due to the width dependence of the Ni thickness from the shadow effects of patterning and the width dependence of Ni width reduction during $MoCl_5$ intercalation. The resistance measured in this chapter is the combined resistance of the doped MLG and the residual Ni catalyst. To obtain the resistance of doped MLG only, it is necessary to remove the Ni layer. In the narrower patterns, such as those of the order of micrometers, Ni catalyst is expected to be removed by etching from the pattern edge with Cl_2 gas during $MoCl_5$ intercalation. In the future, we will fabricate narrower Ni patterns using photolithography, which is expected to eliminate the mask shadow effects observed in this chapter and lead to more uniform thickness of Ni patterns as well as improved MLG crystalline uniformity and doping efficiency.

References

[1] E. Ketsombun and K. Ueno, Proc. Int. Conf. Solid State Devices and Materials, 2020, pp127-128.

[2] X. Wu, Y. Chuang, A. Contino, B. Sorée, S. Brems, Z. Tokei, M. Heyns, C. Huyghebaert and I. Asselberghs, Adv. Mater. Interfaces. **5**, 1800454 (2018).

[3] E. Lancelot, “Perspectives on Raman Spectroscopy of Graphene.” HORIBA, Jun. 2013

[4] L. G. Cançado, K. Takai, T. Enoki, M. Endo, Y. A. Kim, H. Mizusaki, A. Jorio, L. N. Coelho, R. Magalhães-Paniago, and M. A. Pimenta, Appl. Phys. Lett., **88**, 163106 (2006)

[5] T. Akimoto and K. Ueno, Proc. Electron Devices Technology and Manufacturing Conf., 2019, p. 351.

[6] M.S. Uddin and K. Ueno, Jpn. J. Appl. Phys. **56**, 04CP08 (2017).

[7] H. Okuyama, N. Iwata and H. Yamamoto: MRS Online Proceedings Library Archive. 901 (2005).

[8] R. Matsumoto and N. Akuzawa, Mater. Today Commun. **20**, 100532 (2019).

[9] H. Miyazaki, R. Matsumoto, M. Katagiri, T. Yoshida, K. Ueno, T. Sakai and A. Kajita: Japanese Journal of Applied Physics. **56**, 04CP02 (2017).

[10] K. Yokosawa, T. Akimoto, Y. Okada and K. Ueno, Proc. Electron Devices Technology and Manufacturing Conf., 2019, p. 47.

[11] M. Kosaka, S. Takano, K. Hasegawa and S. Noda, Carbon. **82**, 254 (2015).

[12] X. Wu, Y. Chuang, A. Contino, B. Sorée, S. Brems, Z. Tokei, M. Heyns, C. Huyghebaert and I. Asselberghs, Adv. Mater. Interfaces. **5**, 1800454 (2018).

[13] J. Kang, Y. Matsumoto, X. Li, J. Jiang, X. Xie, K. Kawamoto, M. Kenmoku, J.H. Chu, W. Liu and J. Mao: Nature Electronics. **1**, 46 (2018).

CHAPTER 7
CONCLUSIONS AND FUTURE PROSPECTS

7.1 Overall conclusions

MLG is expected to behave as a conductor material with low resistance and high reliability for electron devices, such as interconnects, electrodes, and high-frequency inductors. Carrier doping is required to obtain low-resistance MLG as pristine MLG has fewer carriers. $MoCl_5$ intercalation is a known stable doping method. In this work, the optimization of the $MoCl_5$ intercalation process for many MLG thicknesses was studied for conductor applications, which require different thicknesses. $MoCl_5$ intercalation doping was achieved for FLG obtained by the CVD process and films exfoliated from e-HOPG for thick, high-crystallinity MLG. CVD-MLG on Ni catalyst was optimized for increased doping efficiency and reduced damage of the graphene layer as they correspond to the reduction of sheet resistance after the intercalation doping process.

As a practical fabrication process for their application as inductors, doped MLG patterns using the CVD process and $MoCl_5$ intercalation were demonstrated. Stage 2 or higher of intercalation doping was achieved, which is expected to yield low-resistance MLG.

7.2 Conclusions for each chapter

7.2.1. Chapter 3

Doped FLG is expected to be used in applications that include LSI interconnects and transparent electrodes of solar cells. Temperature, time, and chemical concentration dependencies of $MoCl_5$ intercalation of FLG were investigated to optimize process conditions from the viewpoints of doping efficiency and process damage. For high chemical concentrations, the intercalation temperature can be reduced to 150 ºC to reduce FLG damage. A resistivity of 14 μΩ cm is reached for a micron-size graphene device. For reduced chemical concentrations, the doping uniformity was improved by increasing the reaction time. It was found that the intercalation efficiency and the damage of FLGs depend on the number of graphene layers. The optimum temperature and time increase as the layer number increases.

Either a higher temperature or a longer reaction time leads to increased doping efficiency and damage. By comparing the G-peak shift and the G/D ratio, better conditions for FLG intercalation were found to be 200 ºC for 60 min rather than 175 ºC for 120 min. It is suggested that the optimization of intercalation temperature and time is important, depending on the layer number, for device applications of FLG.

7.2.2. Chapter 4

Thick MLG, of the order of micrometers, is required for MLG applications in high-frequency devices, such as inductors. Moreover, the high inductance density of doped MLG is expected in inductor applications because of the kinetic inductance of doped MLG. This chapter optimized the $MoCl_5$ intercalation process for relatively thick e-HOPG films in terms of resistance and damage. We achieved a 77% decrease in sheet resistance with reduced damage by reducing the amount of chemical to one-fifth of that of FLG at 225 °C for 15 min. The strain and hole density induced during the intercalation process were analyzed using G and 2D peak correlation plots. The changes in strain and carrier density agreed well with the observed damage and sheet resistance. Strain is considered to be induced during the intercalation process, resulting in line-shaped defects. As the induced strain depends on the MLG thickness, a further decrease in damage is expected for thinner films. The sheet resistance reduction effect of $MoCl_5$ intercalation is comparable to that of Br intercalation used to demonstrate doped MLG inductors with high inductance density. Therefore, $MoCl_5$ intercalation is promising for thick MLG applications, such as on-chip inductors, because of its environmental stability and doping efficiency. Optimizing the intercalation conditions in terms of thickness is essential for $MoCl_5$ intercalation to resolve the trade-off between doping concentration and damage due to intercalation.

7.2.3. Chapter 5

CVD-MLG is expected to be a more practical method for device manufacture than e-HOPG. In this chapter, the optimization of CVD temperature provides a guideline for the $MoCl_5$ intercalation process with patterned CVD-MLG. High-crystallinity CVD-MLG with a G/D ratio of 88 was obtained with a high CVD temperature of 900 ºC. A higher crystallinity

or a G/D ratio more than 20 was required for $MoCl_5$ intercalation. The morphology did not differ after the intercalation process, which suggests minimal to no damage. Cross-sectional SEM images showed the stacked layers of CVD-MLG and Ni. Part of the Ni layer was removed after intercalation at a temperature of 300 ºC.

7.2.4. Chapter 6

Based on the optimized CVD and intercalation conditions provided in Chapter 5, doped MLG patterns were fabricated by selective CVD. A higher doping density was obtained with high-crystallinity patterned MLG on the Ni catalyst with a G/D ratio above 20. Stage 2 intercalation and above was achieved by increasing the intercalation temperature and using high-crystallinity CVD-MLG. The sheet resistance was reduced after intercalation. However, there was a pattern width dependence of the sheet resistance. The reason for the pattern dependence is considered to be the thickness variation induced by the shadow effect during Ni deposition. Moreover, the effect of Ni catalyst removal is considered the reason for sheet resistance reduction because the measured resistance is the parallel resistance of the doped MLG layer and the residual Ni catalyst layer. The reduction of the resistance in a wide pattern of the doped MLG/Ni indicates resistance reduction of the MLG layer after doping, despite the resistance increase with the partial removal of the Ni layer.

7.3. Future prospects

To avoid the shadow effect during Ni thin-film deposition, the use of photolithography is expected improve future patterning. Moreover, the narrow width of the patterned CVD-MLG may increase the etching of the Ni catalyst. By further optimization, a doped MLG pattern is expected to form without a Ni layer using the simultaneous etching of Ni.

Although the target value of the resistivity of doped-graphene depends on the applications of doped-graphene, it should be lower than the resistivity of metal interconnect such as copper after scaling down to the same width. According to the $FeCl_3$ intercalation-doped ML-GNR (multi-layer graphene nanoribbon) interconnects with a width down to ~20 nm, the resistivity as low as 21μΩ cm was obtained, and it is comparable to Cu of the same

size. For the target value of the doped-graphene for the inductor applications, the inductance value is considered to be the target value rather than resistivity. So, the target value of doped-graphene for inductor applications is the inductance higher than that of Br-intercalated MLG inductor at the same size, which was reported as 1.5 times higher than that of Cu.

In this study, we investigated the optimization of $MoCl_5$ intercalation, which is known as stable intercalation, to MLGs of various film thickness. Since there is a trade-off between the damage caused by intercalation and doping density, optimization according to the film thickness is indispensable. However, the optimized condition will lead to obtain a low-resistance and stable MLG for various conductor applications in electron devices such as interconnects, electrodes, and high frequency devices, along with practical MLG deposition methods such as CVD. Especially, doped MLGs are expected to be used for smaller and higher in performance of communication devices after 5G due to the characteristic feature of high inductance density.